NOTICE

AVIS

The quality of this microform is heavily dependent upon the quality of the original thesis submitted for microfilming. Every effort has been made to ensure the highest quality of reproduction possible.

La qualité de cette microforme dépend grandement de la qualité de la thèse soumise au microfilmage. Nous avons tout fait pour assurer une qualité supérieure de reproduction.

If pages are missing, contact the university which granted the degree.

S'il manque des pages, veuillez communiquer avec l'université qui a conféré le grade.

Some pages may have indistinct print especially if the original pages were typed with a poor typewriter ribbon or if the university sent us an inferior photocopy.

La qualité d'impression de certaines pages peut laisser à désirer, surtout si les pages originales ont été dactylographiées à l'aide d'un ruban usé ou si l'université nous a fait parvenir une photocopie de qualité inférieure.

Reproduction in full or in part of this microform is governed by the Canadian Copyright Act, R.S.C. 1970, c. C-30, and subsequent amendments.

La reproduction, même partielle, de cette microforme est soumise à la Loi canadienne sur le droit d'auteur, SRC 1970, c. C-30, et ses amendements subséquents.

Canada

Numerical Simulation of Imploding Shock Waves

Alidad Amirfazli

A Thesis

in

The Department

of

Mechanical Engineering

Presented in Partial Fulfilment of the Requirements
for the Degree of
Master of Applied Science
at
Concordia University
Montreal, Quebec, Canada

August 1994

ISBN 0-315-97581-4

Canada

ABSTRACT

Numerical Simulation of Imploding Shock Waves

Alidad Amirfazli

A numerical study was made of imploding shock waves. The objective of the present paper is to clarify the propagation and instability of the converging cylindrical and elliptical shock waves. In order to make the simulation, a second order explicit MacCormack type finite difference method was employed to solve the unsteady compressible Euler equations. At first, a one-dimensional simulation was preformed for converging cylindrical shock waves. The results were found to be in good agreement with the Chester, Chisnell and whitham relation. Also, the numerical results were in good agreement with other published 1-D numerical simulations (e.g. method of characteristic).

A two-dimensional simulation was also developed for initially perturbed implosions. The governing fluid dynamics equations have been solved in polar coordinates. The 2-D scheme is an extension to the 1-D case, using the operator splitting, where the multi-dimensional solution is evolved from a factored sequence of one dimensional operators. From the two-dimensional study of converging cylindrical shocks, it has been concluded that although the shock has been perturbed

initially in the azimuthal direction, it has a tendency to keep its continuous shock front curvature until it gets close to the centre. Eventually, at the centre a break down in the shock front is inevitable. Finally, for the elliptical shock the perturbation parameter (ξ) was found to vary with shock travel in a complex manner that can not be represented by a simple power law. This finding is in good agreement with recent experimental results.

Acknowledgements

.

Table of contents

List of Figures

Figure:

Nomenclature

Latin symbols

A	Control surface
A	Jacobian matrix $(\partial F/\partial U)$
a_1-a_4	Eigenvalues (A)
B	Jacobian matrix $(\partial G/\partial U)$
b_1-b_4	Eigenvalues (B)
C	Vector corresponding to inhomogeneous term in axisymmetric flow
c	Speed of sound
c_o .	Speed of sound in the lower pressure region
D_{max}	Major diameter of ellipse
D_{min}	Minor diameter of ellipse
E	Total energy (Pa)
E'	Dimensionless total energy
e	Internal energy (J/Kg)
F	Vector function of U in the radial direction
G	Vector function of U in the azimuthal direction
i	Space index in the radial direction
J	Number of mesh points in the azimuthal direction

j	Space index in the radial direction
K	Initial pressure ratio
K$'$	Initial density ratio
L_c	Splitting operator (inhomogeneous)
L_r	Splitting operator (radial direction)
L_θ	Splitting operator (azimuthal direction)
M_o	Initial Mack number
M_s	Shock Mack number
m	Azimuthal mode number
m	Harmonic number
n	Time step
P	Pressure
P$'$	Dimensionless pressure
P_o	Initial pressure at lower pressure region
R	Radius
R_a	Average radius
R_d	Diaphragm's radius
R_o	Initial radius
r	Radius
r$'$	Dimensionless radius
r_o	Mean radius of the diaphragm
t	Time

t'	Dimensionless time
t_o	Time parameter (r_o/u_o)
U	Vector function of conservative variables
u	Velocity component in the radial direction
u'	Dimensionless velocity component in the radial direction
u_o	Velocity parameter $(c_o/\sqrt{\gamma})$
V	Velocity vector
v	Velocity component in the azimuthal direction
v'	Dimensionless velocity component in the azimuthal direction

Greek symbols

α	Constant parameter
β	Constant parameter
γ	Specific heat ratio
δ	Amplitude (mode four)
θ	Azimuthal angle
λ	Difference operator
μ	Viscosity coefficient
ξ	Perturbation parameter (elliptical)
ξ_o	Initial perturbation parameter
ρ	Density

ρ'	Dimensionless density
ρ_0	Initial density in low pressure region
ϕ	Amplification factor (error)
ε	Error
ε	Amplification of the harmonic component (elliptical shock)

CHAPTER 1

Introduction

For solving today's engineering problems, the most used approaches are theoretical, experimental and numerical simulation. Many of the governing equations of the fluid dynamics do not permit an exact solution. Therefore, an appropriate solution in which based on rational arguments some terms are left out is employed. Another way to find approximate solutions is the use of dimensional analysis coupled with the experimental techniques to come up with some empirical relations. The availability of fast computers with large memories and at reasonable costs, enables one to seek numerical solutions to the governing equations. Such computer simulations are an efficient way to reduce the development time and concurrently study the problem from different angles with a marginal increase in cost. Other important advantage of numerical simulation is obvious in cases that, experiments are hard to carry out or dangerous, like: explosions. In such situations, an insight to the flow behaviour is achievable through numerical models.

In order to study the imploding shock wave, the facts above, promoted the idea of numerically modelling it. Details about the computational method and the results obtained from the study will be presented in the next chapters. The remainder of this

chapter will present the application of the imploding shock waves and a brief review of the previous works.

1.1 Some applications of imploding shock wave

Possibility of achieving high temperature and high pressure by means of an imploding shock wave have found a variety of scientific and engineering applications. Synthetic diamond is produced from graphite by placing the graphite in a steel container and exposing it to a focused implosion [1]. Also, focused shock waves are used in condensation of carbide or oxides gas cloud to form fine crystals [2]. Application of the imploding shock waves in the field of nuclear physics have led to the production of neutrons from deuterium-deuterium reactions [3]. This has been done through an explosion-driven implosion to produce fusion at the focus. Another interesting use of imploding shock waves is in the hypervelocity launchers. The speeds, as high as, 5.4 Km/S was actually obtained for an 8 mm diameter projectile [4,5]. In astronomy, the study of converging shock, has been used to describe the triggering mechanism for star formation through fragmentation of the shock compressed regions [32].

For such applications, investigation of the basic aspects of implosion phenomena is required. To meet this requirement, in the past few decades several analysis have been done through theoretical, experimental, and numerical studies.

1.2 Different approaches in studying converging shock waves

1.2a Theoretical studies

Converging spherical and cylindrical shock waves were investigated theoretically some fifty years ago by Guderley [6]. In his study, Guderley has shown that a weak symmetrically converging shock wave can increase in strength in the vicinity of the focus at which infinity high temperature and pressure are found. This however would not happen in reality, since the perfect symmetry does not exist in actual cases and the effect of viscosity or heat conduction will cause the pressure and temperature to remain finite. Based on Guderley's work, other analytical solutions were found for the problem of imploding shocks by Butler [7], Lighthill [8], Stanyukouvich [9], and Whitham [10]. Butler and Whitham in their work indicated that any small perturbation of the shock front will translate in an unstable convergence. This means that a small perturbation amplifies during the course of convergence. In the continuation of the theoretical investigation, Chester [11-13] introduced a linear analysis of the motion of a shock wave propagating in a tube having a small variation in its cross section. Through his analysis, Chester obtained a relation in differential form between the average shock wave strength and the cross sectional area. Using the basic concept of Chester's work, Chisnell [14] found a similar relation with a better approximation. Later, Whitham [15] using the characteristic form of conservation equations, reached a similar result as Chester and

Chisnell. The merger of the three works is known as Chester, Chisnell, and Whitham relation or CCW theory. The CCW theory is of particular interest, since in the case of a converging shock wave, the area is constantly decreasing and this reduction in area has a direct effect on the shock strength.

1.2b Experimental studies

To verify the theoretical studies and at the same time acquire a better understanding of dominant factors in the stability of the converging shock waves, several experiments have been preformed by various researchers. Perry and Kantrowitz [16] were among the first to produce and study the converging cylindrical shocks experimentally. With their Tear-drop configuration Perry et al. were able to generate a weak converging cylindrical shock. Experimentally, Takayama et al. [17] and Wanatabe et al. [18] both verified the theoretical prediction of Butler [7] and Whitham [10] about the amplification of the initial perturbation of the shock front. Traditionally, the stability of the shock is measured by examining the symmetry of the imploding shock wave. It is important to know the stability state of the imploding shock wave, because the final state of the gas at the focus depends directly on that. To achieve a highly symmetric shock wave, and consequently a stable one, Neemeh [19] and Wu et al. [20] used a three increment contraction configuration. Neemeh then observed a pair of vortices at the centre of collapse after the shock converged and he attributed this to a small asymmetry of the annular section of the shock tube.

4

So, a perfectly symmetric converging shock is yet to be produced. This implies that more studies in the basic mechanism of the imploding shock dynamics are needed for the production of a stable symmetric converging shock. Another approach that can give more insight to this problem is the numerical simulation of imploding shock waves.

1.2c Numerical studies

By the introduction of computers, scientists found another alternative to theoretical and experimental studies through numerical modelling of the problem. Study of the converging shock wave was no exception, and the first attempt to tackle the problem numerically was done by Payne [21]. He modeled the problem using a cylindrical diaphragm separating two regions of uniform gas at rest, but at higher pressure in the outside region. Then Payne obtained a one-dimensional solution based on Lax's method for the governing equations of an inviscid compressible gas without heat conduction. Later, Lapidus [22] and Abarbanel et al. [23] solved the converging cylindrical shock problem using the same model as Payne but with different versions of Lax-Wendroff scheme. Their simulation was a one-dimensional second order accurate modelling, and both of their simulation produced similar results. By using Glimm's random choice method, Sod [24-26] introduced a novel approach to solve the one-dimensional equations of gasdynamics for a converging spherical or cylindrical shock wave. With his first order accurate method, Sod obtained a very

sharp shock front compared to Payne's first order accurate simulation. Among the other 1-D simulations for converging cylindrical shock, Yabe and Aoki [27] treated the problem by using a cubic-polynomial interpolation scheme of the finite difference family. Recently, a third order finite difference scheme was used by Shankar et al. [28] to model the converging shock in radiating gas. This simulation was one-dimensional and concluded that the effect of radiation heat transfer is to decrease the growth rate of shock strength as it propagates toward the axis. Matsuo et al. examined the various methods for numerical simulation of cylindrical converging shock [29]. They pointed out that favourable results were obtained by a second order scheme, particularly the MacCormack method with an artificial diffusion term. One of the latest one-dimensional simulation for a converging cylindrical imploding shock wave has been done by Srivastava et al. [30], in which they used an invariant difference scheme of Rusanov. The study included not only the moderate initial pressure ratios, but also pressure ratios up to a thousand.

Through experiments, it has been observed that a real imploding shock wave is not perfectly symmetric, so a one-dimensional simulation can not give a complete description of its properties. In the view of the spatial non-uniformity in the azimuthal direction a two-dimensional analysis is necessary. The first effort among only a few attempts reported on two-dimensional modelling of the converging cylindrical shock has been made by Itoh and Abe [31]. They used the same cylindrical diaphragm model as Payne [21], but with small sinusoidal perturbation imposed on the density

or the pressure of the external fluid. For the computation, Itoh et al. extended the 1-D scheme of Abarbanel et al. [23] to spatially two-dimension. Later, Munz [33] used a more realistic model of deformed diaphragm for the perturbation in the azimuthal direction. He used a MUSCL-type scheme as the computation method in both Cartesian and Cylindrical coordinates. Munz's simulation in Cartesian coordinates was not as accurate as the Cylindrical coordinates simulation. By using an explicit, second order finite difference method known as flux corrected transport (FCT), Kimura et al. [32] applied their simulation results to describe the mechanism for the formation of stars. A numerical simulation of converging cylindrical shock was made using TVD finite difference scheme in polar coordinates by Wanatabe and Takayama [18]. Their numerical results were in good agreement with their holographic interferometry pictures from experiment. Recently, Demmig et al. [34,35] introduced another way to model the problem of converging cylindrical shock wave. They used a "snapshot" of measured physical quantities of the wave at a specific time. In the model of Demmig et al. there is no diaphragm and the computation's initial conditions come from the digitized photo of the experiment's shock contour and the measured properties of the at the time of photography. Then the shock motion is followed to the centre with numerical simulation. The method of computation here is TVD finite difference. For more details of the modelling method one can refer to the reference [35].

1.3 Scope of this thesis

The focus of the present thesis is threefold. First, a one-dimensional simulation is made of an axisymmetric imploding shock wave. The results then, compared with other 1-D simulations and also CCW theory, were found to be satisfactory. The method used in this part is a second order MacCormack finite difference. The scheme has been applied to the spatially one-dimensional unsteady compressible Euler equations.

Second, after gaining confidence in the scheme through 1-D analysis, it has been extended to spatially two-dimension in polar coordinates to simulate a converging shock. In this part a deformed diaphragm model has been used. The results of this section are used to verify the amplification of initial disturbances during the course of convergence for the shock wave. A perturbation of mode four is used for this purpose.

Finally, a converging elliptical shock has been simulated numerically. It has been found that the amplification of the shock during its convergence can not be described by the simple power law R^{-n} [7,10]. Instead, a harmonic type of variation has been suggested for the amplification of the shock.

CHAPTER 2

Governing Equations and the Computational

Method

In this chapter the time dependent governing equations for the flow of an invicid, non-heat conducting compressible fluid, namely Euler equations will first be reviewed. In the second part of the present chapter, the numerical method used to simulate the converging shock wave in spatially one and two dimensional models are going to be discussed. Later in the third part, boundary and initial conditions for both one and two dimensional analysis will be presented. Finally, in the last section of this chapter we will have a brief look at the truncation error and stability of the scheme.

2.1 Governing equations

The problem of imploding shock wave is sufficiently well described by the Euler equations. The Euler equations are extracted from the Navier-Stokes equations by neglecting the viscous terms. The set of Euler equations is a system of non-linear hyperbolic equations. Although no fluid can really be considered invicid, the Euler equations provide a reasonable (especially when the Reynolds number becomes very large), but by no means complete estimate of the behaviour of a fluid. If in the

problem under investigation one sets aside the effects of heat conduction, body forces and also viscosity, then the time-dependent governing equations for a compressible fluid would take the following form:

conservation of mass

$$\frac{\partial \rho}{\partial t} + \nabla \cdot (\rho V) = 0 \qquad (2.1a)$$

conservation of momentum

$$\frac{\partial V}{\partial t} + (V \cdot \nabla) V + \frac{1}{\rho} \nabla P = 0 \qquad (2.1b)$$

conservation of energy

$$\frac{\partial E}{\partial t} + \nabla \cdot [(E + P) V] = 0 \qquad (2.1c)$$

Here, P and ρ stand for pressure and density respectively; t is the time; V is the velocity vector and E represents the complete energy of a unit volume of the gas. E can be described in terms of internal energy of a unit mass (e) and the kinetic energy as follows:

$$E = \rho (e + \frac{1}{2} V^2) \qquad (2.2)$$

in this study, the assumption is that the gas is calorically perfect, so the equation (2.3) holds for the gas, where γ is the specific heat ratio.

10

$$e = \frac{1}{\gamma-1} \frac{P}{\rho} \qquad (2.3)$$

In the next step, the set of equations in (2.1a-c) is cast in the two-dimensional polar coordinates by means of the vector notation that is more suited for analysis.

$$\frac{\partial U}{\partial t} + \frac{\partial F}{\partial r} + \frac{1}{r}\frac{\partial G}{\partial \theta} + \frac{1}{r}C = 0 \qquad (2.4)$$

Here, U is the vector function of conservative variables; F and G are the vector functions of U representing the flux of conservation variables in the radial (r) and the azimuthal (θ) directions respectively; C is the vector corresponding to an inhomogeneous term in the axisymmetric flow. They are given by

$$U = \begin{matrix} \rho \\ \rho u \\ \rho v \\ E \end{matrix} \qquad F = \begin{matrix} \rho u \\ \rho u^2 + P \\ \rho uv \\ u(E + P) \end{matrix}$$

$$G = \begin{matrix} \rho v \\ \rho vu \\ \rho v^2 + P \\ v(E + P) \end{matrix} \qquad C = \begin{matrix} \rho u \\ \rho(u^2 - v^2) \\ 2\rho uv \\ u(E + P) \end{matrix}$$

In the above vectors, u and v are the velocity components in the radial and

11

azimuthal directions respectively. The variables to be solved for are ρ, u, v, and E. Then the pressure could be found using equations (2-2) and (2-3) together with the primary solved variables (i.e. ρ, u, v, and E). Equation (2-4) is a hyperbolic system of conservation laws, since each of the Jacobian coefficient matrices, $A=\partial F/\partial U$ and $B=\partial G/\partial U$, has four real eigenvalues. For Jacobian A one has

$$a_1 = u \quad , \quad a_2 = u+c \quad , \quad a_3 = u \quad , \quad a_4 = u\text{-}c$$

where c is the speed of sound. Similarly for the Jacobian B

$$b_1 = v \quad , \quad b_2 = v+c \quad , \quad b_3 = v \quad , \quad b_4 = v\text{-}c$$

In the numerical computation one of the techniques to decrease the round-off errors of the computer calculation, is the use of non-dimensional variables. It also has the benefit of giving a broader interpretation to the results obtained and a more stable computation. In order to transform the equation (2.4) in to a dimensionless form, the following dimensionless (primed) quantities are defined. By the substitution of these non-dimensional quantities the equation (2.4) remains unchanged.

$$v' = \frac{v}{u_o} \qquad u' = \frac{u}{u_o}$$

$$E' = \frac{E}{P_o} \qquad t' = \frac{t}{t_o}$$

$$r' = \frac{r}{r_o} \qquad \rho' = \frac{\rho}{\rho_o} \qquad P' = \frac{P}{P_o}$$

where

$$u_o = \sqrt{\frac{P_o}{\rho_o}} = \frac{c_o}{\sqrt{\gamma}} \qquad t_o = \frac{r_o}{u_o}$$

For the converging shock wave modeled by using a diaphragm separating the high and low pressure regions (which is the case here in this study), r_o is the mean radius of the diaphragm; ρ_o and P_o are the initial density and pressure at the lower pressure region respectively, and finally c_o is the speed of sound at the lower pressure region. Hereafter, these non-dimensional variables will be used and the primes will be omitted for the sake of convenience.

Now, the Euler equations have the desired form that is suited for the computation. In the next section, with the Euler equations properties (non-linearity and hyperbolicity) in mind, a reasonably accurate scheme for the solution of the set of equations will be discussed.

2.2 Numerical computation

Generally the numerical computation of a problem is composed of three parts. First, the preprocessing stage which includes the discritization of the domain of computation and mesh generation. Second, the processing stage in which the discritized equations will be solved. Finally at the last step, namely post-processing,

necessary gradients and other required quantities were calculated from primary variables. Also if needed, graphical representation of the results will be accomplished in this stage.

In the present thesis, the discritization of the governing equations has been done through finite difference formulation and the flow domain has been modeled as follows: when t=0, initially at $r=r_0$ a diaphragm separates the two regions of high and low pressure gas. Both inside low pressure and outside high pressure gases are isothermal and at rest. At time equal to 0^+ the diaphragm ruptures and the emergent shock wave moves toward the centre. The computation domain and the mesh for the spatially one-dimensional simulation of a symmetric converging shock is shown in figure (2.1). The mesh size for one dimensional model is chosen to be 1/200. For the two-dimensional simulation of imploding shock wave with the geometry of the flow in mind, the grid shown in fig. (2.2) has been suggested. The grid has 301 points in radial and 101 points in azimuthal directions respectively. This grid configuration approximately allows evenly spaced nodes at the average radius of the grid where the diaphragm has been positioned. As it can be seen from fig. (2.2) the nodes are more clustered as they get closer to the centre and improved results are expected in the vicinity of the axis. This is a natural advantage for the mesh, which is especially important since the gradients are getting larger as the shock gets closer to the centre.

In the processing stage, a Fortran program has been developed to solve for the

14

discritized domain and the resultant set of equations. The set of equations have been solved using a two-step MacCarmack second order accurate scheme. The details of the scheme and how it has been applied to the one and two dimensional cases will be examined in the proceeding section. The hardware used to carry out the computation is the Vax-4000 model 500 system at Concordia University.

At the post-processing step, in order to represent the results graphically, mainly two softwares were used: Surfer[1] and Matlab[2]. The three dimensional and contour plots were obtained using the Surfer and 2-D plots were obtained by programming in Matlab.

2.2a Numerical scheme

There is a vast variety of numerical schemes available for one to chose from. Depending on the problem in hand and the accuracy required and also the computing facilities available, a suitable scheme can be chosen or developed. In the case of this work, since the flow is unsteady the scheme should be able to advance in time, so a time marching method is the right choice. Furthermore, the presence of the shock wave in the flow under investigation requires a shock capturing method. In the so

---

[1] Surfer Access System, Version 4.00, © Golden Software Inc. 1989.

[2] Matlab version 3.5h, © The Networks Inc., 1984-1992

15

called "shock capturing" methods [36], the use of artificial (or sometimes called numerical) viscosity in association with the gas dynamics equations leads to the smearing of discontinuities raised from the shock presence. In this way the shock wave and the contact surface appear as a very narrow region with large gradients which resolves in two or three mesh size widths. As far as accuracy is concerned, the finite difference approximation of the differential equations can be first, second, third, or even higher order. Each of these levels of accuracy has its own advantages and disadvantages. For example, a first order accurate scheme is monotonous near the strong discontinuities but it gives a relatively wide shock representing zone in the solution (dissipation errors). The schemes of even order and particularly second order have problems with the dispersion errors (the small oscillations in the vicinity of discontinuities). Nevertheless, the second order schemes result in a narrow transition zone representing the shock wave. Figure (2.3) illustrates the effects of dissipation and dispersion errors on the computation of a discontinuity. A third order scheme possesses the best properties of the two preceding schemes but implementation of the boundary conditions in the scheme is troublesome. The complication in the boundary conditions arises from the fact that a larger number of points at time t is required to calculate a point at time $t+\Delta t$. Experience with the numerical methods [29,36,37] indicates that in many cases including the present simulation, the optimum scheme is a second order accurate one. Selecting a method for simulation also depends on the available computing facilities. For instance, if the computer in use has parallel computing capabilities, one should use a method that takes the full advantage of this

16

feature. However, in the case of this study the available computer was equipped only with a single processing unit and the selection of the method is in accordance with that factor.

Considering all the discussions above and trying to avoid complications in the simulation task, the decision has been made to use an explicit two-step scheme of MacCarmack [38-41]. This scheme is second order accurate and implementation of the artificial viscosity to capture the shock is fairly simple. First, in order to state the scheme clearly a one-dimensional version is presented here.

The unsteady one-dimensional axisymmetric Euler equations in the vector form is written as below:

$$\frac{\partial U}{\partial t} + \frac{\partial F}{\partial r} + \frac{1}{C} = 0 \tag{2.5}$$

The two-step MacCarmack method consists of a forward difference predictor step and the proceeding backward difference corrector step. The application of the method to the equation (2.5) would result in the following form:

$$\overline{U_i} = U_i^n - \frac{\Delta t}{\Delta r} \lambda^+ F_i^n - \frac{\Delta t}{r} C_i^n \tag{2.6}$$

$$U_i^{n+1} = \frac{1}{2} (\overline{U_i} + \frac{\Delta t}{\Delta r} \lambda^- - \frac{\Delta t}{r} \overline{C_i})$$

where

17

Forward difference operator: $\quad \lambda^+ F_i = F_{i+1} - F_i$

Backward difference operator: $\quad \lambda^- F_i = F_i - F_{i-1}$

In the above equations, the subscript i indicates the spatial mesh point with the Δ r spacing distance, and the superscript n refers to time, t=nΔ t, where Δ t is the time increment that the solution is advanced in each cycle of calculations. The vectors with bars are the first approximation that later in the corrector step will be modified to the final value for the current time interval. Figure (2.4) denotes the schematic for the space-time index.

In theory, the finer Δ r (Δ r $\rightarrow$ 0) is, the better the result would be. However, from a practical point of view there should be a sensible limit for Δ r. In this study, Δ r is chosen to be 1/200. A considerable improvement in results has been observed for Δ r = 1/200 over the larger values (e.g. 1/100), but for increments less than 1/200 (e.g. 1/300 and 1/400) there is not a noticeable enhancement in results. Moreover, for the Δ r = 1/200 the computing time is significantly shorter than for the smaller values of Δ r. In order to choose the right Δ t, one should consider the limit that has been dictated by the stability criteria for the scheme. More elaboration on this matter would appear later in this chapter.

The severe pressure changes associated with the strong shock wave produces large oscillations in results in the vicinity of the shock wave. Unfortunately, the use of the scheme described earlier in its present form often leads to unstable

computation. To suppress oscillations in the numerical results an artificial viscosity term is added to the above scheme. The form and size of this artificial viscosity is often determined by numerical experiments. The inclusion of the artificial viscosity in the current work has been explicit and takes the following form:

$$\Delta U_i^D = \Delta U_i - \mu (U_{i-1} - 2U_i + U_{i+1})$$

where

$$\Delta U_i = U_i^{n+1} - U_i^n$$

and the final value is

$$(U_i^{n+1})^D = U_i^n + \Delta U_i^D$$

In above, the superscript D represents the damped value for ΔU_i and U_i^{n+1}; μ is a constant that has been found by numerical experimentation. The result of the computation was sensitive to the viscosity coefficient (μ). If the μ is too small, then the scheme would become unstable. On the other hand, if viscosity was too large, it leads to smearing out the shock and contact surface. Additionally, the determined viscosity coefficient (μ) was dependent on the initial pressure ratio. For the initial pressure ratio of 4, to start the computation the value for μ has been chosen to be 0.09. After the shock wave has traveled about 15 percent of its path toward the centre, the value for μ is reduced to 0.05 to get a sharper shock front. The results of the described scheme applied to a converging cylindrical shock will be discussed in chapter three.

Now, in order to illustrate the method in two dimensions (r and θ), the scheme has been applied to equation (2.4). The implementation of the numerical scheme to equation (2.4) has been done using the operator splitting technique[1]. In this technique, the multi-dimensional solution is evolved from a factored sequence of one-dimensional operators. In other words, the equation (2.4) is broken down to three parts and each part is solved separately using an operator. The two one-dimensional equations and the inhomogeneous term are as follows:

$$\frac{\partial U}{\partial t} + \frac{\partial F}{\partial r} = 0$$

$$\frac{\partial U}{\partial t} + \frac{1}{r} \frac{\partial G}{\partial \theta} = 0 \qquad\qquad (2.7)$$

$$\frac{\partial U}{\partial t} + \frac{1}{r} C = 0$$

and the three corresponding operators are

$L_r(\Delta t)$:

$$\overline{U_{ij}^n} = U_{ij}^n - \frac{\Delta t}{\Delta r} \lambda^+ F_{ij}^n$$

$$U_{ij}^* = \frac{1}{2}(U_{ij}^n + \overline{U_{ij}^n} - \frac{\Delta t}{\Delta r} \lambda^- \overline{F_{ij}^n}) \qquad\qquad (2.8a)$$

---

[1] The concept of splitting is credited to Peaceman and Rachford. "The Numerical Solution of Parabolic and Elliptic Differential Equations",SIAM J.,Vol. 3,1955,PP.28-41.

$L_\theta(\Delta t)$:

$$\overline{U_{ij}^\bullet} = U_{ij}^\bullet - \frac{1}{r}\frac{\Delta t}{\Delta\theta} \lambda^+ G_{ij}^\bullet$$

$$U_{ij}^{\bullet\bullet} = \frac{1}{2}(U_{ij}^\bullet + \overline{U_{ij}^\bullet} - \frac{1}{r}\frac{\Delta t}{\Delta\theta} \lambda^- \overline{G_{ij}^\bullet})$$

(2.8b)

$L_c(\Delta t)$:

$$\overline{U_{ij}^{\bullet\bullet}} = U_{ij}^{\bullet\bullet} - \frac{1}{r}\Delta t \, C_{ij}^{\bullet\bullet}$$

$$U_{ij}^{n+1} = \frac{1}{2}(U_{ij}^{\bullet\bullet} + \overline{U_{ij}^{\bullet\bullet}} - \frac{1}{r}\Delta t \, \overline{C_{ij}^{\bullet\bullet}})$$

(2.8c)

To maintain a second order accuracy the operators L_r, L_θ, and L_c should be applied to U_{ij}^n in a symmetric sequence. Therefore:

$$U_{ij}^{n+2} = L_r \, L_\theta \, L_c \, L_c \, L_\theta \, L_r (\Delta t) \, U_{ij}^n$$

(2.9)

The reason for applying the operators in a symmetric sequence to achieve the second order accuracy is analyzed in detail by MacCarmack [39].

As it has been mentioned earlier a grid in cylindrical coordinates with 301 × 101 nodes in the r-θ plane has been used for numerical calculations (fig. 2.2). To have a more efficient simulation for elliptic imploding shock, a quarter of the grid has been used and a mirror image boundary condition is applied to both sides of this sector. In the case of a perturbed cylindrical shock, the perturbation is generated with a cosine curve corrugation [Cos(mθ)] to the diaphragm, where m is the azimuthal mode number. Since the perturbation is periodic in the azimuthal direction with a period of 2π/m, the computation is performed in a sector with the central angle of

21

$2\pi/m$ to achieve the maximum efficiency. The periodic boundary conditions at both sides of this sector are adopted.

Again, the time step for the numerical computation in two dimensions is dependent on the stability criteria for the two-dimensional method. Moreover, since a splitting technique has been used, consideration should be given to advance the time in the both directions (r,θ) equally. This does not mean the time steps for r and θ could not be different. However, it indicates that the total advancement of time for each direction should be equal in any cycle of calculations.

The artificial viscosity in the present work is applied only to the L_r operator. The reasoning for this matter is based on the fact that the flow experiences the discontinuity only in the radial direction. So, the unnecessary use of artificial viscosity has been avoided for the other direction (θ). The implementation of the viscosity term for the L_r operator is similar to the one-dimensional case. In this way, the damped value of variables (i.e. Vector U_{ij}^P) should be used as the input for L_θ operator instead of U_{ij}^* in equation (2.8a).

2.2b Initial and boundary conditions

In this section the initial and boundary conditions employed are described. Initially, when $t=0$, the conditions for the one-dimensional model of a cylindrical

converging shock is given by

$$u_i^0 = 0 \qquad\qquad\qquad \text{for all radii}$$

$$P_i^0 = 1 \, , \; \rho_i^0 = 1 \qquad\qquad\qquad r \langle r_0$$

$$P_i^0 = K \, , \; \rho_i^0 = K' \qquad\qquad\qquad r \rangle r_0$$

$$P_i^0 = (K+1)/2 \, , \; \rho_i^0 = (K'+1)/2 \qquad\qquad r = r_0$$

where r_0 is a constant representing the radius of the diaphragm; K and K' are pressure

ratio and density ratio respectively. In this work K and K' are chosen to be equal to

4. Additionally, for the initial conditions of a two-dimensional imploding shock, one

has

$$v_i^0 = 0 \qquad\qquad\qquad \text{for all radii}$$

Also it should be noticed that for a perturbed converging cylindrical shock, r_0 ·

is not a constant any more, since the radius of the diaphragm (r_0) varies in accordance

with the following cosine perturbation:

$$r_o = r_o(\theta = \frac{\pi}{2}) \, [1 + \delta \, \cos(m \, \theta)] \qquad\qquad (2.10)$$

where δ is the amplitude and m is the mode number in azimuthal direction. The above

form of perturbing a converging cylindrical shock is almost similar to what Munz [33]

has suggested. The three different values for δ in this study are 0.02, 0.03, and 0.04

with the mode number m=4. Moreover, in the case of an elliptic imploding shock

wave the variation of r_0 is given as a function of perturbation parameter (ξ) and the

azimuthal angle in the following form:

23

$$r_o = \sqrt{\frac{r_o(\theta = 0)}{\xi \sin(\theta)^2}} \qquad (2.11)$$

where the perturbation parameter (ξ) is

$$\xi = \frac{D_{max} - D_{min}}{D_{max} + D_{min}} \qquad (2.12)$$

In above, D_{max} and D_{min} are denoting the major and minor diameters of ellipse. The two values for ξ are chosen to be 0.0415 and 0.064. Finally, it is assumed that the rupture of the diaphragm is instantaneous and uniform.

In order to impose the boundary conditions to a problem, first the domain of computation should be defined. Actually, the problem in hand has a semi-infinite domain (i.e. $0 \leq r < \infty$), however, for the computational purposes one must specify a finite domain. Traditionally, the domain of numerical computation for an imploding shock wave is chosen to be a circle with a radius twice as the radius of diaphragm separating the higher and lower pressure regions initially. Here as well the same domain is respected, so with the diaphragm radius equal to 0.5, the domain of computation would be $0 \leq r \leq 1.0$.

Having defined the domain of calculation, now the conditions at the boundaries (i.e. r = 1.0 and r = 0) should be discussed. The boundary conditions at r = 1.0 are fairly simple and the values of the variables for t = (n+1) Δt have been found

from their values at $t = n\Delta t$ using a second order extrapolation. For instance, if the pressure is considered, then its value at $r = 1+\Delta r$ could be acquired using the Lagrange method [23] as follows:

$$P^n_{r=1+\Delta r} = P^n_{r=1-2\Delta r} - 3P^n_{r=1-\Delta r} + 3P^n_{r=1}$$

Now that the $P^n_{r=1+\Delta r}$ has been obtained, the value of $P_{r=1}^{n+1}$ could be found using the previously described MacCarmack scheme. The boundary conditions at $r = 0$ need more attention since $r = 0$ is a singular point in the domain of computation. It is clear that both components of velocity are zero at the axis ($r = 0$). In addition, density and pressure are indeterminate of the type 0/0 at the centre that makes $r = 0$ a singular point. An extrapolation technique can not be used to exclude the singular point from computation, because of very large gradients near the axis. So to calculate the density, energy, and consequently pressure at the centre, the conservation laws should be used. To find the density at the axis the conservation of mass in its integral form has been used as follows:

$$\frac{\partial}{\partial t}\iiint_{cv} \rho\, d\upsilon + \iint_{cs} \rho V dA = 0$$

Considering the control volume (υ) shown in figure (2.5) with a radius of Δr one has

$$d\upsilon = r d\theta dr \qquad , \qquad dA = \Delta r d\theta$$

so the preceding integral equation takes the form of

$$\frac{\partial}{\partial t}\iint_0^{\Delta\theta} \rho r dr d\theta + \int_0^{\Delta\theta} \rho u \Delta r d\theta = 0$$

25

In the above formulation the azimuthal component of velocity (v) is ignored, because in comparison with the radial component (u) it is very small. After the integration and considering only the first order accuracy that results in less oscillations near the axis, one has

$$\rho_{r=0}^{n+1} = \rho_{r=0}^{n} - 2\frac{\Delta t}{\Delta r} \, \rho_{r=\Delta r}^{n} \, u_{r=\Delta r}^{n}$$

With the same argument and this time considering the conservation of energy, the value of E can be obtained at the axis using

$$E_{r=0}^{n+1} = E_{r=0}^{n} - 2\frac{\Delta t}{\Delta r} \, u_{r=\Delta r}^{n} \, (E_{r=\Delta r}^{n} + P_{r=\Delta r}^{n})$$

Now the pressure at the axis can be found by using equations (2.2) and (2.3). To find the gas properties at the centre in the case of a two-dimensional simulation, the following form is suggested to obtained ρ and E:

$$\rho_{r=0}^{n+1} = \rho_{r=0}^{n} - \frac{1}{J} \, \Sigma_{j=1}^{J} \, 2\frac{\Delta t}{\Delta r} \, [\rho_{r=\Delta r}^{n} \, u_{r=\Delta r}^{n}]_{j}$$

$$E_{r=0}^{n+1} = E_{r=0}^{n} - \frac{1}{J} \, \Sigma_{j=1}^{J} \, 2\frac{\Delta t}{\Delta r} \, [u_{r=\Delta r}^{n} \, (E_{r=\Delta r}^{n} + P_{r=\Delta r}^{n})]_{j}$$

where J is the number of mesh points in the azimuthal direction.

As it has been discussed previously, in order to save the computation time, a sector of a circle is used as the computation domain (see fig. 2.6). At the two sides, OA and OB, the symmetry conditions must be fulfilled. They are

26

$$v = \frac{\partial \rho}{\partial \theta} = \frac{\partial u}{\partial \theta} = \frac{\partial E}{\partial \theta} = 0$$

To satisfy the above conditions one additional ray is introduced at each side of the domain (i.e. OA and OB) outside of the calculation region. The value of variables at each of these auxilary mesh points are obtained from interior points by considering the symmetry of the flow. In the process of transferring the data from the interior region to the outside mesh points, one should remember that the velocity component normal to the boundaries (v) changes its sign. This way of implementing the boundary conditions for a symmetrical flow is often called "mirror imaging" [36].

2.2c Error analysis and stability of the scheme

The error in a simulation task like the one under consideration in this thesis can have several sources. The list for the sources of error in the computation includes: input errors, programming errors, round-off errors, and truncation errors. Here in this section, a brief review about the round-off and truncation errors are presented and the discussion about the other sources of errors are overlooked. Later in this part, a note on the stability of the scheme used for the numerical simulation and the criteria to have a stable computation will be given.

Round-off error (or sometimes called machine error) has roots in the fact that during a computation, a number in the computer could only be represented with a

27

fixed number of significant digits. Leaving out the rest of the digits due to this limitation results in an error that during the course of calculation could accumulate and sometimes lead to a wrong or unstable solution. In this work to minimize this type of error the double precision mode for the variables in the program has been used. Also the employed non-dimensional variables can help to reduce the effect of round-off error. Truncation error is the error corresponding to the fact that only a finite number of terms in a series or steps necessary to produce an exact result could be used and the rest of the terms or steps are truncated prematurely. For simplicity of presentation, here a one-dimensional Euler equation is considered and it has been shown that the application of MacCarmack scheme results in a second order accurate method. The Euler equation in Cartesian coordinates has the following form:

$$\frac{\partial U}{\partial t} = -\frac{\partial F}{\partial x} \tag{2.13}$$

By applying the MacCarmack method to the above equation one has

$$\overline{U_i} = U_i^n - \frac{\Delta t}{\Delta x} \lambda^+ F_i^n \tag{2.14}$$

$$U_i^{n+1} = \frac{1}{2}(U_i^n + \overline{U_i}) - \frac{\Delta t}{2\Delta x} \lambda^- \overline{F_i} \tag{2.15}$$

Substitution of $\overline{U}_i$ from equation (2.14) into eq. (2.15) gives

$$U_i^{n+1} = U_i^n - \frac{\Delta t}{2\Delta x} \lambda^+ F_i^n - \frac{\Delta t}{2\Delta x} [F(U_{i+1}^n - \frac{\Delta t}{\Delta x} \lambda^+ F_{i+1}^n) \\ - F(U_i^n - \frac{\Delta t}{\Delta x} \lambda^+ F_i^n)] \tag{2.16}$$

Expanding the F ($U_{i+1}^n - \Delta t/\Delta x \, \lambda^+ F_{i+1}^n$) by means of a Taylor series would result

28

in

$$F(U_{i+1}^n - \frac{\Delta t}{\Delta x} \lambda^+ F_{i+1}^n) = F_{i+1}^n - [\frac{\Delta t}{\Delta x} \lambda^+ F_{i+1}^n] F_{i+1}^{n'} + HOT$$

Similarly treating the $F(U_i^n - \Delta t/\Delta x \lambda^+ F_i^n)$ and substituting the outcome into equation (2.16) gives:

$$U_i^{n+1} = U_i^n - \frac{\Delta t}{2\Delta x} (F_{i+1}^n - F_{i-1}^n) - \frac{\Delta t^2}{2\Delta x^2} (F_{i+1}^{n'} \lambda^+ F_{i+1}^n - F_i^{n'} \lambda^+ F_i^n) + O(\Delta^3)$$

The equation above confirms the second order accuracy of the scheme, since the difference between this formulation and a direct expansion of equation (2.13) via Taylor series to the form below is of Third order.

$$U_i^{n+1} \approx U_i^n + (\frac{\partial U}{\partial t})_i^n \Delta t + (\frac{\partial^2 U}{\partial t^2})_i^n \Delta \frac{t^2}{2}$$

Hence

$$\frac{\partial}{\partial t}(\frac{\partial U}{\partial t}) = -\frac{\partial}{\partial x}(\frac{\partial F}{\partial t}) = -\frac{\partial}{\partial x}(F'(U)\frac{\partial U}{\partial t}) = \frac{\partial}{\partial x}(F'(U)\frac{\partial F}{\partial x})$$

It is worth noticing that a truncation error of $O(\Delta^2)$ means; for instance, by halving the space increment (Δx), it approximately quarters the error caused by treating the problem in a series of finite terms. However, this enhancement in grid points results in the larger round-off errors. Therefore, a balance between truncation and round-off errors should be reached. Moreover, these errors influence greatly the stability of every numerical algorithm. So, in order to bound the error, appropriate restrictions which ensure the stability must be implemented.

The stability of the solution for a non-linear equation like the one under consideration (i.e. Euler equations) can not be analyzed completely. The most successful approximate analysis can be achieved by first linearizing the equation. Then, the linear equation's stability can be studied using von Neumann's analysis [42,43]. The principle of the von Neumann analysis is based upon studying the propagation of an error in the initial values. In the analysis, first a small error is introduced in the equation (e.g. second order wave equation $\partial^2 z / \partial t^2 = c^2 \; \partial^2 z/\partial x^2$) and in the second step, this new equation is subtracted from the original error free equation. The result is the error equation which, due to the linearity of the considered partial differential equation, is the same as the original equation (i.e. wave equation). This error equation is shown in its discritized form

$$\frac{\epsilon_i^{n+1} - 2\epsilon_i^n + \epsilon_i^{n-1}}{\Delta t^2} = \frac{\epsilon_{i+1}^n - 2\epsilon_i^n + \epsilon_{i-1}^n}{\Delta x^2} \qquad (2.17)$$

Next, the error $\epsilon(x,t)$ is expanded using Fourier series as

$$\epsilon(x, t) = e^{\alpha t} e^{i\beta x} \qquad (2.18)$$

where β is any real value and α is a function of β and may be complex. The term e^{α} is often called amplification factor φ. By substituting (2.18) into (2.17) one obtains

$$e^{\alpha \Delta t} = 1 - 2\varphi^2 \sin\frac{\beta \Delta x}{2} \pm \sqrt{(1 - 2\varphi^2 \sin\frac{\beta \Delta x}{2})^2 - 2} \qquad (2.19)$$

where $\varphi = c \, \Delta t/\Delta x$ is called the Courant number. Since $\epsilon_i^n = e^{\alpha \Delta t} \epsilon_i^{n-1}$ for any β in the solution for error, and $\sin(2\beta \Delta x/2)$ is at most equal to one, it is obvious that

30

the general Fourier component of error will not grow from one time step to another, if $\left| e^{\alpha \Delta} \right| \leq 1$. Therefore, considering the equation (2.19), it becomes clear that the stability requirement for the explicit scheme is $\Delta t = \Delta x / c$. In the stability analysis of a system of differential equations, instead of an amplification factor, one would get an amplification matrix. Thus, with a similar analysis for the system of difference equations that of this simulation, the following stability condition for the explicit two-dimensional Euler solver would become

$$\Delta t \leq \min \left(\frac{\Delta x}{|u| + c} , \frac{\Delta y}{|v| + c} \right)$$

in which $c = \sqrt{\gamma P / \rho}$ is the local speed of sound.

In practice, due to insufficient assumption of linearity, the value of Δt obtained from the above condition should be multiplied by a factor less than one. By experimenting with different coefficients and keeping in mind that the largest coefficient would result in a more efficient computation, a factor of 0.87 is chosen. It has been observed that in the case of a two-dimensional simulation, as a shock wave gets closer to the centre the stability of the scheme is deteriorated and a smaller factor (0.3) has been used to assure the stability of computation in the vicinity of the axis. This deterioration in stability could correspond to the larger gradients near axis showing perhaps the need for more clustered mesh points. Another element that is important for the selection of the multiplication factor is the initial pressure ratio. During the course of this work different initial pressure ratios have been chosen and

31

it has been noticed that the higher the initial pressure ratio is the smaller the multiplication factor should be.

CHAPTER 3

Application of the Numerical Algorithm

to Implosions

This chapter discusses the results obtained from application of the previously described numerical scheme to simulate the imploding shock waves. At first a one-dimensional simulation has been carried out for perfectly symmetric converging cylindrical shock waves and the results have been compared with CCW, characteristic method, and some other finite difference methods. Also the numerical results for the variation of the shock Mack number versus the radius of the shock were compared with the experimental data. In the second part of the present chapter, the results from a two-dimensional simulation of an imploding shock wave are examined. The study has been conducted for two cases of perturbed cylindrical shock waves. The amplification of the shock wave distortion is examined through the perturbation parameter and findings were compared with recently obtained experimental results. A detailed description of the study is presented in the following sections.

3.1 One-dimensional study

As it has been mentioned before in order to study the imploding shock wave,

it has been modeled using a circular diaphragm separating the regions with different pressures. It is assumed that the outside region's pressure is higher than the inside zone. Further, it is presumed that the density ratio of the two regions is the same as the pressure ratio that ultimately would result in the uniform temperature across the two zones. Since in this section the focus is on the one-dimensional study of the implosion phenomenon, everything including the gas properties and the geometry of the flow and the domain of the computation is uniform in the azimuthal direction. Finally, the last two assumptions are: (a) the gases in both regions are initially at rest, and (b) the specific heat ratio γ is constant at all the times in the calculations and it is equal to 1.4. Figure (3.1) illustrates the schematic of the discussed model.

At time $t = 0^+$, the diaphragm is ruptured and a series of compression waves rapidly emerge into a converging cylindrical shock wave. The wave propagates at supersonic speed in the lower pressure region as it can be seen from fig. (3.2a,b). The motion of the shock wave sets the gas behind it in motion in the same direction as the shock velocity. At the same time a rarefication wave originates at the diaphragm section and propagates in the opposite direction into the higher pressure region. The shock wave and the rarefication wave interact in such a manner to establish a continuous pressure and velocity profile for the gas downstream of these waves (see fig. 3.2a,b). However, the gas in the region between the shock wave and the rarefication wave does not have a continuous temperature throughout the whole region, since there is a sudden drop in the temperature (see fig. 3.2d). The drop in

34

the temperature can be described with the following argument. The laws of the normal shock dictate a sudden increase in the temperature for the gas when a shock passes through it, and once the heated gas comes into the contact with the colder gas down stream of the rarefication wave a discontinuity in the temperature is inevitable. The surface at which these two hot and cold gases meet each other is called a contact surface (or contact discontinuity) and it is highly visible in figure (3.2c). The contact surface moves toward the axis with the local velocity of the gas.

The numerical results are presented graphically in figures (3.2a-l). In these graphs, convergence, reflection, and divergence of the cylindrical shock wave are shown ' the time intervals of 0.05. Here, the shock appears as a rapid variation in pressure which is approximately resolved in two or three mesh size widths. The contact surface appears as the second jump in the density in fig. (3.2c) and the rarefication wave is represented by the portion of the graph with large gradients at the radii larger than 100 in all the figures.

With a closer look at the pressure versus radius graphs (i.e. figs. 3.2a,e,i) one could notice that as time increases the shock propagates toward the axis and its strength increases with time. This is in general agreement with the Guderley's theoretical prediction [6] and also experimental observation of Perry et al. [16]. When the shock wave arrives at the axis it is reflected, its strength rises to a large but finite value and a diverging shock appears. In theory, at the axis the infinite pressure should

be reached. In the current simulation a significantly better approximation to the theory has been achieved compared to the other simulation efforts. For the same initial pressure ratio of 4, Sod [24] with his random choice method has reached a maximum pressure of just over 8 at the axis and Abarbanel et al. [23] with their Lax-Wendorff type scheme obtained a value of approximately 14 for the pressure at the very small radii. In the more recent work, Shankar et al. [28] by using a third order accurate Rusanov scheme also reached to a maximum of close to 14 for the pressure at the vicinity of the axis. For the same pressure ratio, 4 that is, in this work the maximum of over 21 has been reached for the pressure value close to the centre (see fig. 3.2e). The result of this numerical simulation obviously shows a closer agreement with the theory as far as the amplification of the pressure is concerned at the axis. Comparisons of the pressure at the axis for the different initial pressure ratios are difficult, since the great majority of the reputable results are presented for the case with the initial pressure ratio of 4. To validate the simulation results at a different initial pressure ratio the comparison has been made with some experimental data. Also, the variation of the shock Mack number versus the radius of the shock has been compared with CCW theory for higher pressure ratios. More elaboration on this matter will appear later in this section. Returning to our discussion concerning the figures (3.2a,e,i), it is also observed that the pressure at a given point behind the reflected shock wave decreases with time. The reason for this is the expansion of the shock wave and the gas behind it with time as the shock diverges.

The density and the temperature profiles are displayed in figures (3.2c,g,k) and (3.2d,h,l) respectively. There is a sudden increase in the density while the shock is passing through the gas but owing to the simultaneous temperature rise this increase in the density is not as high as the increase in pressure. Also, the contact discontinuity is clearly visible in the density profiles as the second sudden increase in the plot. The reason for the this second jump in the density could be found in the temperature versus radius plots (e.g. fig. 3.2d). An abrupt decrease in the temperature due to the colder gas dragged by the shock wave from the higher pressure region is the reason behind the second jump in the density profile. It can be seen from the figs. (3.3g,h) that the density and the temperature before the shock wave touches the axis are both increasing at a fixed point with time. This result from the simulation is quite expected since as it has been known theoretically and observed experimentally the strength of the shock wave increases as it converges toward the axis.

In figures (3.2b,f,j) the velocity distribution has been shown. The shock wave's speed accelerates as it travels toward the centre (see fig. 3.2b). This acceleration of the shock wave is due to the fact that the area decreases as the shock converges toward the axis. When the shock wave is reflected from the axis, the diverging shock wave has a relatively smaller absolute velocity. The positive sign here shows an outward direction. The reason for a smaller absolute velocity is that a diverging shock has been slow down by the rush of the gas coming onward to it as a result of the previously passed converging shock. Similar to the case of the pressure profile, at a

fixed point behind the converging shock wave the velocity increases with time and behind a diverging shock the velocity decreases with time.

In figures (3.3a-l) the variation of pressure, velocity, density, and temperature at constant radii with time have been shown (for initial pressure ratio of 4). The three fixed points are located at r=0.25, 0.50, 0.75. In all of the pressure versus time at constant radius graphs there are two jumps: the first one corresponds to the arrival of the converging shock wave to the point and the second one indicates the passage of the diverging shock wave. Moreover, it is clear that as the radius decreases the peak values of the curves are higher since the shock wave is stronger at smaller radii. The velocity versus time curves have two discontinuities as well. These discontinuities, like in the pressure versus time plots, correspond to the converging and diverging shock waves. However, the second discontinuity includes a change in the sign that shows the gas particles suddenly alter the direction of their motion due to the diverging shock. The general trend in the temperature and density variation with time at constant radius graphs, except for the r=0.75 curves, are similar to the pressure graphs. The exception in the graphs at r=0.75 is due to the fact that for the time range shown, the radius is large enough so the slower contact surface can pass through the point and affect the gas properties at that radius. In the density curves for the r=0.75 the second jump denotes the passage of the contact surface through the point as it can be confirmed from the corresponding temperature plot by observing the sudden drop in the gas temperature. Here the third jump is the indication of the

diverging shock wave.

In general, as it can be seen from the adopted graphs at the same initial conditions (see figs. 3.4a-h) which belongs to the references [21], [23], [24], [28], the overall trend of the results agree with those of this work. However, the superior results have been obtained as far as the contact discontinuity is concerned compared to the Payne's work [21] in which the contact discontinuity is barely noticeable. Furthermore, unlike the Shankar et al. [28] results, in the current simulation the shock wave is monotonous. Also as it has been discussed earlier, a distinguishably better approximation to the theory has been achieved in this work for the pressure at the vicinity of the axis compared to the other results shown in figs. (3.4a-h). Although the results of this simulation commonly agreed well with all the other results in the references, the speed of the shock appears to be slower as it is displayed in figure (3.5). In fig. (3.5) the shock radius versus time for the methods used in references [24] and [31] are compared with those of obtained here. The difference with random choice method [24] is justifiable since this method has the accuracy of order Δt, while the accuracy of MacCarmack's method is of order Δt^2. However, the slower speed compared to the results in the Itch et al. work [31] seems to be a characteristic of the scheme adopted in this thesis. This slower speed for the shock wave when using the MacCarmack method is also observed by Matsu et al. [29] in their comparison with the method of integral relations. All in all, sightly slower shock velocity is not a major problem since overall the results are acceptable and as it has

been mentioned in the Matsu et al. study of different methods for simulating the converging shock wave, particularly favourable results can be obtained by using the MacCarmack scheme.

In addition to verifying the outcome of the current simulation with the other simulations efforts as it has been discussed in the preceding paragraphs, the results have been compared with the experimental data as well. The experimental data have been extracted from the oscilloscope traces in Zitouni's work [44]. In order to minimize the boundary layer effects on data, the oscilloscope traces corresponding to the widest chamber have been used. Moreover, the selected data belongs to the set with the initial Mack number of 1.70. To find the initial pressure ratio for the simulation of the experiment, the following relationship has been used.

$$\frac{P_h}{P_l} = \frac{\gamma-1}{\gamma+1} \left[\frac{2\gamma}{\gamma-1} M_o^2 - 1 \right] \left[1 - \frac{\frac{\gamma-1}{\gamma+1}(M_o^2 - 1)}{M_o} \right]^{\frac{-2\gamma}{\gamma-1}}$$

In the above equation P_h and P_l are indicating the pressure at higher and lower pressure regions respectively and M_o is the initial Mack number. Using the preceding equation the initial pressure ratio is found to be 13.45. Figures (3.6a,b) show the results from the numerical simulation together with the available experimental data for the pressure versus time at two different radii. The overall trend of the simulation results are promising and the slight difference between the experimental data and the numerical results can be attributed to the fact that viscosity effects have been

40

overlooked in the simulation. The agreement between the numerical results and the experimental data is better at the smaller radius. This suggests that the errors in the numerical simulation are getting larger as more steps are involved in the calculations. At the higher pressure ratios a small oscillation appears behind the shock (e.g. fig. 3.6a). This oscillation as it has been said before, is a characteristic of the second order schemes and it can be omitted with the use of a larger artificial viscosity coefficient. However, here the large coefficient for the artificial viscosity is exchanged with a balanced one in order to keep the representing shock wave zone sharper and also to have a better accuracy in results.

The variations of the shock Mack number with the radius of the shock wave for two different initial pressure ratios have been displayed in figures (3.7) and (3.8a,b). To find the shock Mack number from the numerical results the following relation has been used.

$$M_s = \sqrt{\frac{\gamma+1}{2\gamma} \frac{P_2 - P_1}{P_1} + 1}$$

In the above equation P_1 and P_2 are the pressure in front and behind the shock wave respectively and M_s is the shock wave's Mack number. For the initial pressure ratio of four, the simulation results have been compared with those theoretically obtained by the CCW theory [10-15]. Remarkably good agreement was noticed between the theory and the numerical values at larger radii (see fig. 3.7). Deviation of the numerical data from the simplified CCW solution at smaller radii has mainly two

41

reasons. First, in our earlier discussion it has been mentioned that the shock waves speed calculated with the MacCarmack scheme tends to be slower at the vicinity of the axis. Secondly, the CCW solution itself is approximate since the effect of the secondary wave refection has been omitted in the derivation of the theory.

Now, in order to have a stronger representation of the results obtained for the variation of the shock Mack number versus the shock radius, the comparison has been made between the simulation results and those of CCW theory, characteristic method, and experimental data. Figures (3.8a,b) show the outcome for the initial pressure ratio of 13.45. Again the experimental data as well as the method of characteristic results have been adopted from Zitouni's work [44]. A reasonably good agreement between the method of characteristic (MOC) and the numerical results from this work with . those of the experimental data can be seen from fig. (3.8a). The deviation of the experimental data from the two other methods in the larger radii as it has been pointed out by Zitouni is the result of the multiple reflection of the characteristic wave as it passes through the area contraction in his experiment apparatus. So it can be considered as an error factor in the experimental data. Although in fig.(3.8a) at the smaller radii as it has been expected, the method used in this thesis results in slower shock Mack number compared to characteristic method, interestingly the experimental results agree very well with the outcome of the current work. In figure (3.8b) like the case with the initial pressure ratio of 4, at the larger radii the simulation results agree well with the CCW theory. However, the difference still remains in the smaller radii

for the reasons that have been mentioned before.

3.2 Two-dimensional study

In this section the results from a two-dimensional simulation for an imploding shock wave are analyzed. The discussion is threefold: first a 2D simulation with a one-dimensional initial condition is preformed, secondly, a mode four perturbation for a converging cylindrical shock is examined and in the third part an elliptical shock wave has been simulated. The outcomes from each of these simulations are discussed individually in the three proceeding sections.

3.2a One-dimensional initial conditions

All the assumptions for the one-dimensional simulation are held here and the only difference is that the spatially two-dimensional Euler equations have been used. In other words, the equation (2.4) has been used for the simulation and there is no perturbation in any of the fluid properties inside or outside of the diaphragm before its rupture. Moreover, the diaphragm itself does not have any deformity and it is a perfect circle (see figure 3.1). The purpose of this study is first to analyze the effects of the initial conditions on the results from a 2D simulation, in comparison with the solely one-dimensional model. Secondly, to see whether or not the affiliated errors in the calculations have any effect on the final results as far as the azimuthal direction

is concerned.

The results from this model in the form of the contour plots for the density are presented in figures (3.9a-d). The initial pressure and density ratios are chosen to be 4. In these figures the clustered iso-density contours with the smaller radius represent the shock wave and the second set of the clustered iso-density contours indicates the contact discontinuity. Furthermore, to appreciate the pressure intensification near the axis in figure (3.10) a 3D representation of the pressure at the convergence stage has been shown. It is worth noticing that the initial pressure ratio of three has been intensified more that 600 percent at the vicinity of the axis. The results of the numerical simulation as it can be seen from figures (3.9a-d, 3.10) show that the fluid's properties such as density etc. do not depend on the azimuthal angle θ. Also the shape of the shock wave remains circular at all times (i.e. before and after the convergence). From all of this one can conclude that if simulation starts with the one-dimensional initial conditions, there would not be any instability in the shock waves convergence. Moreover, since the outcome is independent of the azimuthal angle as it has been expected, it shows that the computational errors do not have a major effect on the final answer. The later finding is an advantage over MUSCL-type scheme of Munz [33], since in his simulation the computational errors caused a mode four perturbation at the convergence stage of the shock wave. Further, it appeared that the errors in Munz's simulation caused the contact surface to vanish when the shock wave was diverging. Now that confidence has been built that the computational errors are

not going to affect the study of the perturbed shock waves, we may proceed to the next section.

3.2b Mode four perturbation

There are several ways to produce a perturbation for the purpose of the numerical simulation of a converging cylindrical shock wave. The most realistic one is the method used by Demmig et al. [35], since they use the experimental data for the input of their program. However, it has the disadvantage of being useful only for the simulation of one specific experiment and it takes a lot of preparations. The other method, perturbing the density or pressure at the high pressure side of the diaphragm separating the high and low pressure gasses (i.e. creating the perturbation by high pressure regions used by Wanatabe et al. [18] or periodic perturbation of density used by Itoh et al. [31]) is very hard to achieve physically. It seems that corrugating the diaphragm in order to produce the perturbation is physically more sensible and in the same time is flexible enough to study the different cases. Such a scheme to generate the perturbation is first used by Munz [33], and an almost similar method has been used here to produce a mode four perturbation. The perturbation is applied by slightly corrugating the diaphragm using equation (2.10). No other perturbations of physical properties are added. Moreover, all the assumptions made in section 3.2a are valid here as well, except the diaphragm being circular. Figure (3.11) illustrates the schematic of the discussed model.

45

In order to achieve the maximum efficiency during the computation due to the symmetry of the flow, a sector with the central angle of $2\pi/m$ has been used. Here m is the mode number which in our case is 4. This means that the domain of the computation would be a quarter circle with the boundary conditions described in chapter two. The initial pressure and density ratios are chosen to be four in consistence with the previous cases in this study. The simulation results in the form of the iso-density contour plots for the cases with $\delta = 0.02$, 0.03, and 0.04 are shown in figures (3.13a-f), (3.14a-e), and (3.15a-e) respectively. The reason for using the iso-density contour plots to illustrate the outcome of the simulation is because all the experimental pictures display the change in the density at different regions. In this way a comparison between the patterns from experimental pictures and the numerical iso-density contour plots is possible.

At the beginning, as it can be seen from figs. (3.13a), (3.14a), and (3.15a) although different perturbation parameters (δ) were used, the shape of the shocks resembled one another. Also the iso-density contour patterns are almost the same. However, the initially small disturbances caused by slightly corrugating the diaphragm were amplified as the shock wave converged (e.g. see figs. 3.13a-e). Figure (3.13f) shows the reflected shock wave which becomes cylindrical with propagation outward and is known to be stable. By examining a series of the isopycnic plots, one can observe the time evolution of the gas flow. Although at the beginning the shock wave looked cylindrical, behind it a slight non-uniformity existed since the iso-density

46

contours were not cylindrical. The iso-density contours were quadrangularly disturbed which indicated the onset of mode four instability. For instance, as it can be seen from figure (3.14d) the shock wave is no longer cylindrical and the disturbance of the flow behind it becomes even more pronounced. In fig. (3.14e) the iso-density contours look like a " four-leaf clover". By comparing the results with the experimental pictures (see fig 3.16) taken from Watanabe's work [45] a remarkable agreement was found. It should be noted that there are some differences in the initial conditions between the experiment and the simulation (e.g. presence of the bend in the experiment apparatus). However, it is clear that the initial perturbation is amplified with shock convergence. Another example for the agreement between the experimental pictures and the outcome of this simulation can be seen in the figure (3.16a). The shadowgraph pictures belong to reference [48]. Figure (3.17) summarizes the amplification of the shock wave distortion. The solid curve represents the numerical results and the symbols are the selected experimental data from reference [45]. The Y axis is $\Delta R/R_a$, where the deviation of the shock wave ΔR is normalized with respect to average radius of the converging shock wave R_a. The X axis is the average radius normalized with respect to the radius of the diaphragm R_d. Some adjustments have been done to the experimental data since the characteristic length (diaphragm radius) in ref. [45] was different from the R_d in this work. As it can be seen, good agreement between the experimental data and the outcome of the numerical simulation was obtained. A small initial amplification rapidly grows when R_a /R_d is less than approximately 1.7. This can be attributed to the fact that an initially small perturbation

47

transforms to the triple points (two oblique shock and a cylindrical shock) as it can

be seen in the form of "four-leaf clover" pattern (e.g. figure 3.15e). Further, it is

found that the different perturbation parameters (δ) used have little effect on the

dimensionless $\Delta R/R_a$ versus R_a/R_d graph. Therefore, all of the three cases with

different δ have been merged into one curve in fig. (3.17).

3.2c Elliptical shock wave

In the last step of the present study for the first time a converging elliptical

shock wave has been simulated numerically. All the conditions and the assumptions

are the same as the mode four perturbation simulation except the shape of the

diaphragm. In this case the diaphragm is an ellipse given by the equation (2.11). The .

values for initial elliptical perturbation parameter (ξ) in eq. (2.11) are chosen to be

0.0415 and 0.064. Figure (3.12) displays the schematic for the current model.

The iso-density contour plots for the two cases of $\xi = 0.0415$ and 0.064 are

illustrated in figures (3.18a-e) and (3.19a-e) respectively. In figure (3.19a), in addition

to the shock wave and the contact discontinuity, a part of the rarefication wave can

be seen as well. Paying attention to how gas flow patterns are evolving in a series of

plots (e.g. 3.18a-e), one can observe that gas density rises at the most lagging part of

the shock front. This can be clearly seen in the blown-up plot of (3.18d). The more

clustered contours at the 90° and 270° positions, compared to wider spaced iso-density

contours at 0° and 180° locations, confirms the idea. This phenomenon can be explained as follows: when the gas flows into an oblique shock, the normal velocity component of the gas shrinks, while the tangential component is unchanged. Now, the stream line refracts when it approaches the shock front. Consequently, the compressed gas pours toward the lagging part of the shock wave. This compressed gas accumulates at the bottom of the concave front and forms a gas condensation there. A set of experimental pictures with the initial perturbation parameter equal to 0.065 has been displayed in the fig. (3.20). These pictures are taken from Tashtoush's work [46]. The resemblance of the numerical and the experimental pictures are very noticeable despite some differences in the initial conditions (e.g. the slight difference in the initial Mach number).

Very recently Neemeh et al. [47] through experiments found that the perturbation parameter ξ can not be represented by the simple power law relationship r^{-n}. Instead they have suggested a harmonic type of variation especially for the cases with large perturbations. In the reference [46] the following form has been proposed:

$$\xi = \xi_o (\frac{r}{R_o})^{-n} [1 + \epsilon \cos(m\pi \frac{r}{R_o})] \qquad (3.1)$$

where ξ_o is the initial perturbation parameter at R_o, ϵ is the amplitude of the harmonic component, and m is the harmonic number. Here we consider the characteristic radius R_o to be half of the diaphragm's major diameter (i.e. $R_o = 0.5$). It has been pointed out by Wanatabe et al. [18] that the normalized amplification

parameter for the shock wave is independent of the incident Mach number. So to verify the above equation numerically, ξ/ξ_0 versus r/R_0 representation is used. To plot the numerical curve, the information from both simulation cases are applied (i.e. ξ_0 = 0.0415 and 0.064). As it can be seen from figure (3.21) numerically the existence of the harmonic component for the amplification of the shock wave distortion has been confirmed. The simulation outcome is in very good agreement with the experimental results with the following parameters for the empirical equation (3.1):

$$m = 8$$

$$\varepsilon = 0.1$$

$$n = 0.8125$$

From the above result, a better understanding for the shock front perturbation has been obtained, and to some degree the reason behind the deviation of the experimental data from the theoretical prediction of r^{-n} is explained, as it has been mentioned by Neemeh et al [47].

CHAPTER 4

Conclusion and Recommendations

In this chapter the concluding remarks about the results obtained during the course of the present study have been pointed out. Furthermore, some recommendations for the continuation of this work in the future have also been suggested.

4.1 Conclusion

A numerical study was made of imploding shock waves. This simulation has been done through a second order explicit MacCarmack finite difference method by solving the unsteady compressible Euler equations. The study has been split into two parts. First, a one-dimensional model for the converging cylindrical shock wave has been simulated. Secondly, a two-dimensional simulation has been carried out for the mode four perturbation of the converging cylindrical shock wave and also for a converging elliptical shock wave. Based on the various results obtained, the following conclusions can be drawn.

It was shown that the MacCarmack difference method used in the present study

51

would be providing a useful tool other than experiment for furthering our understanding on such a complicated flow considered here. Moreover, employment of the splitting technique is a straightforward method to extend a one-dimensional scheme to multi-dimensional schemes. Further, the intelligible method of the initial set up used in the present computation (i.e. the deformed diaphragm) is capable of analysis of different perturbations and/or shapes for shock waves. Code used in this work has included these features.

In the one-dimensional simulation a reasonably sharp representation for the shock wave and the contact discontinuity has been obtained. Furthermore as it has been expected, numerically it was shown that the strength of the shock wave was increased while it was converging. Also a better approximation to the theory was achieved in this work compared to other simulation efforts at the vicinity of the axis as far as the pressure amplification is concerned. However, near the centre the shock velocity appeared to be a little slower compared to the results from other simulations. It was mentioned that this slower speed tends to be a characteristic of the method used in this study. Overall the computed shock Mack number versus radius results agreed well with the exact solution through the method of characteristic, approximate analysis of CCW, and some experimental results. At last, during the 1D study a satisfactory comparison between the experimental data and the numerical results has been made for the variation of pressure with time at constant radii.

From a 2D simulation but with a one-dimensional initial conditions, it has been concluded that if simulation starts with a 1D initial conditions there would not be any instability in the shock convergence. Moreover, since the results are independent of the azimuthal angle as it has been expected, it shows that the computational errors do not have a major effect.

Successfully a mode four perturbation for a converging cylindrical shock wave has been simulated. A remarkable agreement has been found between the numerical simulation's outcome in the form of the iso-density contour plots and the experimental pictures. Further, the amplification of the perturbation has been studied and the simulation results agreed well with those of experimental studies [45].

Finally, for the first time a converging elliptical shock wave has been simulated numerically. The numerical isopycnic plots well agreed with the experimental spark shadowgraph. Moreover, the amplification of the perturbation parameter for an elliptical shock has been studied. It has been concluded numerically that the variation of the perturbation parameter with the radius in fact has a harmonic component and can not be represented by the simple power law. This is in agreement with the very recent experimental and theoretical findings of Neemen et al. [47].

4.2 Recommendation for the future work

The present investigation has successfully achieved the objectives within the scope of this work. However, there is always some room for further development of the subject. The following are some suggestions for the future development on the problem considered in this thesis:

1. Further enhancement of the resolution of the flow field can be achieved by using solution-adaptive schemes.

2. A three-dimensional simulation can give more insight to the flow field through consideration of third dimension effects on the shock movement.

3. Incorporating the viscosity and boundary layer effects in the simulation of the shock wave.

4. Studying the diverging shock wave numerically and investigating the vortex formation at that stage.

5. At the very high initial pressure ratios the ionization of the gas due to severe heat generated at the focusing stage is an important factor that can be the subject of a additional study.

REFERENCES

[1] - Glass I.I., Sharma S.P.,"Production of diamonds from graphite using explosive-driven implosions", AIAA J., Vol.149, No. 3, 1976, PP. 420-404.

[2] - Strong G.,"Morphology of Carbon Particles formed by the Conically Converging Shock-Wave Tech. ", J. of Crystal Growth, Oct. 1988, Vol. 92, #1/2, PP. 143

[3] - Glass I.I.,"Over forty Years of Continues Research at UTIAS on Nonstationary Flows and Shock Waves", Vol. 1 , No. 1, 1991, PP. 75-86.

[4] - Flagg R.F.,"The Application of Implosion Wave Dynamics to Hypervelocity Launcher", UTIAS Rept. No. 125,1967.

[5] - Glass I.I.,"Appraised of UTIAS Implosion-Driven Hypervelocity Launchers and Shock Tubes ", Prog. Aero. Sci., 1972, No. 13, PP. 223-291.

[6] - Guderley G.,"Powerful Spherical and Cylindrical Compression Shocks in Neighbourhood of the Center of Sphere and the Cylindrical Axis",Luftahrtforschung, Vcl. 19, 1942, PP. 302-312.

[7] - Butter , D.S. , " The Stability of Converging Spherical and Cylindrical Shock Waves ", Armament research and Development Establishment, Rept.No. B 18/56, 1956.

[8] - Lighthill, M.J., "On the Defraction of Blast I ",Proc. Roy. Soc., 198A 1949,

P. 454.

[9] - Stanyukovich, K.P., " Unsteady Motion of Continuous Media",Gostekhzdat, Englo. Transl., Pregamon Press, N.Y., 1960.

[10] - Withham, G.B., " A New Approach to Problems of Shock Dynamics,Part I Two-Dimensional Problems ", J. Fluid Mechanics, Vol. 2, 1957,PP. 145.

[11] - Chester, W., " The Quasi-Cylindrical Shock Tube ", Phil. Mag., Vol.54,1954, PP. 1293-1301.

[12] - Chester, W., " The Propagation of Shock Waves in a Channel, With Applications to Cylindrical and Spherical Shock Waves ", J. Fluid Mech., Vol. 4, 1958, PP. 268-298.

[13] - Chester, W.,"The Propagation of Shock Waves along Ducts of Varying Cross Section", Advances in Appl. Mech., Vol. 6, 1960, PP. 119-152.

[14] - Chisnell, R.F.," The Motion of Shock Waves in a Channel, With Application to Cylindrical and Spherical Shock Waves ", J. of Fluid Mech.,Vol. 2, PP. 286-289.

[15] - Whitham, G.B.," On the Propagation of Shock Waves Through Regions of Non-Uniform Area or Flow", J. of Fluid Mech., Vol.4, PP. 337- 360.

[16] - Perry, R.W., and Kantrowitz, A., "The Production and Stability of Converging Waves", J. of Appl. Phy., Vol. 22, No.7, 1951, PP. 878-886.

[17] - Takayama,K. , Kleine, H., Gronig, H., "An Experimental Investigation of the Stability of the Converging Cylindrical Shock Waves in Air", Experiments in Fluids , Vol. 5, 1987, PP. 357-322.

[18] - Wanatabe, M., Takayama, K., "Stability of Converging Cylindrical Shock Waves", Shock Waves Int. J., Vol. 1, 1991, PP. 149-160.

[19] - Neemeh, R.A.,"Experimental Studies of Converging Cylindrical Shock Waves Produced by area Contraction", Ph.D. Thesis, McGill University, 1976.

[20] - Wu, J.H.T., Neemeh, R.A., Ostrowski, P, " Experimental Studies of the Production of Converging Cylindrical Shock Waves", AIAA J., Vol.18, 1980, PP. 47-48.

[21] - Payne, R.B.,"A Numerical Method for a Converging Cylindrical Shock", J. of Fluid Mech., Vol. 2 , 1957, PP. 185-200.

[22] - Lapidus, A.,"Computation of Radially Symmetric Shocked Flows", J. of Computational Phys., Vol. 8, 1971, PP. 106-118.

[23] - Abarbanel, S., Goldberg, M.,"Numerical Solution of Quasi-Conservative Hyperbolic Systems, The Cylindrical Shock Problem", J. of Computational Phys., Vol. 10,1972, PP. 1-21.

[24] - Sod, G.A.,"A Numerical Study of a Converging Cylindrical Shock", J. of Computational Phys., Vol. 10, 1972, PP. 1-21.

[25] - Sod, G.A.,"A Survey of Several Finite Difference Methods for Systems of Nonlinear Hyperbolic Conservation Laws", J. of Computational Phys.,Vol. 27, 1978, P.1.

[26] - Sod, G.A.,"A Numerical Methods in Fluid Dynamics", Press Syndicate of U. of Cambridge, 1985.

[27] - Yabe, T. and Aoki, T.,"A Universal Solver for Hyperbolic Equations by Cubic-Polynomial Interpolation, Part I", Computer Phys. Comm.,Vol.66, 1991,PP. 219-232.

[28] - Shankar, R. and Singh, T.V.,"On Converging Cylindrical Shock Problem in Radiation Gas Dynamics-Numerical Study", J.of Phys. Society of Japan, Vol.61, 1992, PP.3146-3152.

[29] - Matsuo, H., Ohya, Y., Fujiwara, K.,"Numerical Simulation of Cylindrically Converging Shock Waves",J.of Computational Phys.,1988, Vol. 75, PP. 384-399.

[30] - Srivastova, R.C. et Al. ,"Numerical Investigations of Converging Cylindrical and Spherical Shock Waves", Astrophysics and Space Sci., 1992, Vol. 192, PP. 1-9.

[31] - Itoh, T., Abe, K.,"Simulation of Instability of Cylindrically Converging Shock Waves",4th. Int. Conf. on Appl. Num. Modelling, 1984, Taiwan.

[32] - Kimura, T. Tosa, M,"Fragmentation of a Converging Shock", Mon. Not. R. Astr. Soc., 1990, Vol. 245, PP. 365-369.

[33] - Munz, C.D.,"Two-Step Schemes for the Euler Equations and Numerical Experiments on the Stability of Converging Cylindrical Shock Waves", Proc. 16th Int. Symp. Shock Tubes Waves, 1987 Achen,PP.685-691.

[34] - Demmig, F, Mehmsoth, H.H.,"Model Computation of Converging Cylindrical Shock Waves : Initial Configurations, Propagation, and Reflection", Proc. 17th Int. Symp. Shock Tubes Waves,1989,Bethehem Pa, PP. 155-160.

[35] - Demmig, F, et al. . "Experiments and model Computation of Cylindrical Shock Waves With Time-resolved deformation and Fragmentation", Proc. 19th Int. Symp. Shock Tube Waves, July 1993, France.

[36] - Korobeinikov, V.P.,"Unsteady Interaction of Shock and Detonation Wave in Gases", 1989, Hemisphere Publishing Corp. English editor: Urtiew, P.A.

[37] - Warming, R.F., Kutler, P., Lomax, H.,"Second- and Third-order Noncentered Difference Schemes for Non-linear Hyperbolic Equations", Vol. 11, No. 2, AIAA J., 1973.

[38] - MacCarmack, R.W.,"The Effect of Viscosity in Hypervelocity Impact", AIAA paper No. 69-354, 1969.

[39] - MacCarmack, R.W.,"Numerical Solution of the Interaction of a Shock Wave with a Laminar Boundary Layer", Lecture notes in Physics, Vol. 8, Springer-Verlag, N.Y.,1971,pp.151-163.

[40]- MacCarmack, R.W., Paullay, A.J.,"Computational efficiency achieved by time splitting of finite difference operators", AIAA paper No. 72-154, 1972.

[41]- Baldwin, B.S., MacCarmack, R.W.,"Interaction of Strong Wave with Turbolant Boundary Layer", Lecture notes in Physics, Vol. 35, Springer-Verlag, Heidelberg, 1975, pp. 51-56.

[42] - Pai, S., Luo, S.,"Theoretical and Computational Dynamics of a Compressible Flow", Van Nostrand Reinhold, N.Y., 1991.

[43] - Saad, M.A.,"Compressible Fluid Flow", Prentice-Hall Inc., 2nd Ed., 1993.

[44]- Zitouni, G.,"Theoretical and Experimental Investigation of Converging Shock Waves Propagating in Narrow Cylindrical Chambers", M.A.Sc. Thesis, Concordia University, Nov. 1992.

[45]- Wanatabe, M.,"Experimental and numerical study of converging cylindrical shock waves", Proc. 18th Int. Symp. Shock Waves, Japan, Jul. 1991.

[46]- Tashtoush, B.,"The effect of Non Uniform Bleed and Cylindrical Chamber Width's on Converging Shock Wave Stability", Ph.D. Thesis, Concordia University, (To be presented on Oct. 1994).

[47]- Neemeh, R.A., Tashtoush, B., Vatistas, G.H.,"The Relationship Between the Size of the Perturbation and the Vortex Pair Structure for Converging Cylindrical Shocks", Proc. 19th Int. Symp. on Shock Waves, France, July 1993.

[48]- Wu, J. H. T., Neemeh, R.A., Ostrowski, P.P.,"Experiments on the Stability of Converging Cylindrical Shock Waves", AIAA J., Vol. 19, No. 3, Mar. 1981.

r=0   r=1

1 2   i−1 i i+1   n
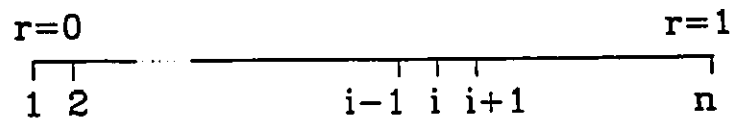
Figure (2.1)- Mesh for the 1D problem
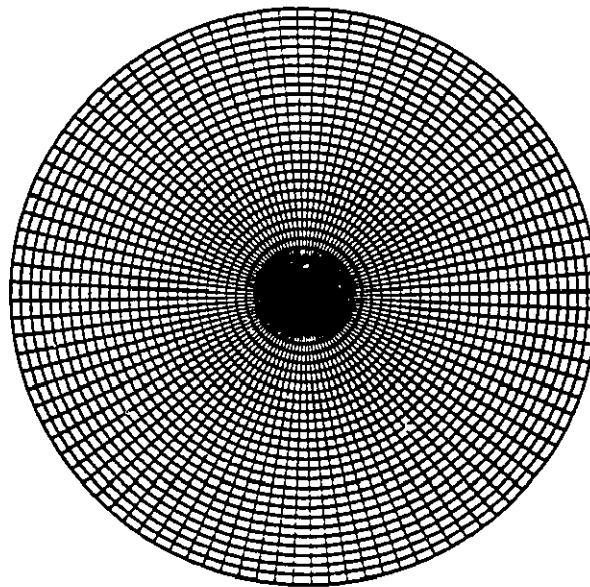
Figure (2.2)- Mesh for the 2D problem

61
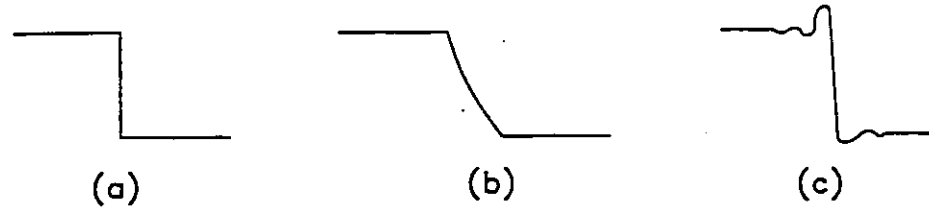
a— Exact
b— Dissipation
c— Dispersion

Figure (2.3)- Effect of the different types of errors on representing a discontinuity
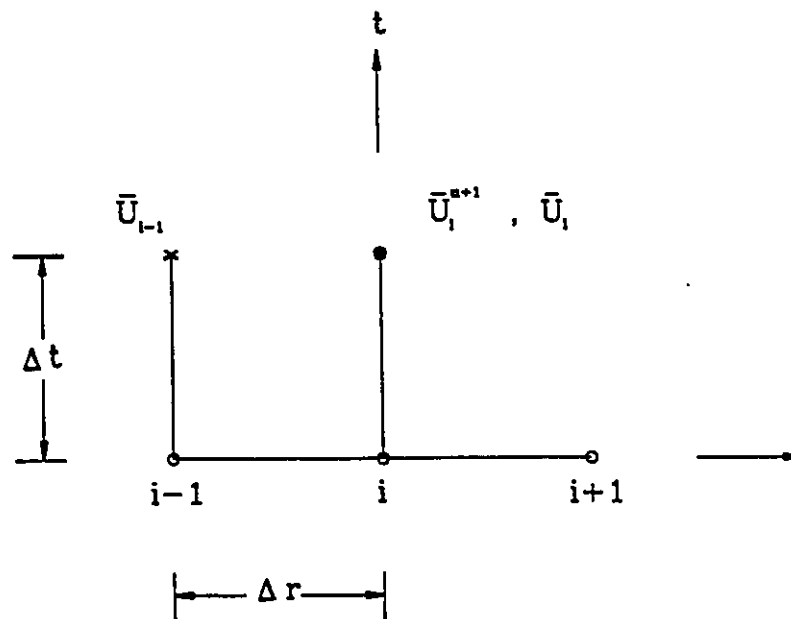
Figure (2.4)- Schematic of the space-time index
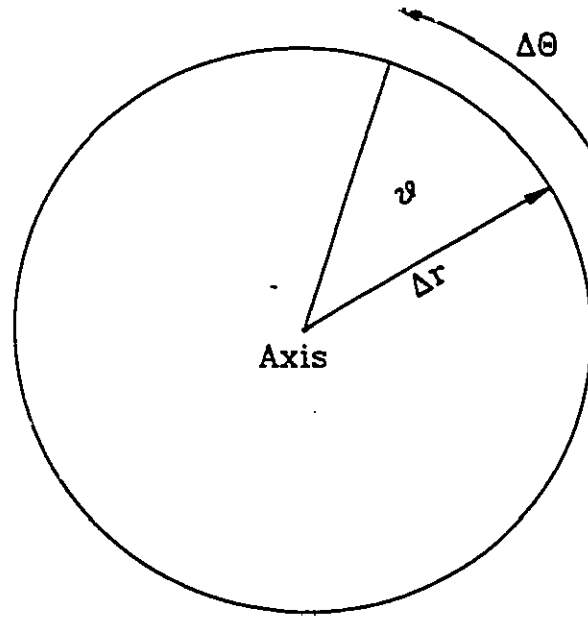
Figure (2.5)- Control volume near the axis
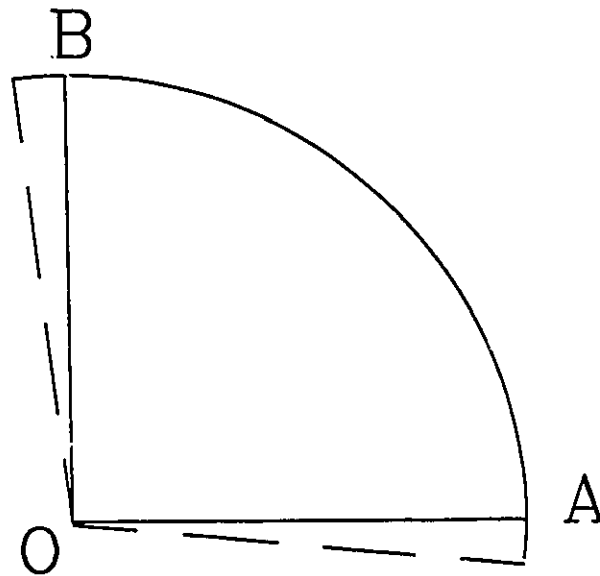
Figure (2.6)- Schematic for the computation domain

Diaphragm

$V_2 = 0$
$T = T_1$
$P = KP_1$
$\rho_2 = K\rho_1$

$V_1 = 0$
$P = P_1$
$T = T_1$
$\rho = \rho_1$
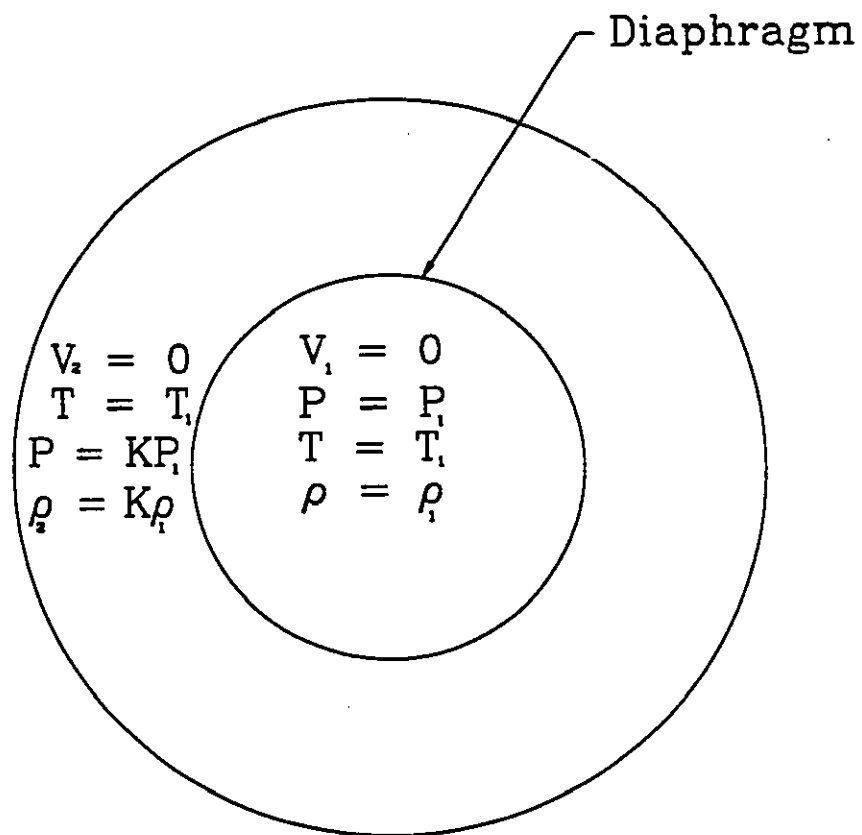
Figure (3.1)- Schematic of the model for 1D and 2D simulations
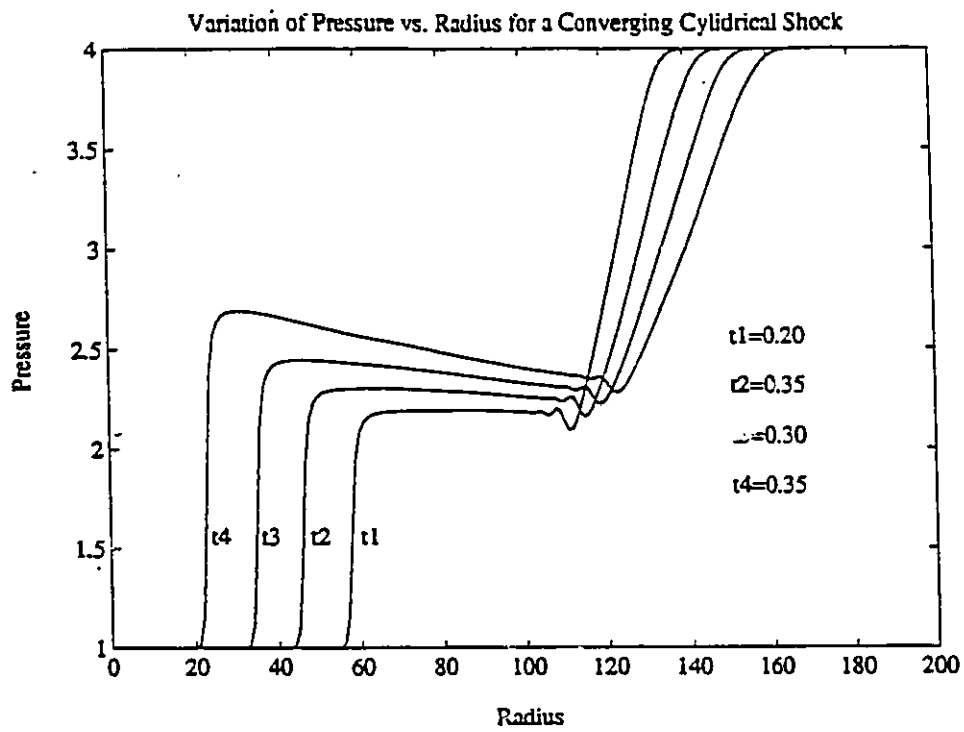
Figure (3.2a)- Variation of pressure vs. radius (K=4)
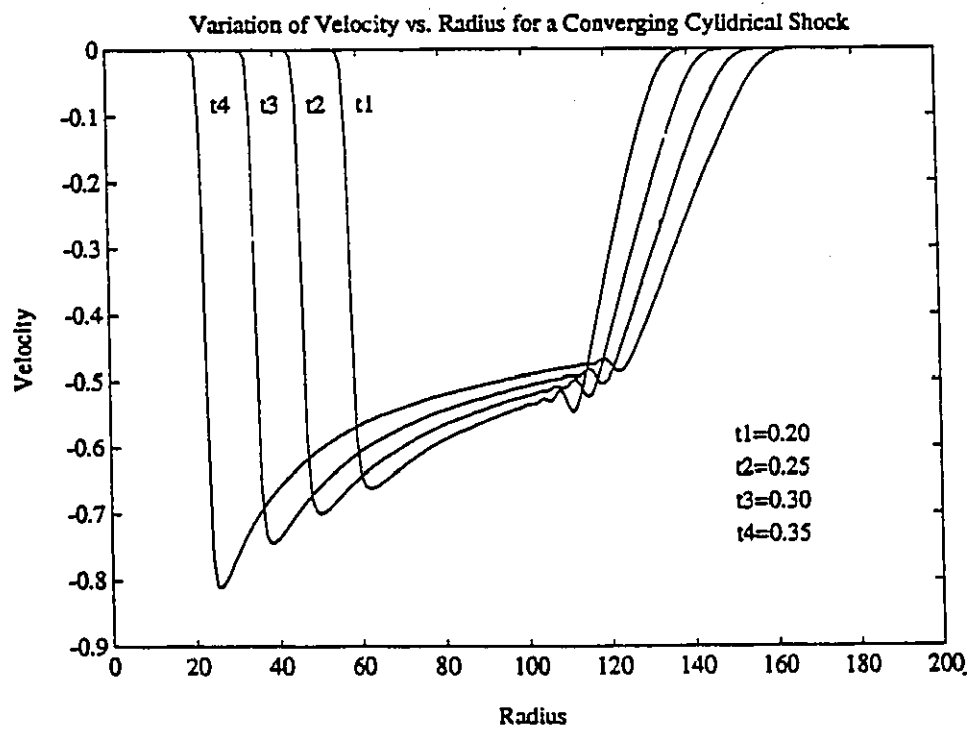
Figure (3.2b)- Variation of velocity vs. radius (K=4)

Variation of Density vs. Radius for a Converging Cylidrical Shock
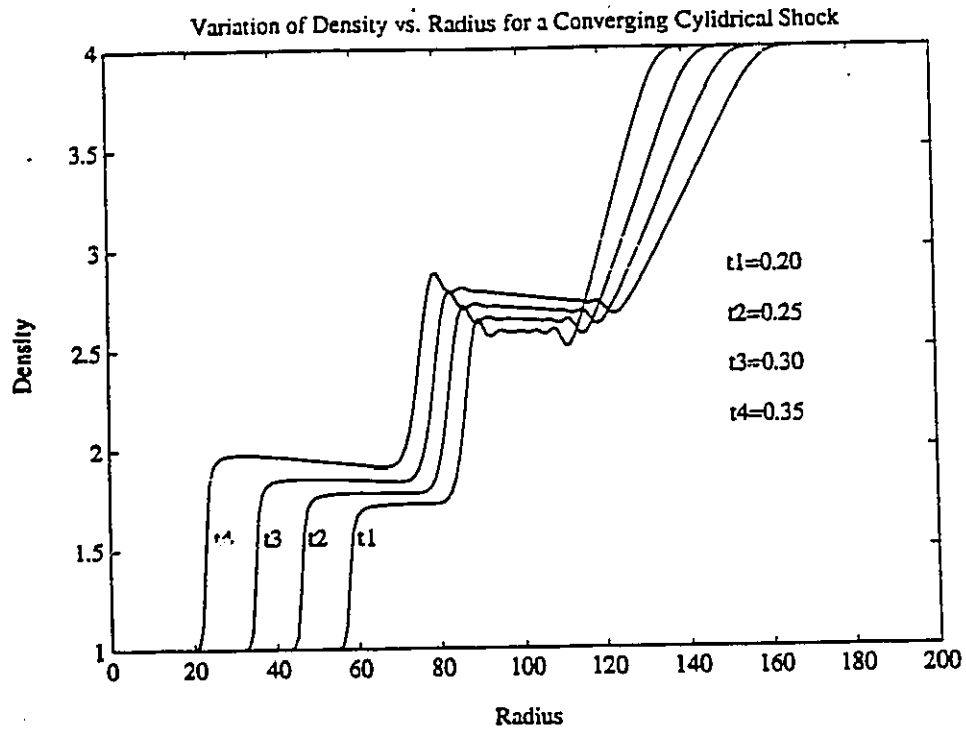
Figure (3.2c)- Variation of density vs. radius (K=4)

Variation of Temperature vs. Radius for a Converging Cylidrical Shock
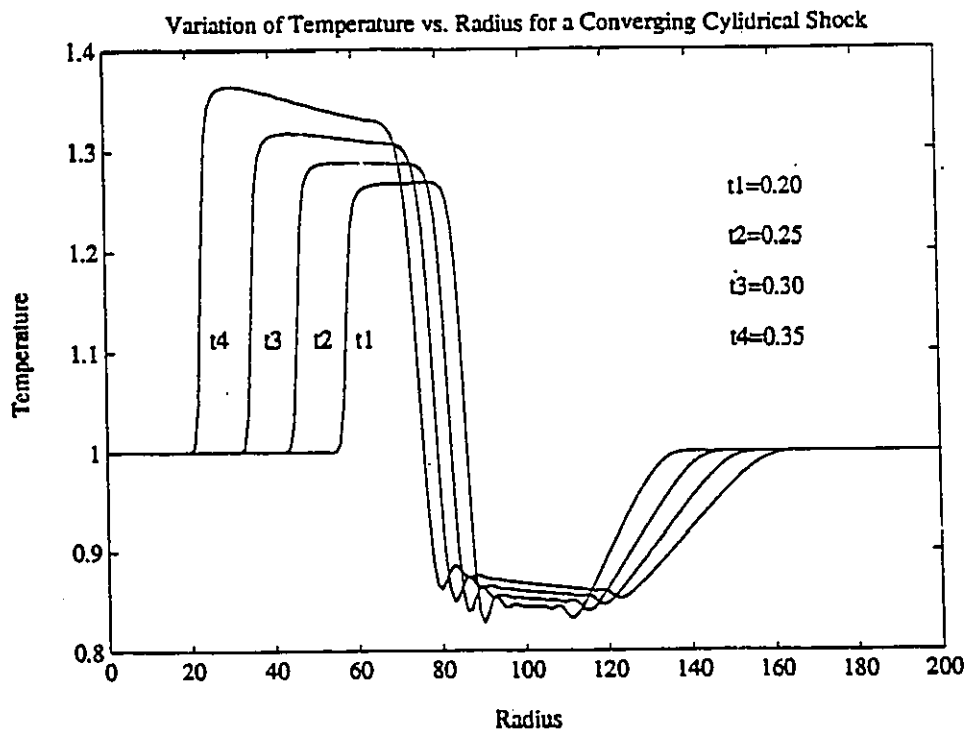
Figure (3.2d) Variation of temperature vs. radius (K= 4)
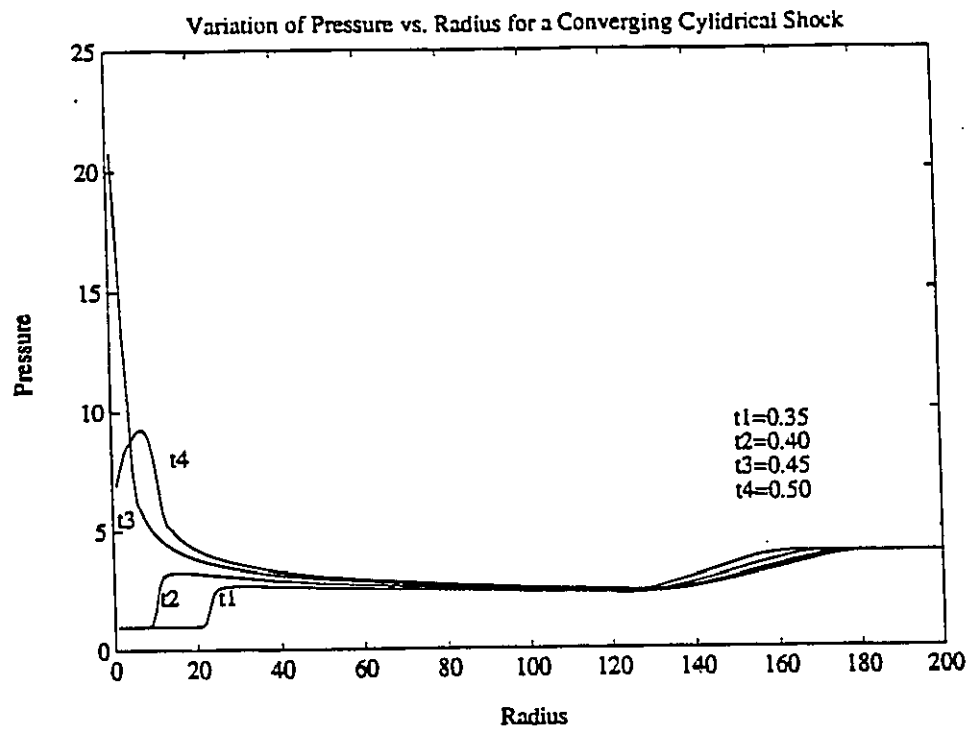
Figure (3.2e)- Variation of pressure vs. radius (K=4)
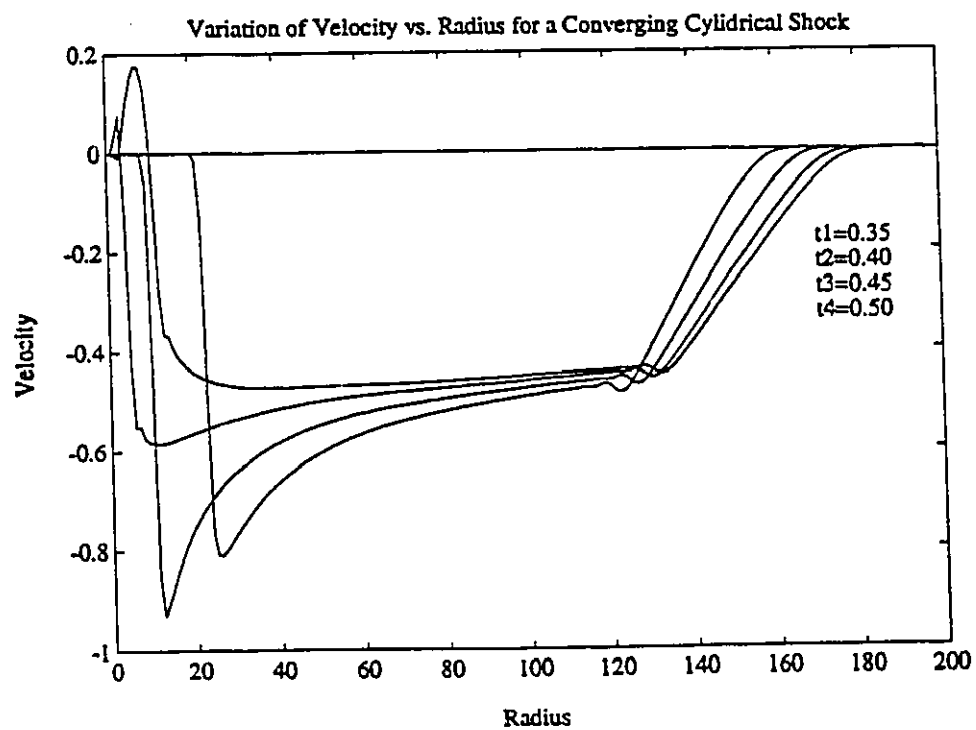
Figure (3.2f)- Variation of velocity vs. radius (K=4)

Variation of Density vs. Radius for a Converging Cylidrical Shock

t1=0.35
t2=0.40
t3=0.45
t4=0.50
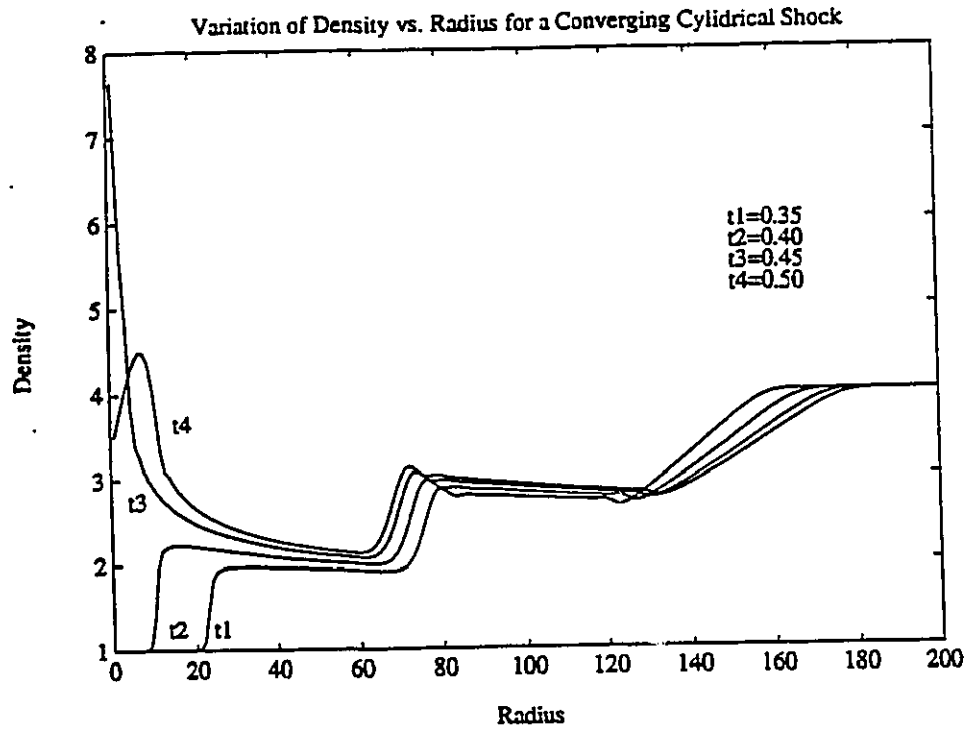
Density

Radius

Figure (3.2g)- Variation of density vs. radius (K=4)

Variation of Temperature vs. Radius for a Converging Cylidrical Shock

t1=0.35

t2=0.40

t3=0.45

t4=0.50

Temperature
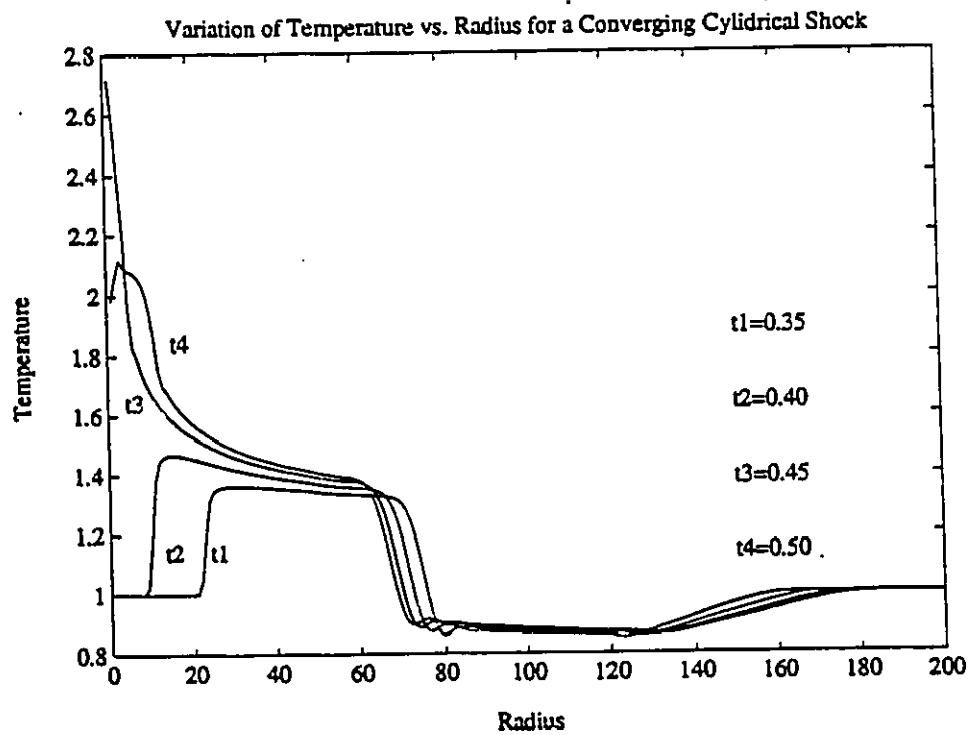
Radius

Figure (3.2h)- Variation of temperature vs. radius (K=4)

68
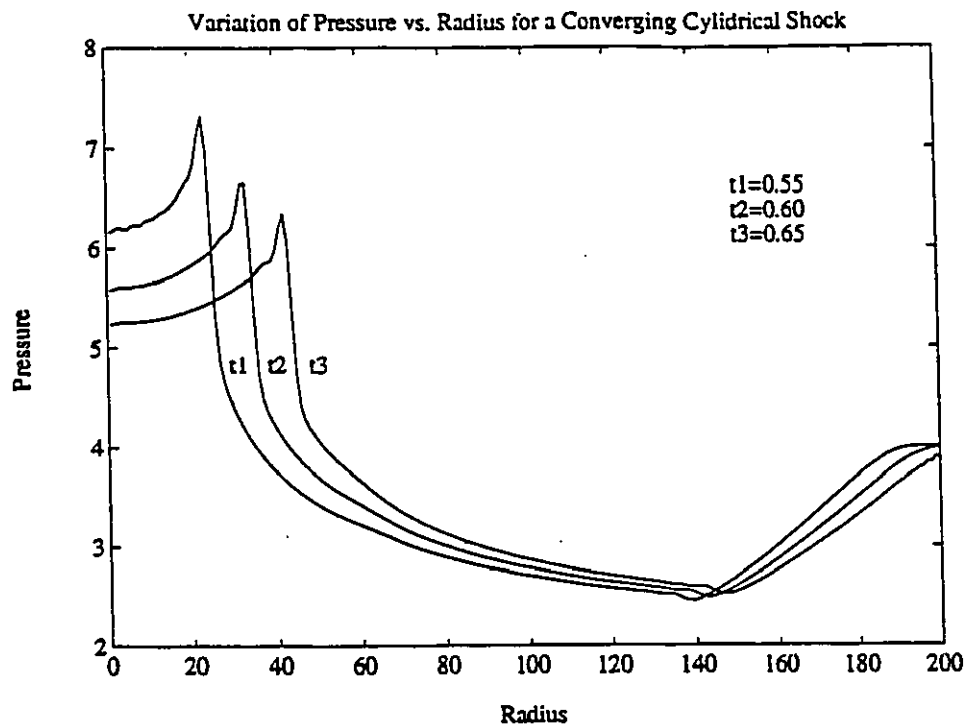
Figure (3.2i)- Variation of pressure vs. radius (K=4)
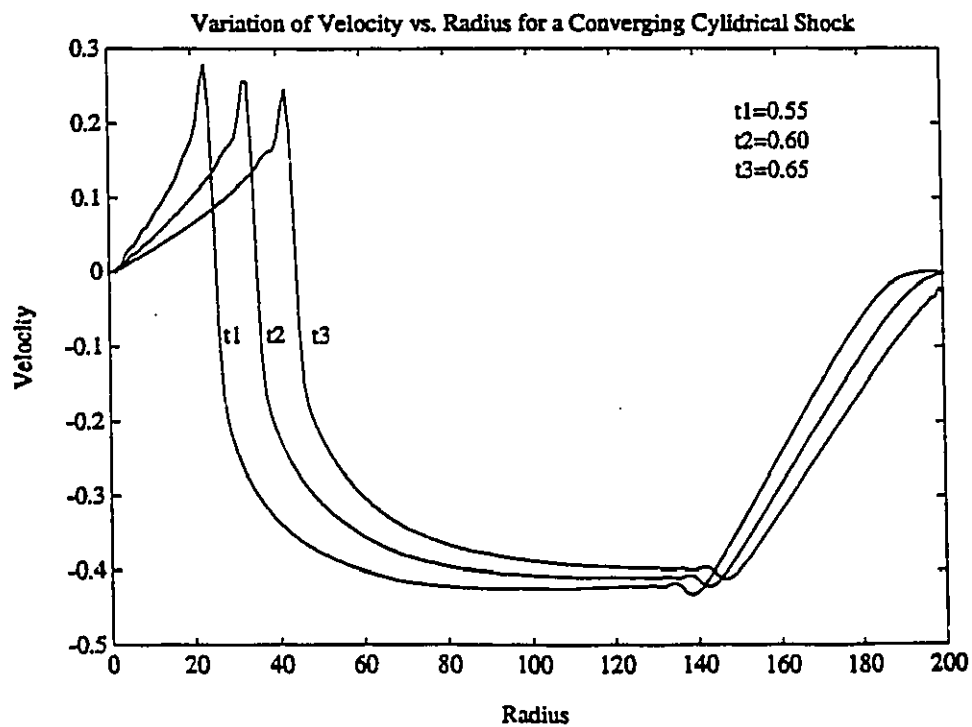
Figure (3.2j)- Variation of velocity vs. radius (K=4)

69

Variation of Density vs. Radius for a Converging Cylidrical Shock

t1=0.55
t2=0.60
t3=0.65
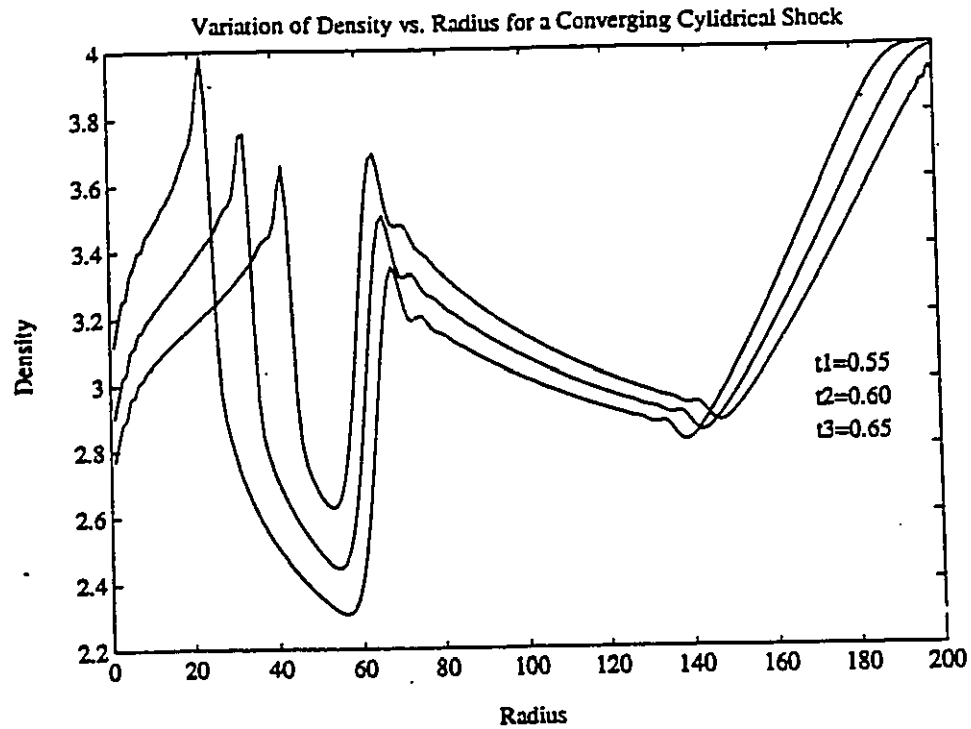
Density

Radius

Figure (3.2k)- Variation of density vs. radius (K=4)

Variation of Temperature vs. Radius for a Converging Cylidrical Shock

t1=0.55
t2=0.60
t3=0.65

t1 t2 t3

Temperature
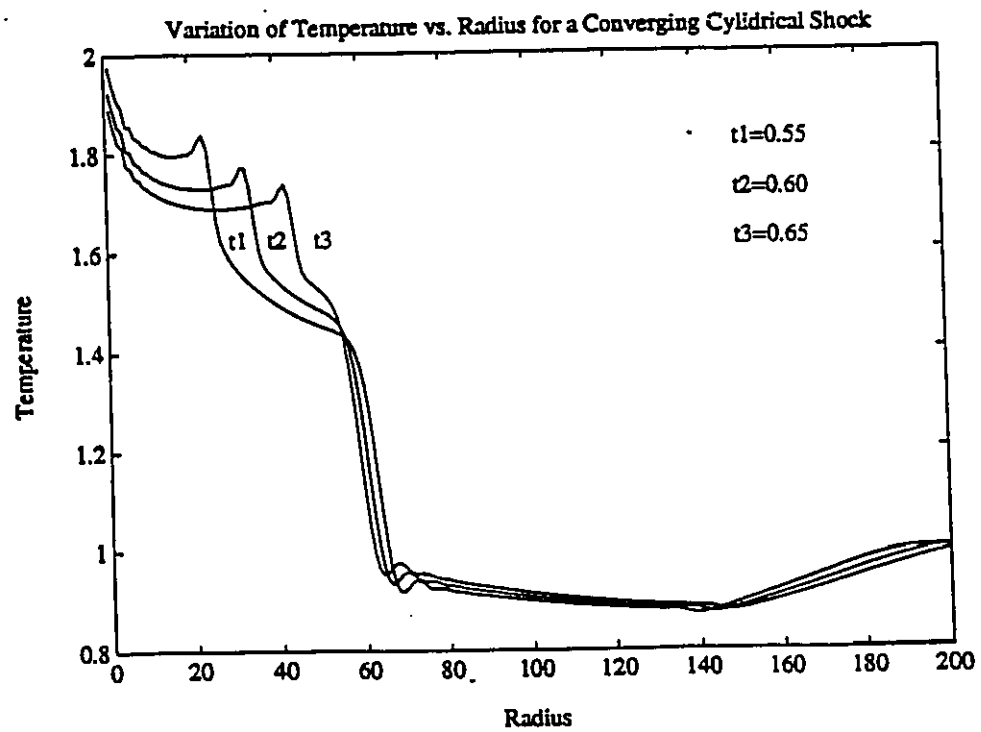
Radius

Figure (3.2l)- Variation of temperature vs. radius (K=4)

70
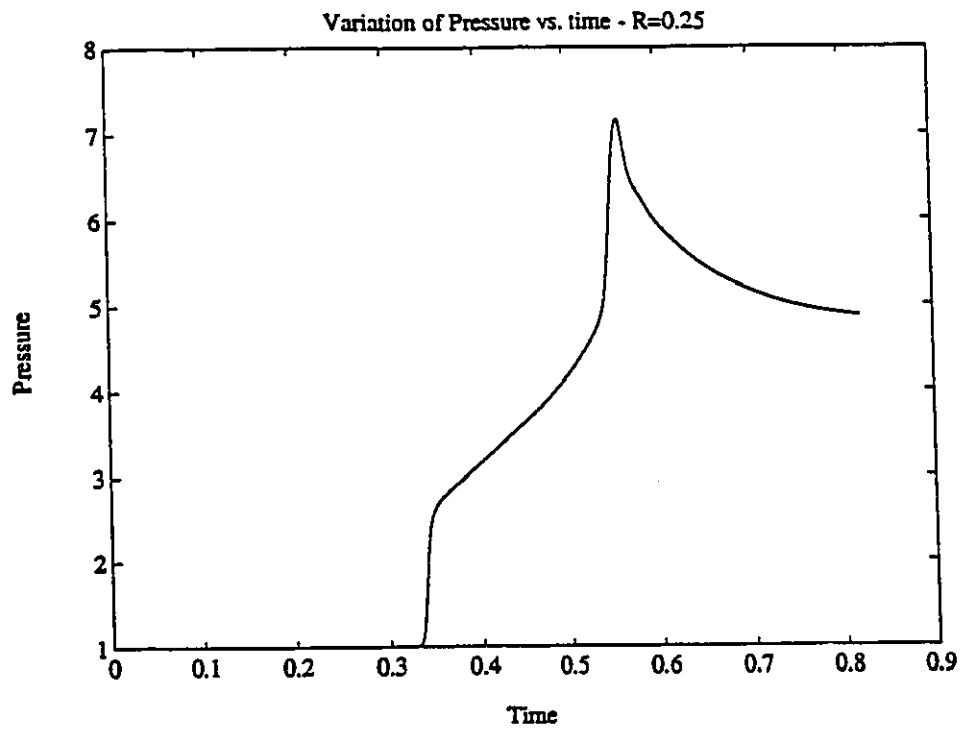
Figure (3.3a)- Variation of pressure vs. time at constant radius (K=4)
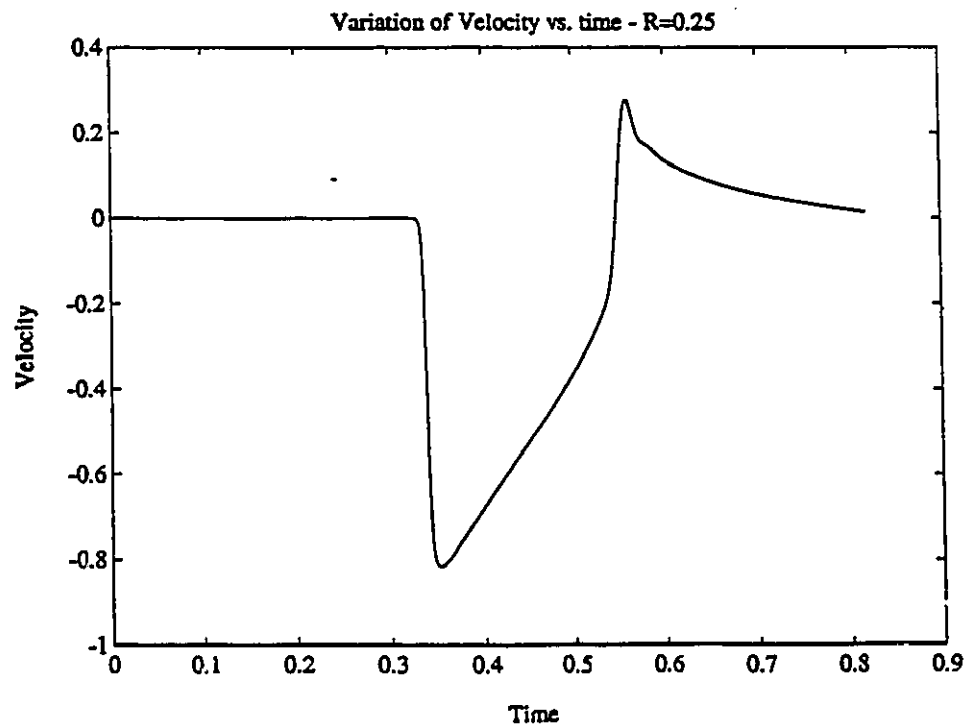
Figure (3.3b)- Variation of velocity vs. time at constant radius (K=4)

71
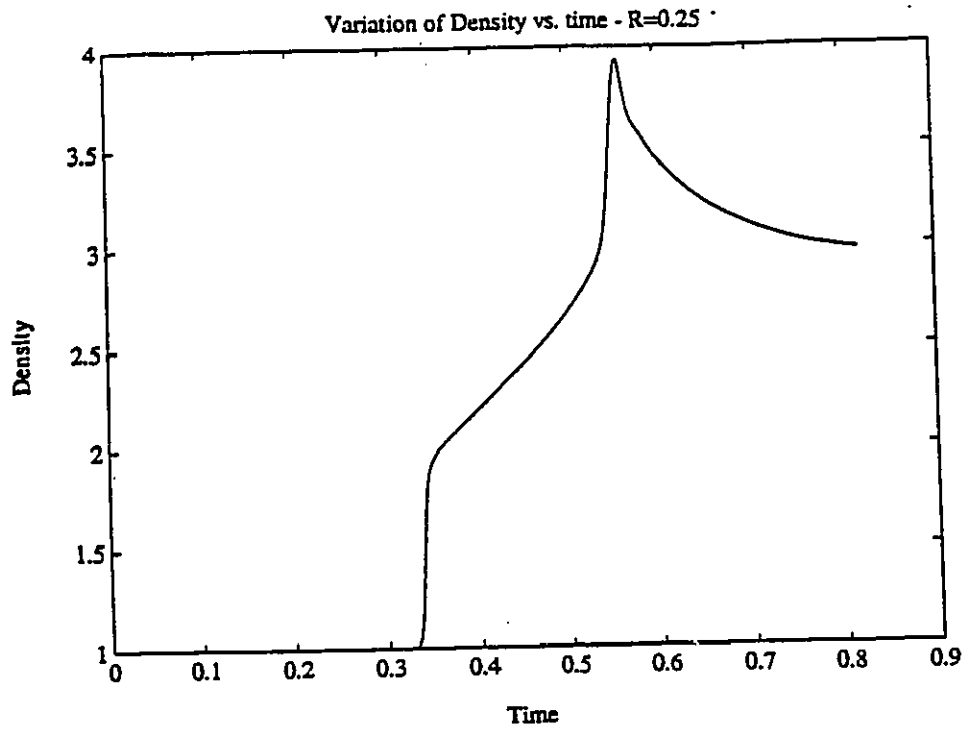
Figure (3.3c)- Variation of density vs. time at constant radius (K=4)
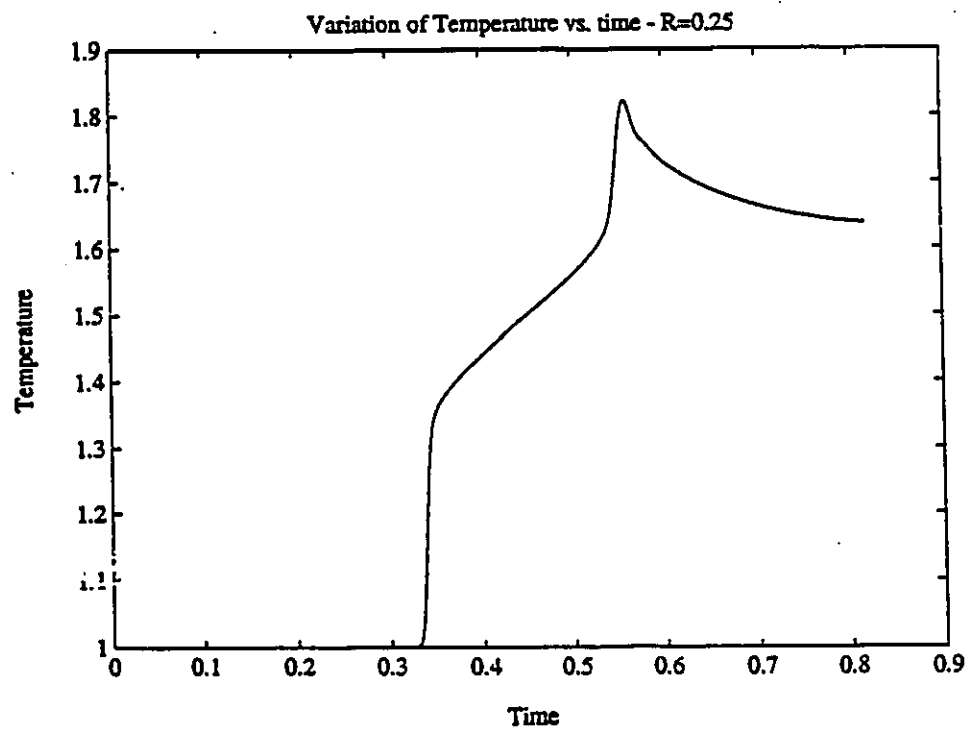
Figure (3.3d)- Variation of temperature vs. time at constant radius (K=4)

72
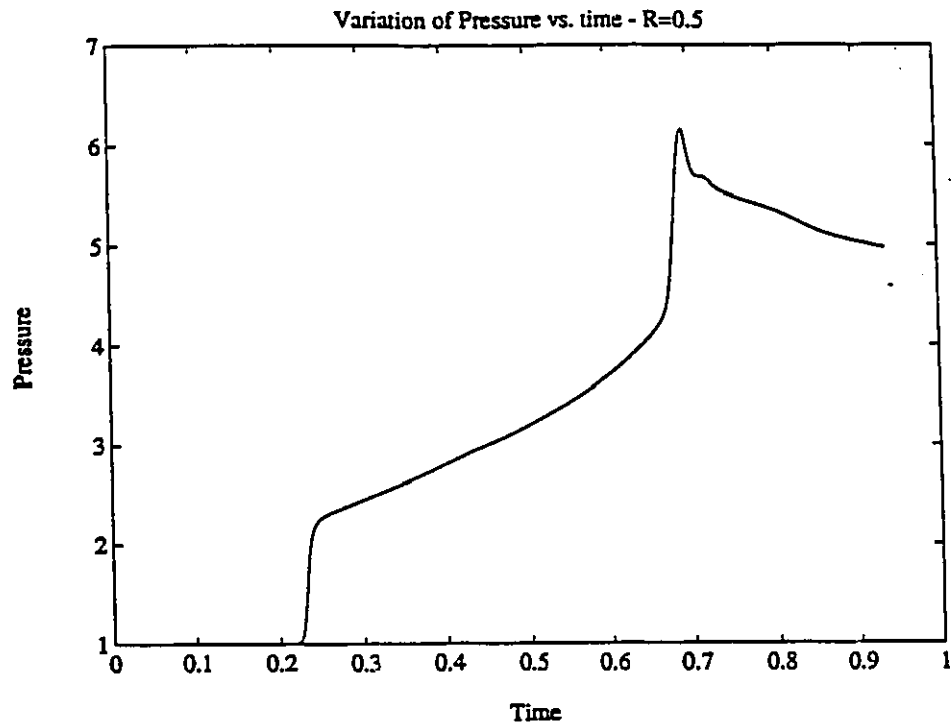
Figure (3.3e)- Variation of pressure vs. time at constant radius (K=4)
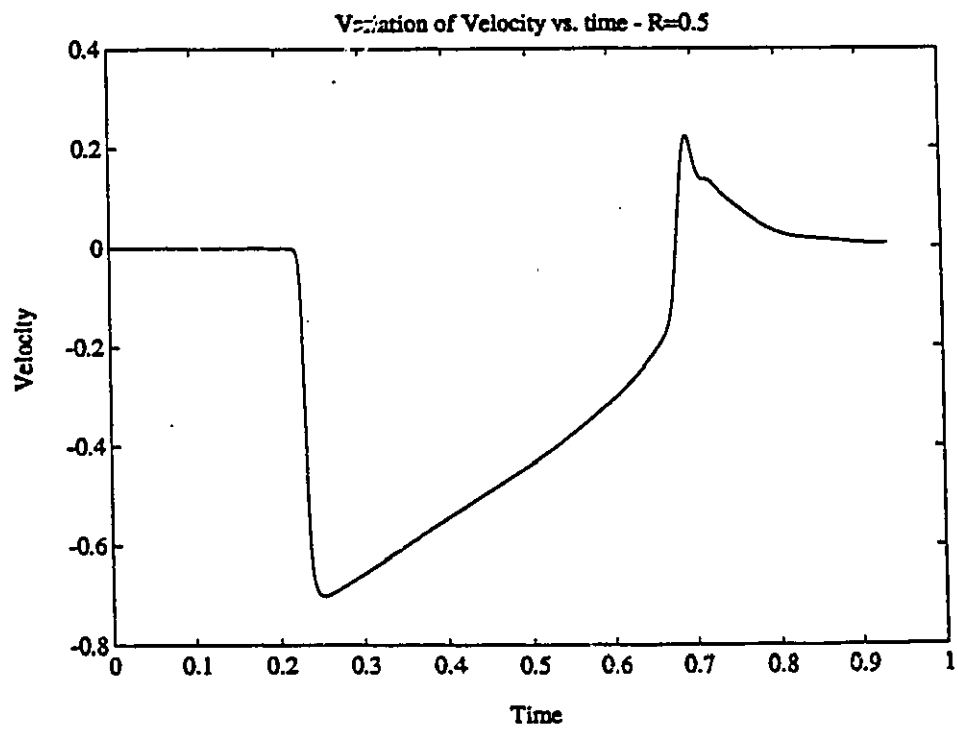
Figure (3.3f)- Variation of velocity vs. time at constant radius (K=4)
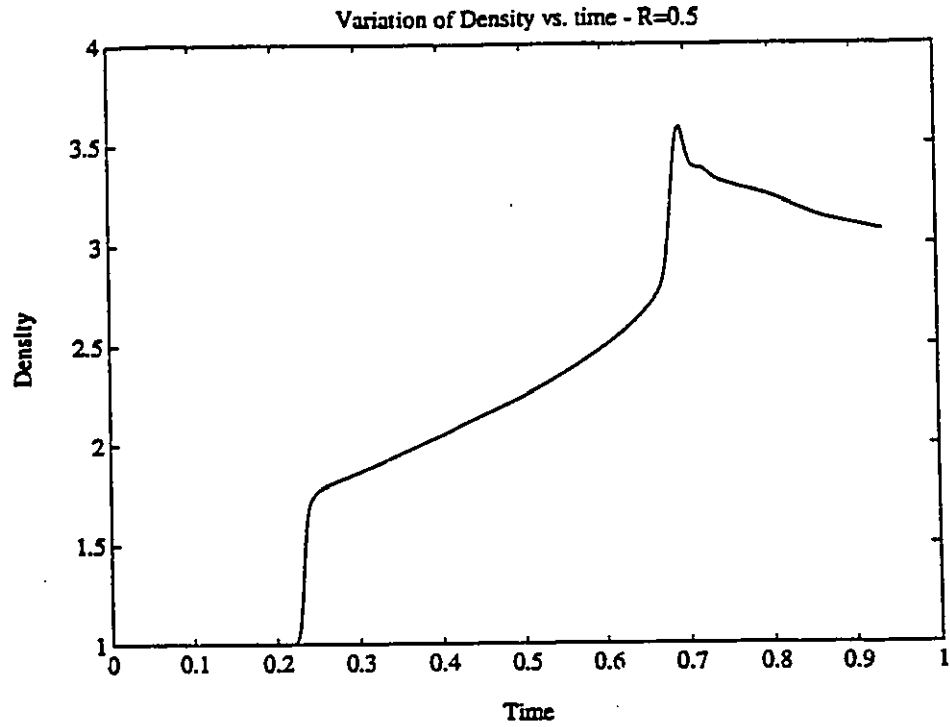
Figure (3.3g)- Variation of density vs. time at constant radius (K=4)
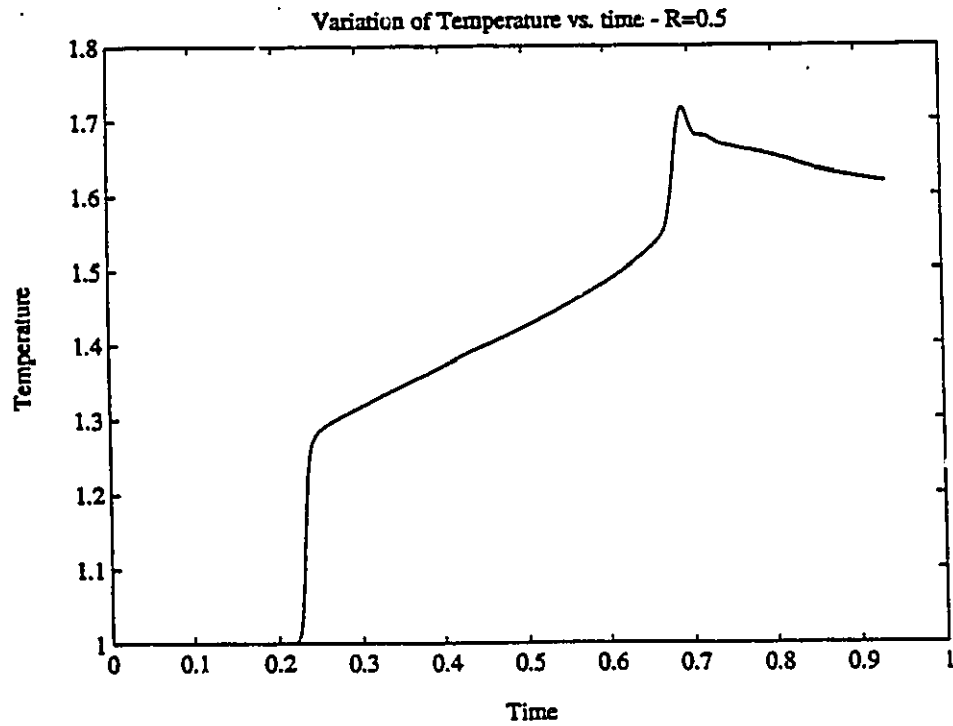
Figure (3.3h)- Variation of temperature vs. time at constant radius (K=4)

74
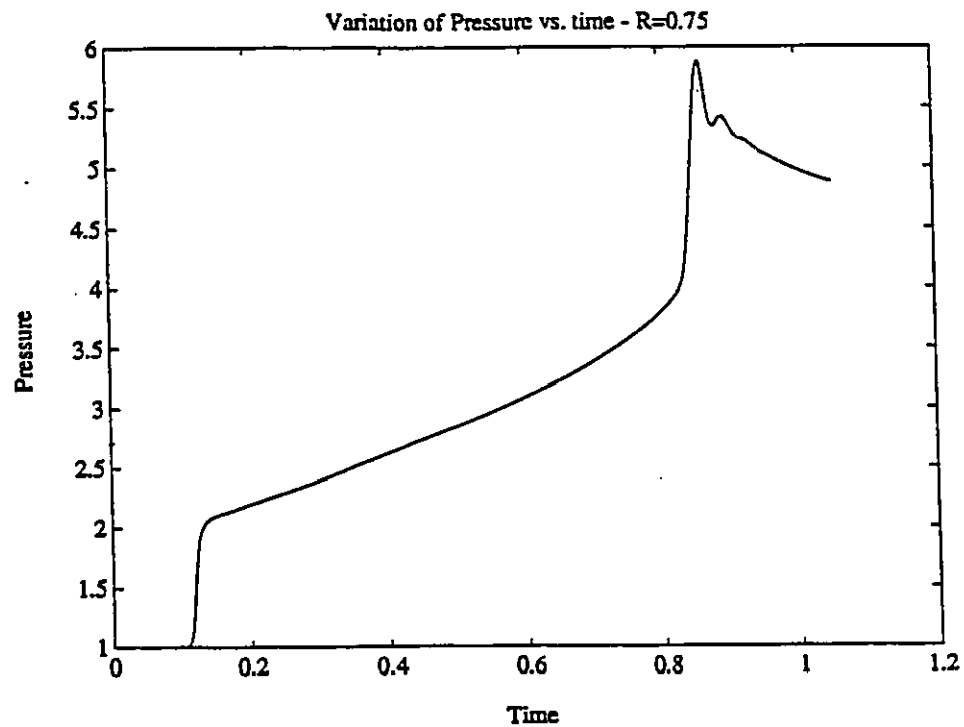
Figure (3.3i)- Variation of pressure vs. time at constant radius (K=4)
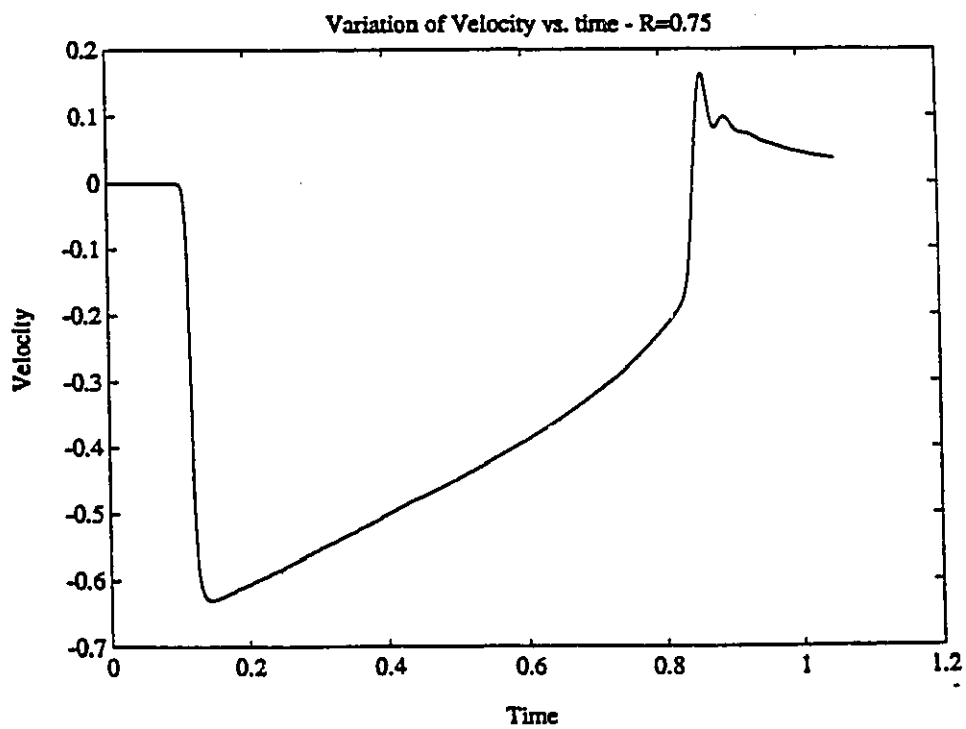
Figure (3.3j)- Variation of velocity vs. time at constant radius (K=4)

75
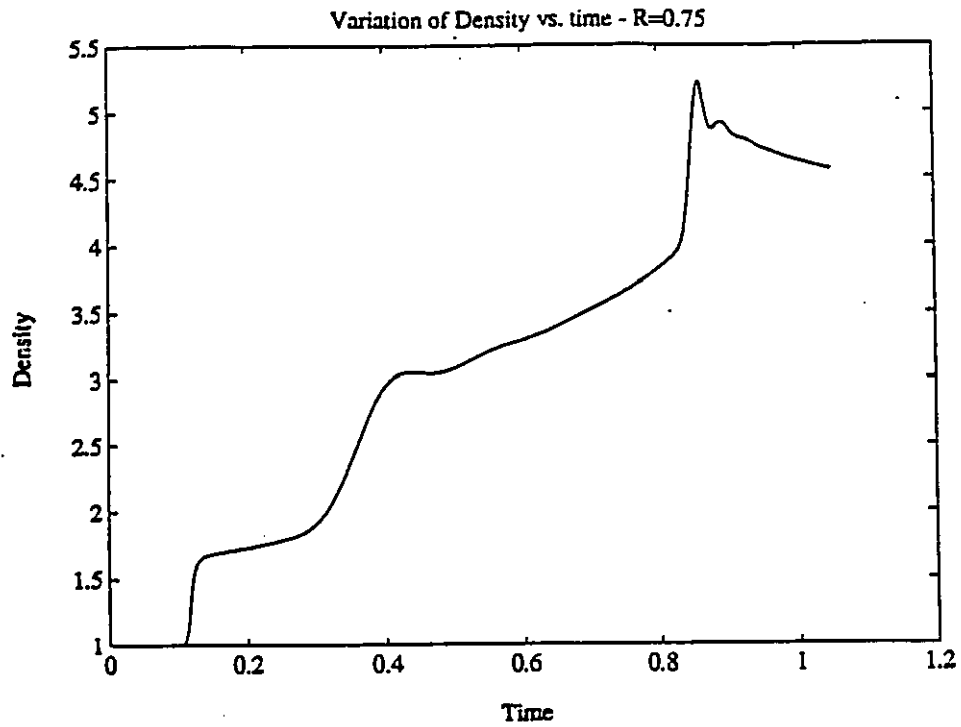
Figure (3.3k)- Variation of density vs. time at constant radius (K=4)
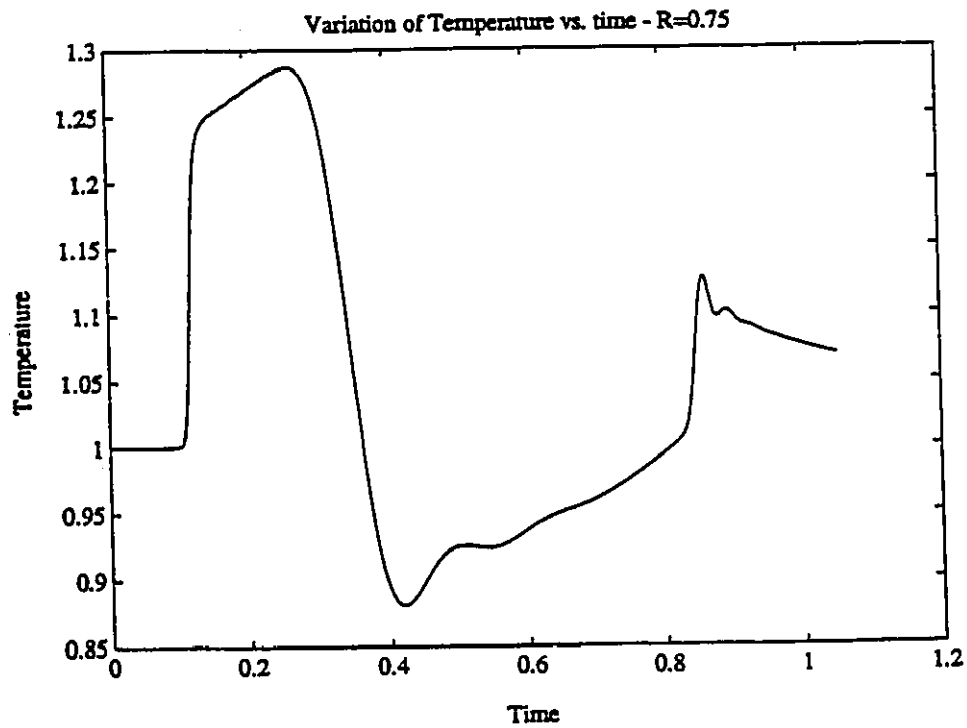
Figure (3.3l)- Variation of temperature vs. time at constant radius (K=4)

76
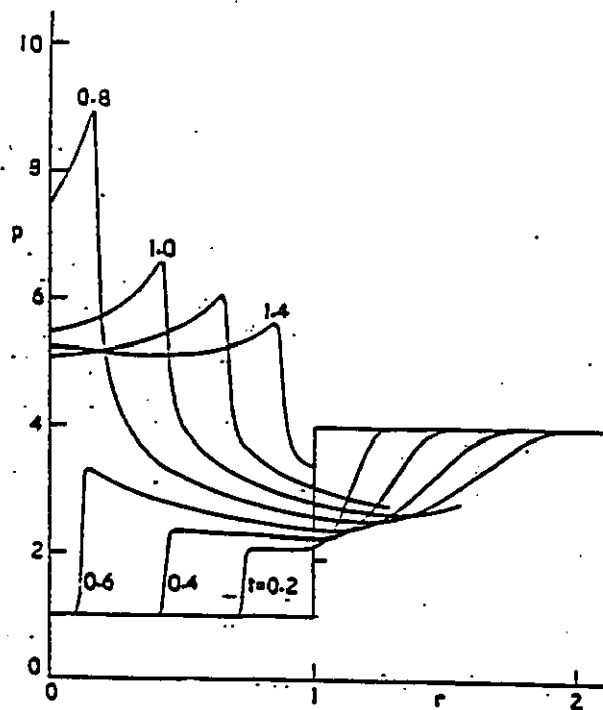
Figure (3.4a)- Pressure variation vs. radius (Payne [21])
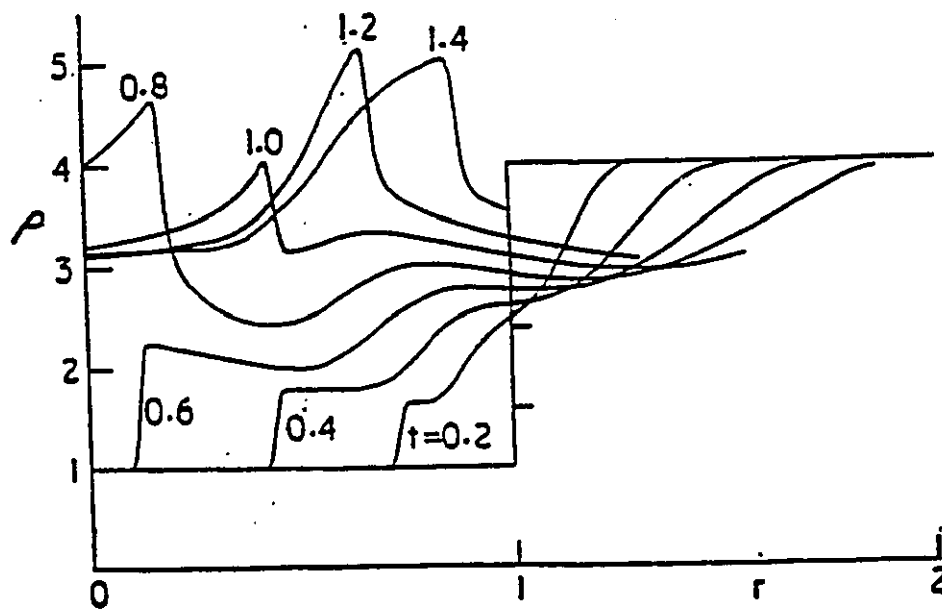
Figure (3.4b)- Density variation vs. radius (Payne [21])
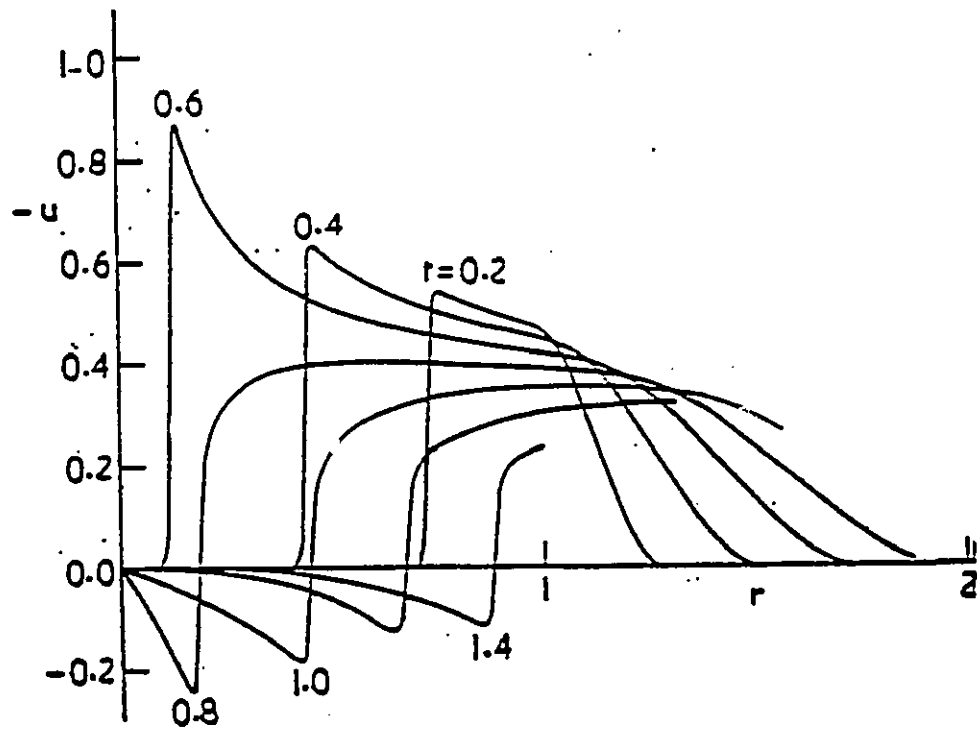
Figure (3.4c)- Velocity variation vs. radius (Payne [21])
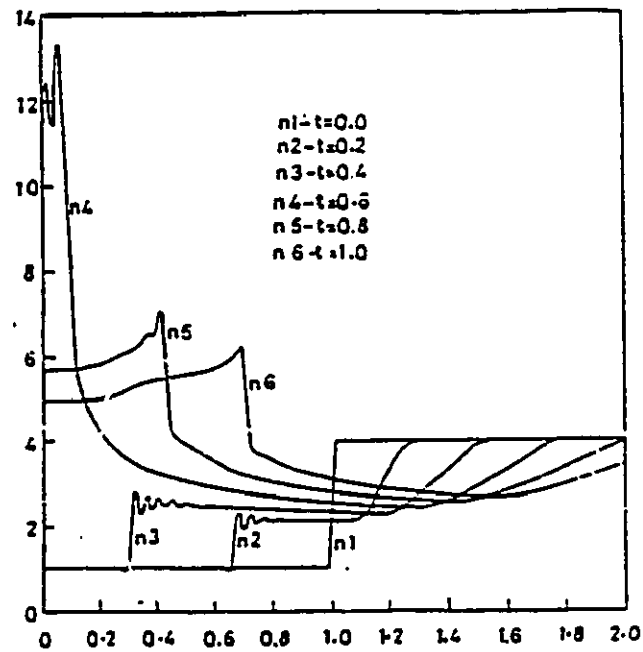
Figure (3.4d)- Pressure variation vs. radius (Shankar et al. [28])
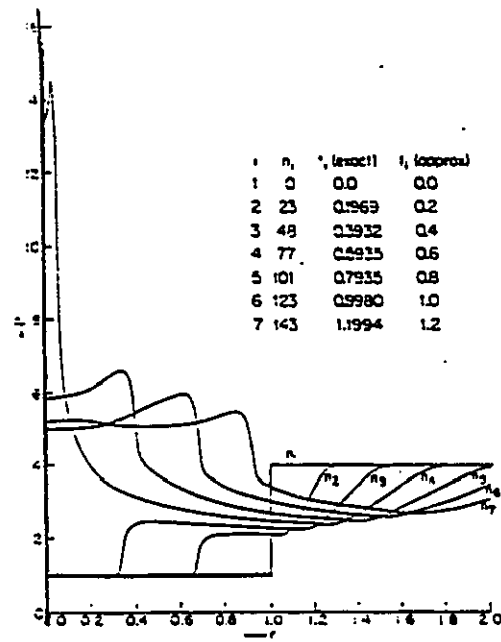
Figure (3.4e)- Pressure variation vs. radius (Abrabanel et al. [23])
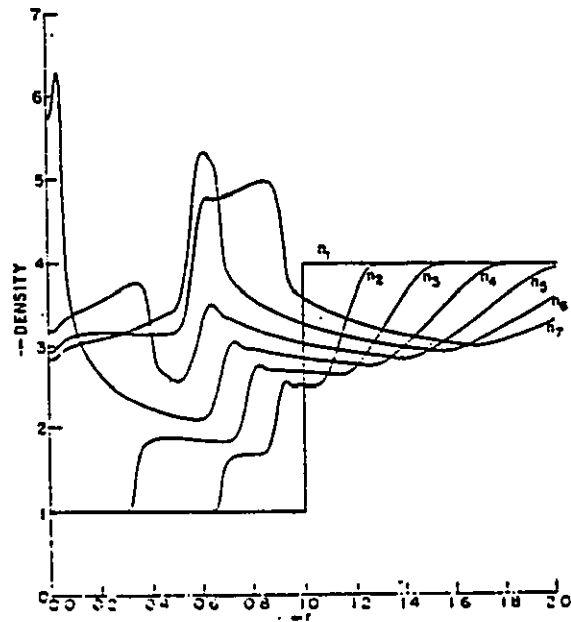
Figure (3.4f)- Density variation vs. radius (Abrabanel et al. [23])
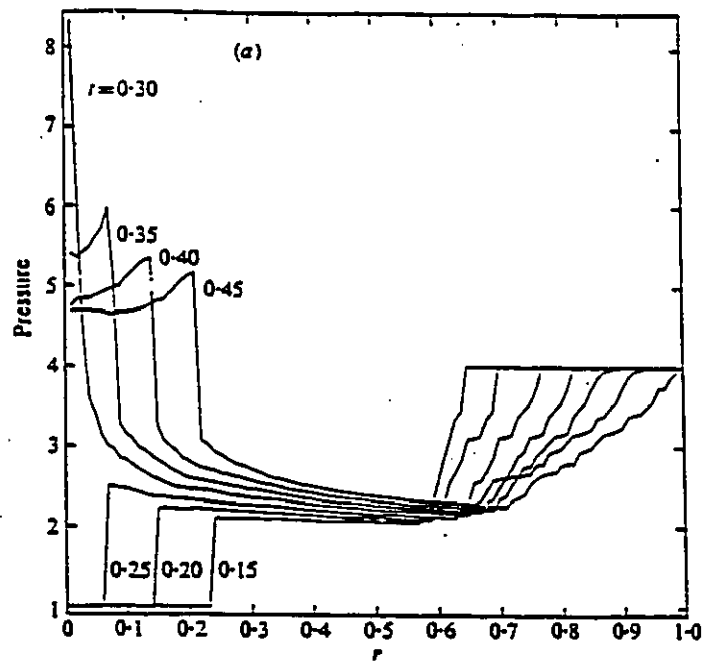
Figure (3.4g)- Pressure variation vs. radius (Sod [24])
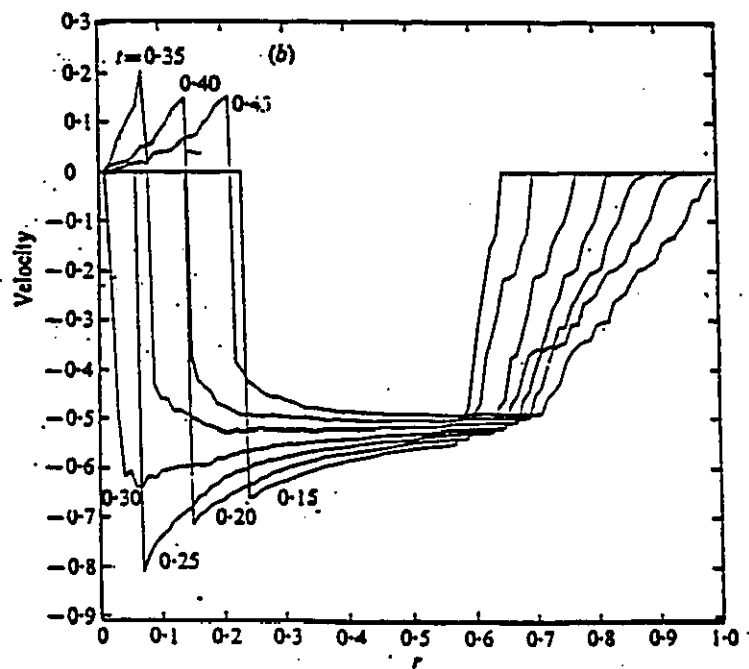
Figure (3.4h)- Velocity variation vs. radius (Sod [24])

80
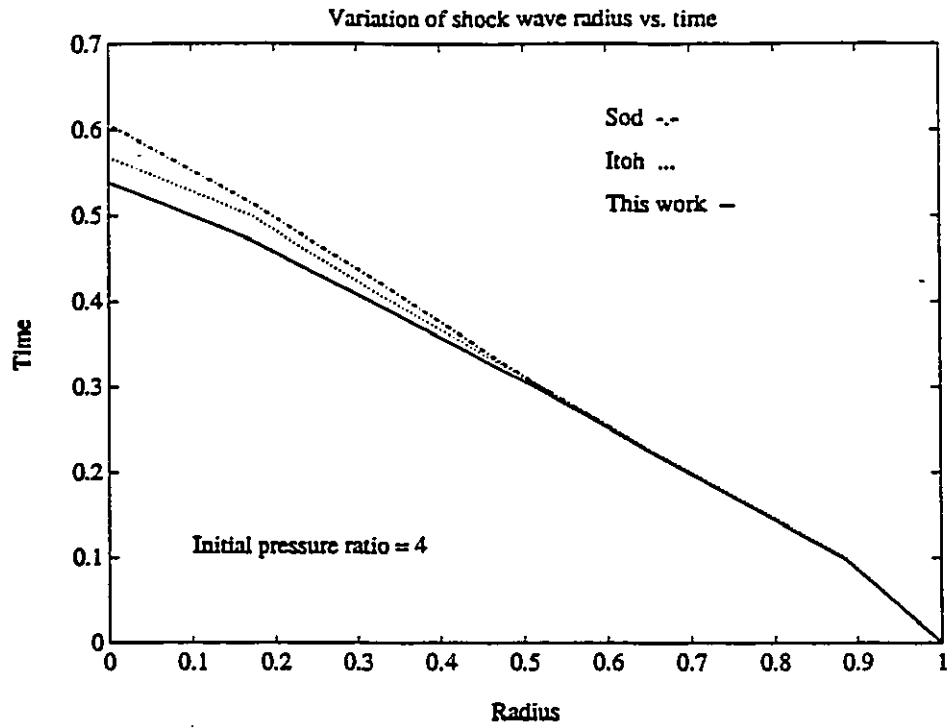
Figure (3.5)- Variation of shock wave's radius vs. time
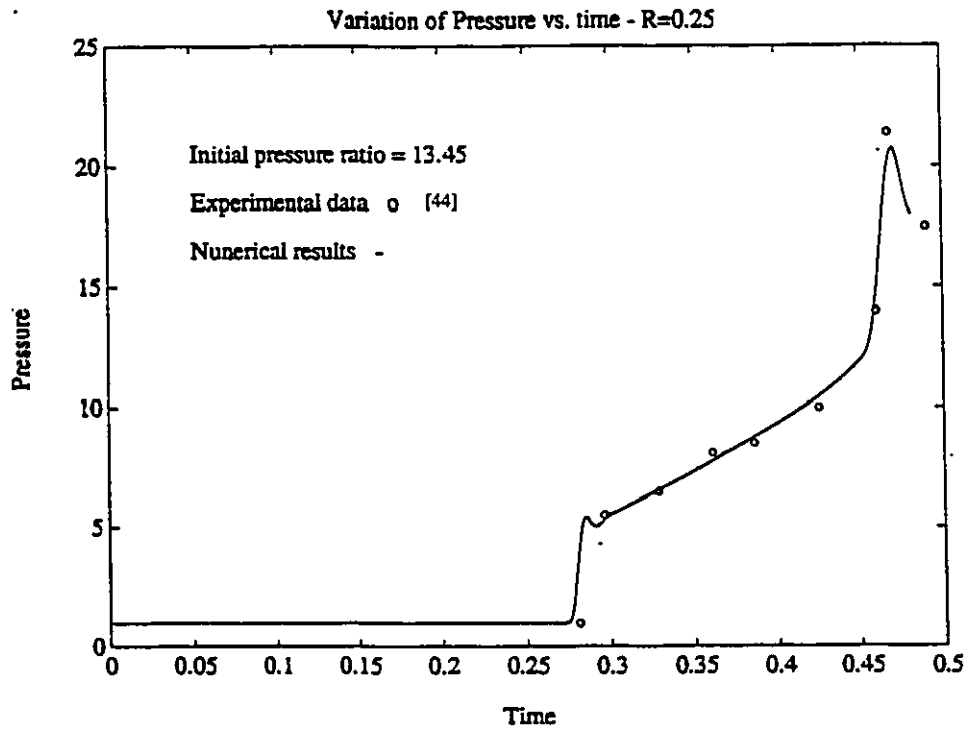
Figure (3.6a)- Variation of pressure vs. time at constant radius

81
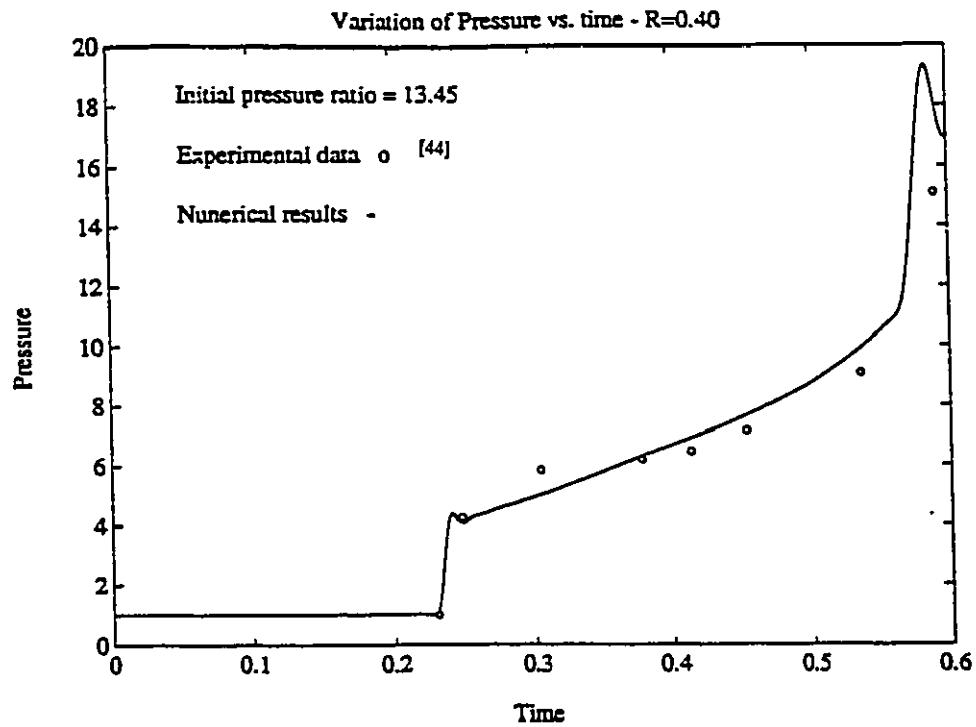
Figure (3.6b)- Variation of pressure vs. time at constant radius
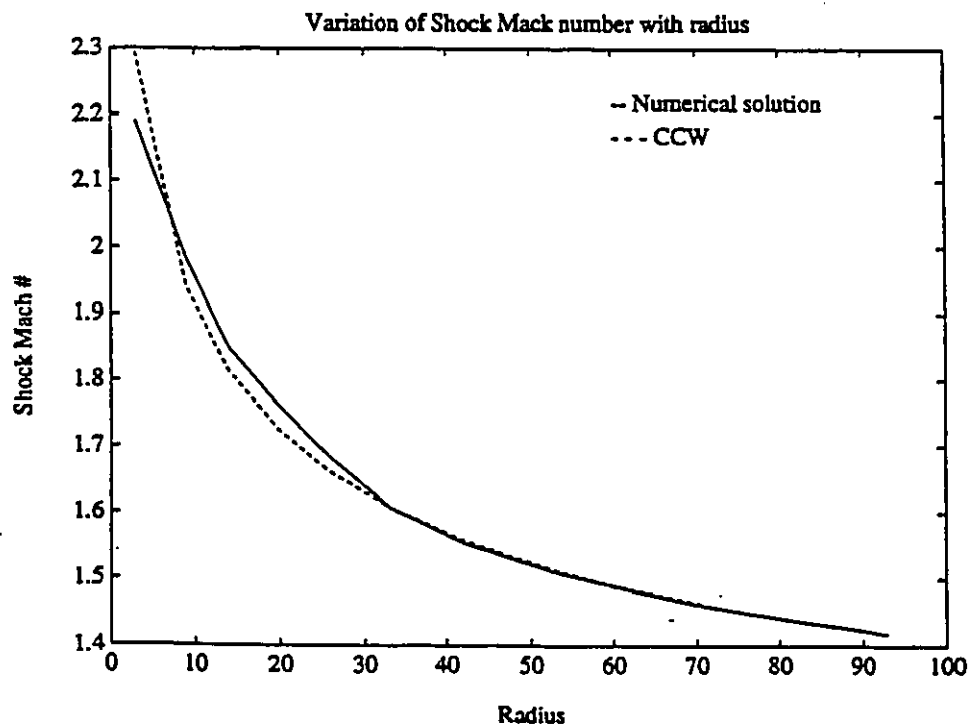
Figure (3.7)- Variation of shock Mack number vs. radius

82
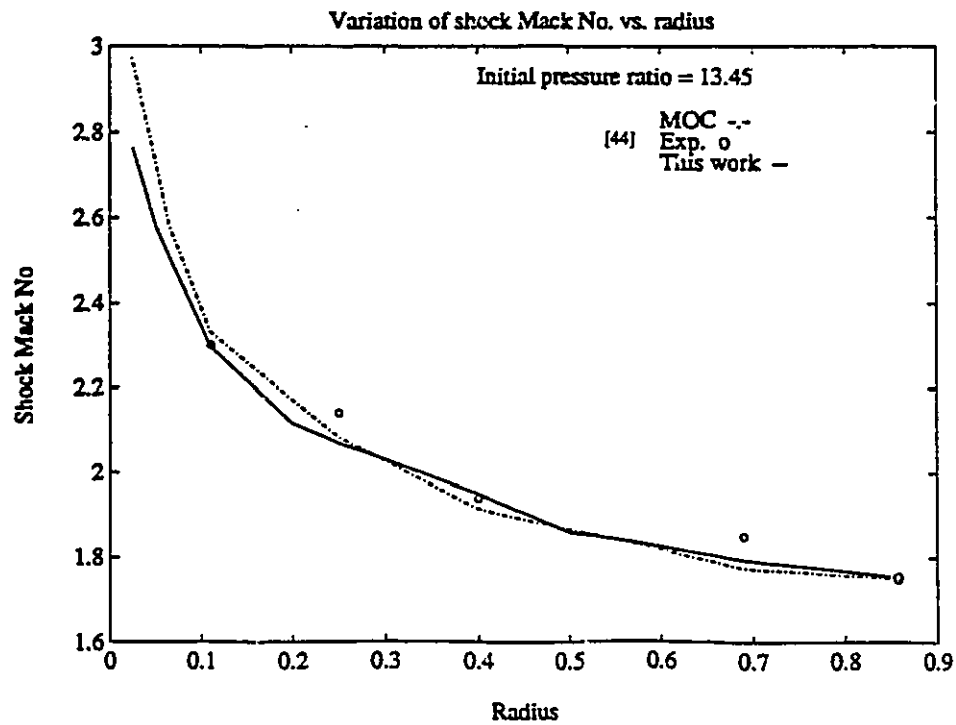
Figure (3.8a)- Variation of shock Mack number vs. radius
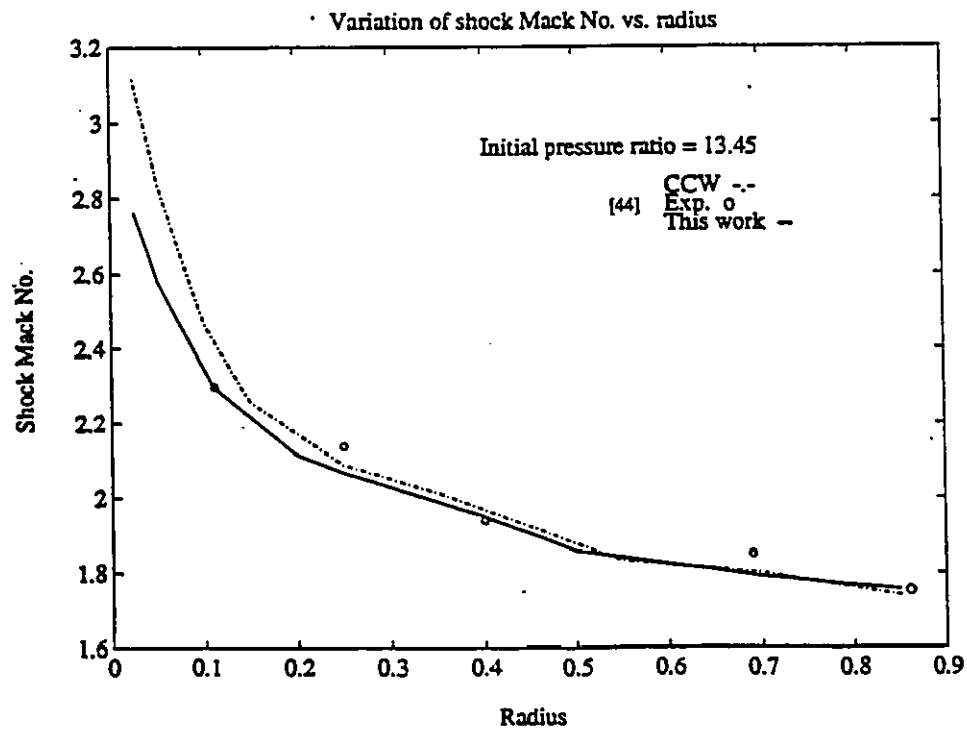
Figure (3.8b)- Variation of shock Mack number vs. radius
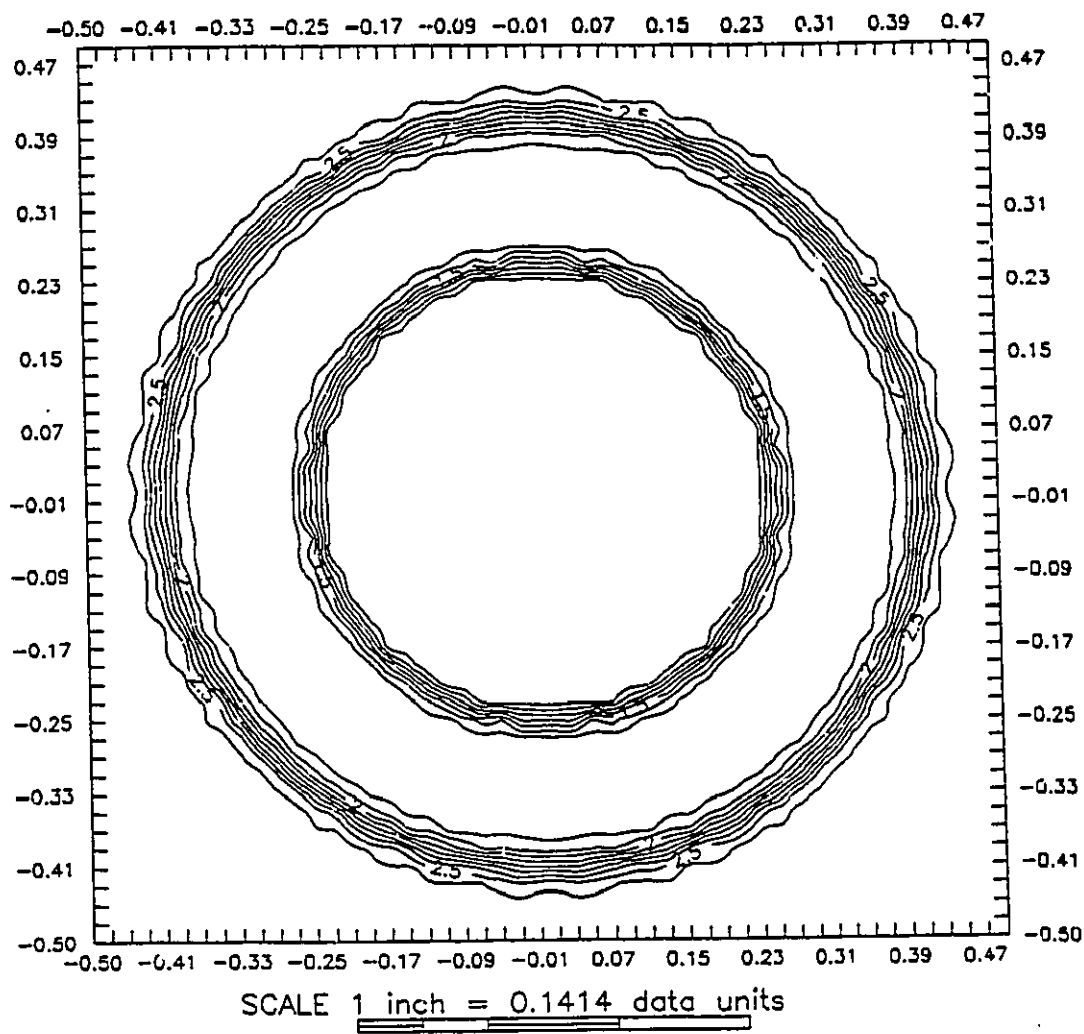
Figure (3.9a)- Iso-density contours for a converging cylindrical shock wave

No perturbation (t = 0.229, K = 4)

84
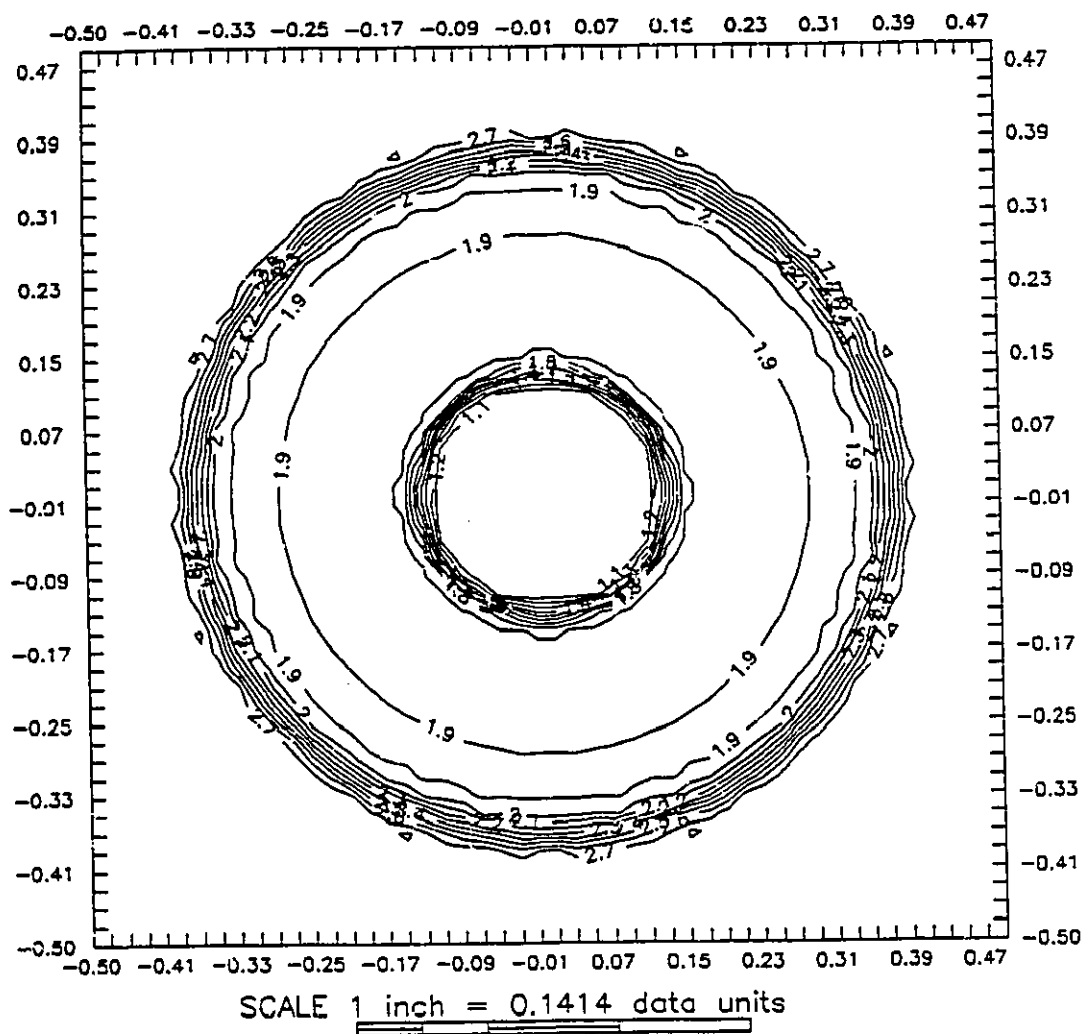
Figure (3.9b)- Iso-density contours for a converging cylindrical shock wave

No perturbation (t = 0.331, K = 4)
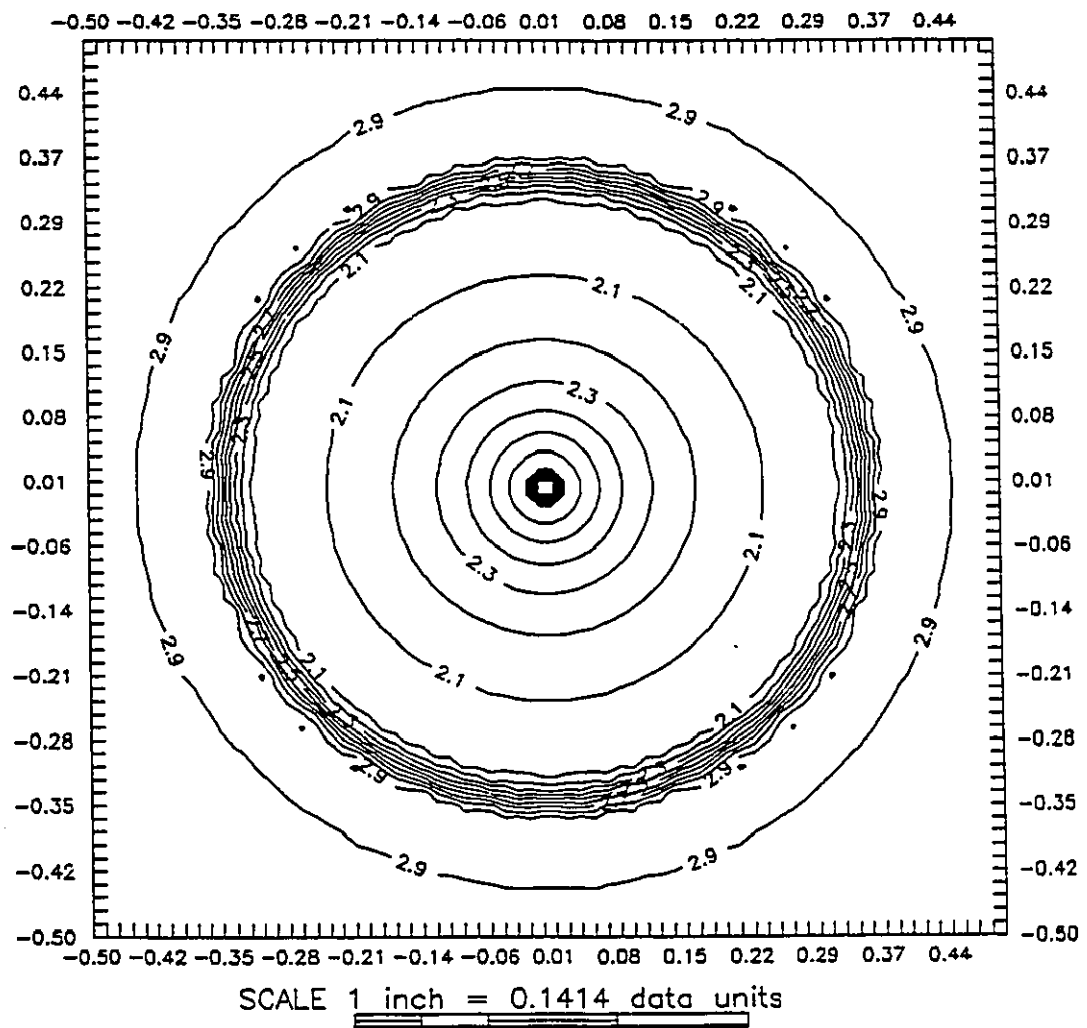
Figure (3.9c)- Iso-density contours for a converging cylindrical shock wave

No perturbation (t = 0.424, K = 4)
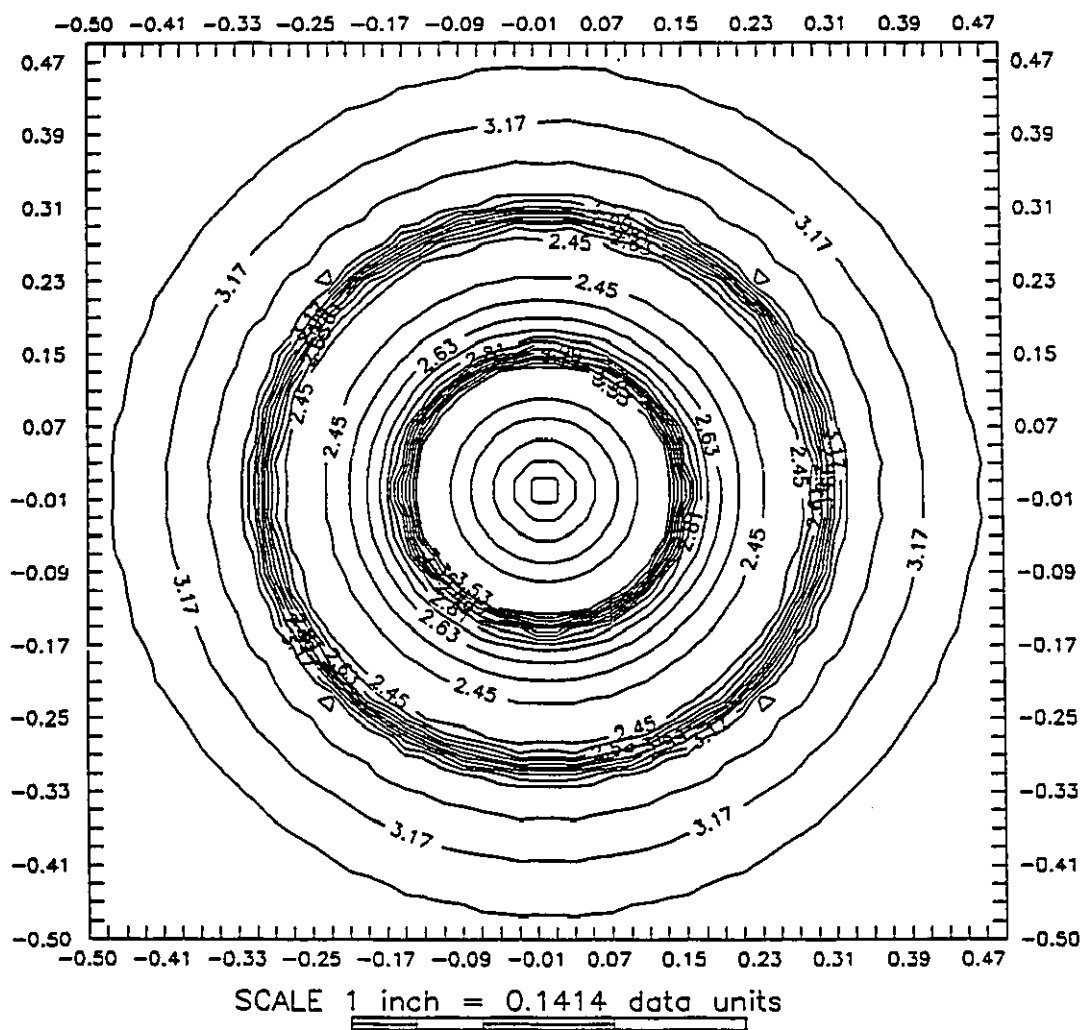
Figure (3.9d)- Iso-density contours for a converging cylindrical shock wave

No perturbation (t = 0.606, K = 4)
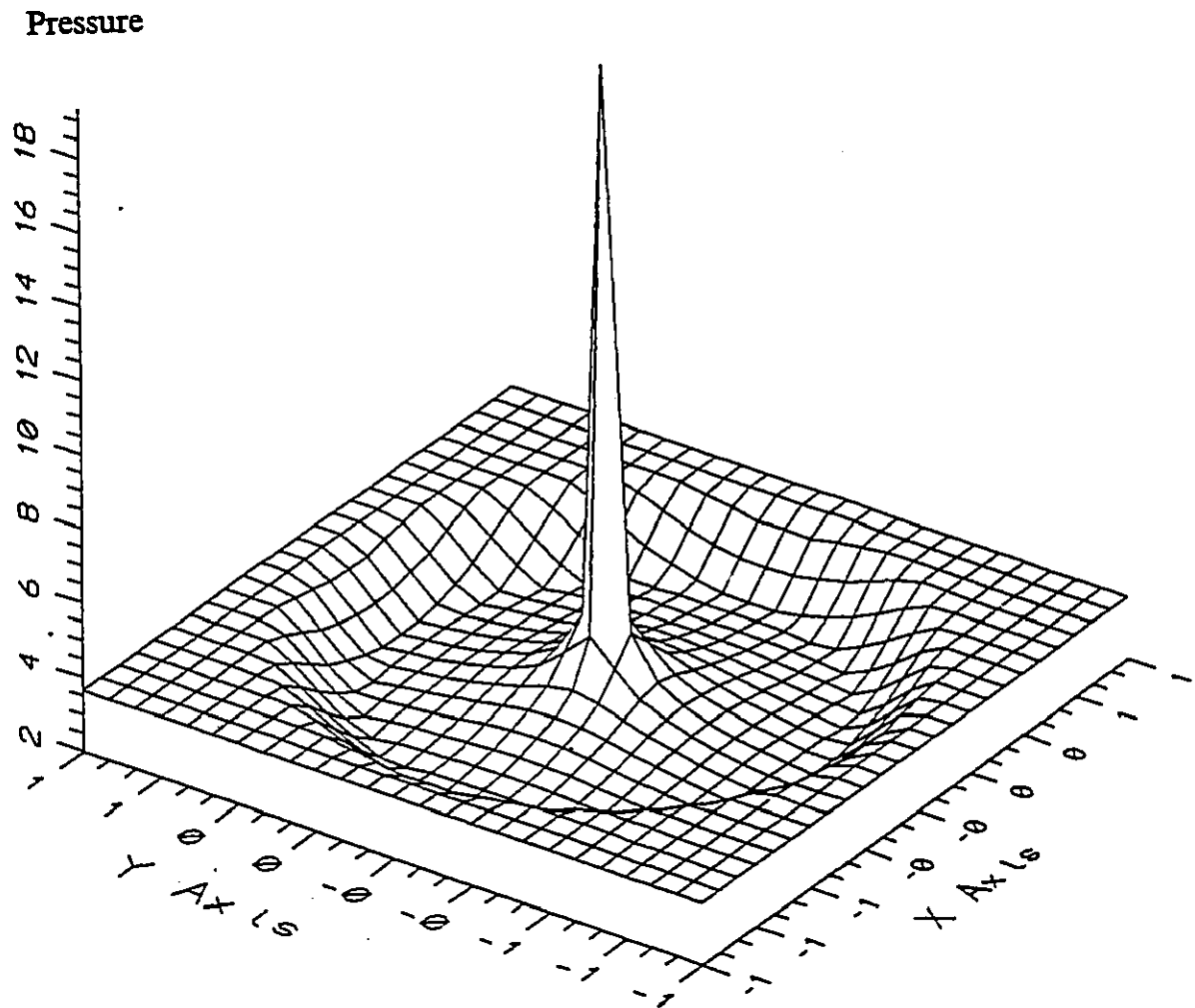
Pressure

Figure (3.10)- Pressure intensification near the axis for a converging cylindrical

shock wave, No perturbation (K = 3)
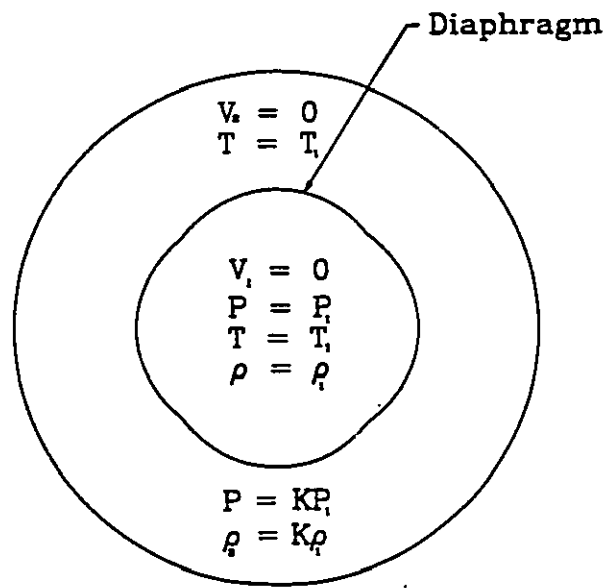
Figure (3.11)- Schematic for the 2D model with mode four perturbation
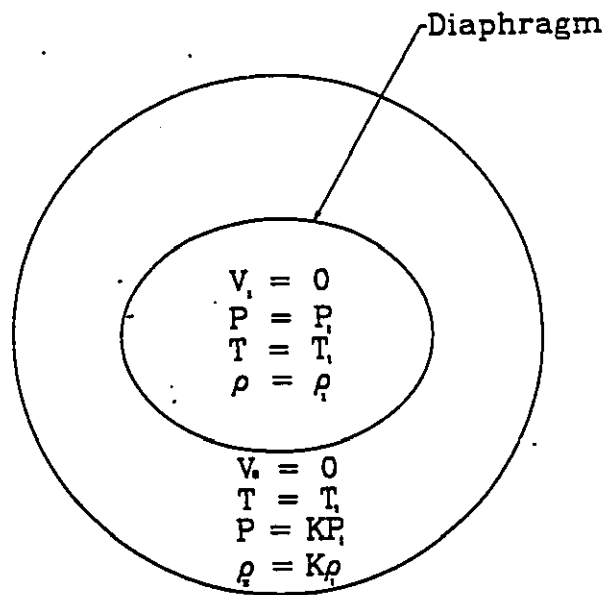
Figure (3.12)- Schematic for the 2D model with elliptical perturbation
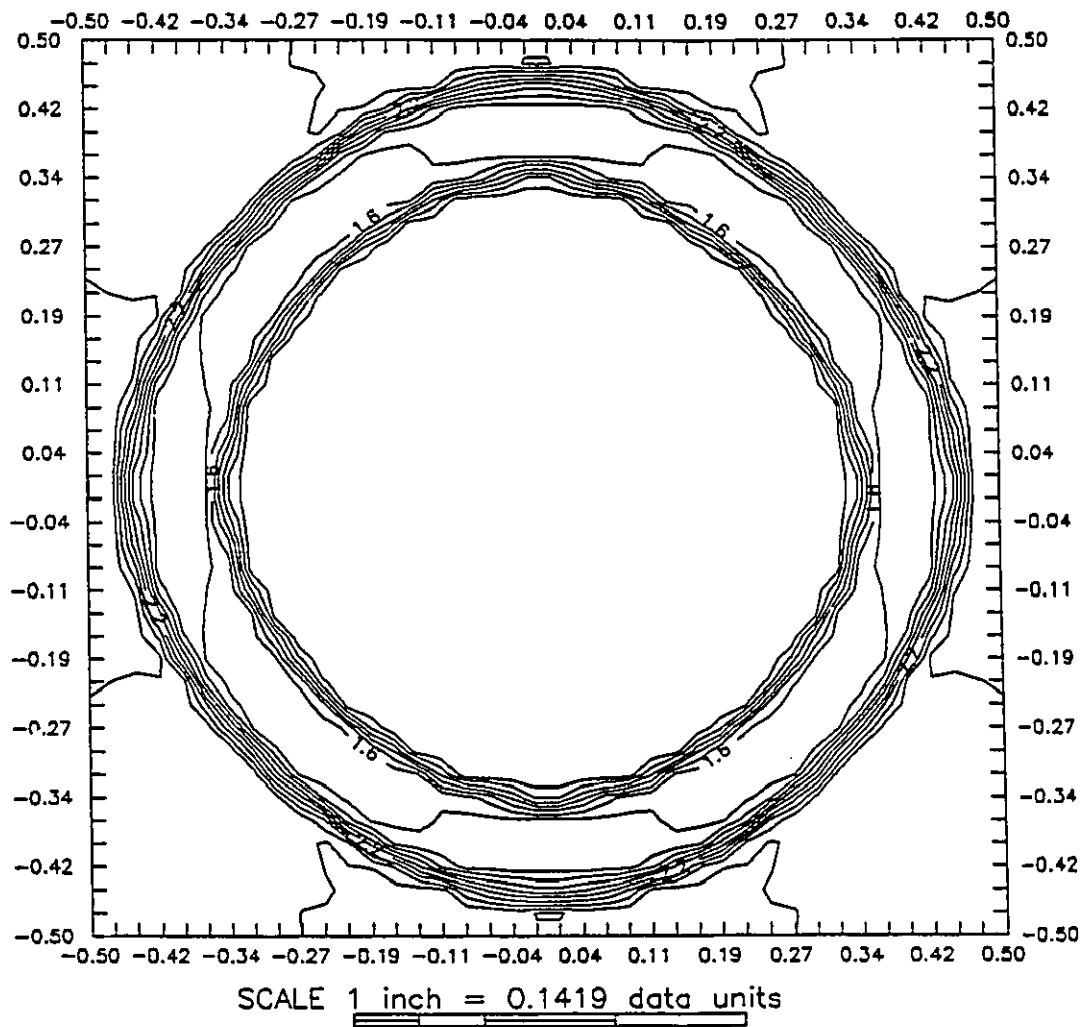
Figure (3.13a)- Iso-density contours for a converging cylindrical shock wave

(Mode = 4, t = 0.143, δ = 0.02, K = 4)

90
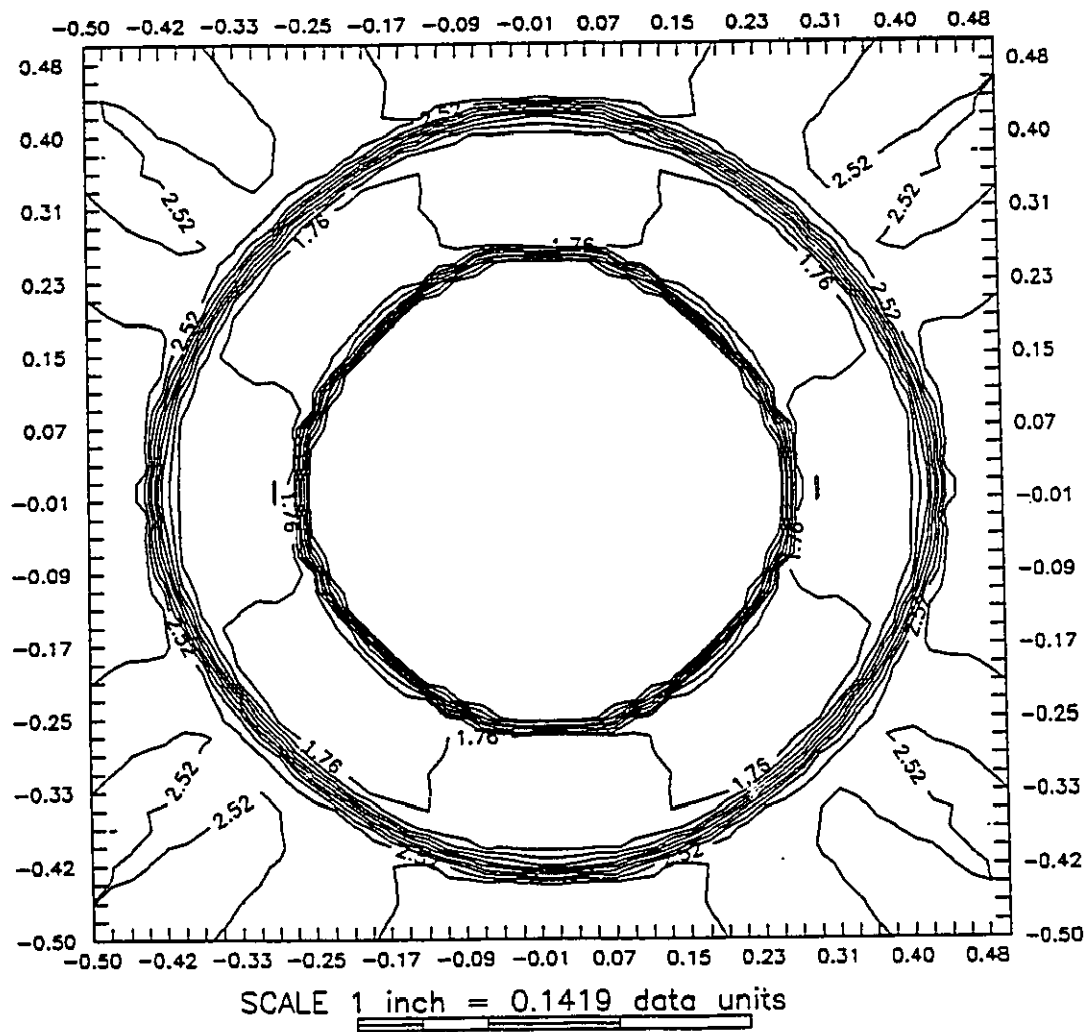
Figure (3.13b)- Iso-density contours for a converging cylindrical shock wave

(Mode = 4, t = 0.205, δ = 0.02, K = 4)

91
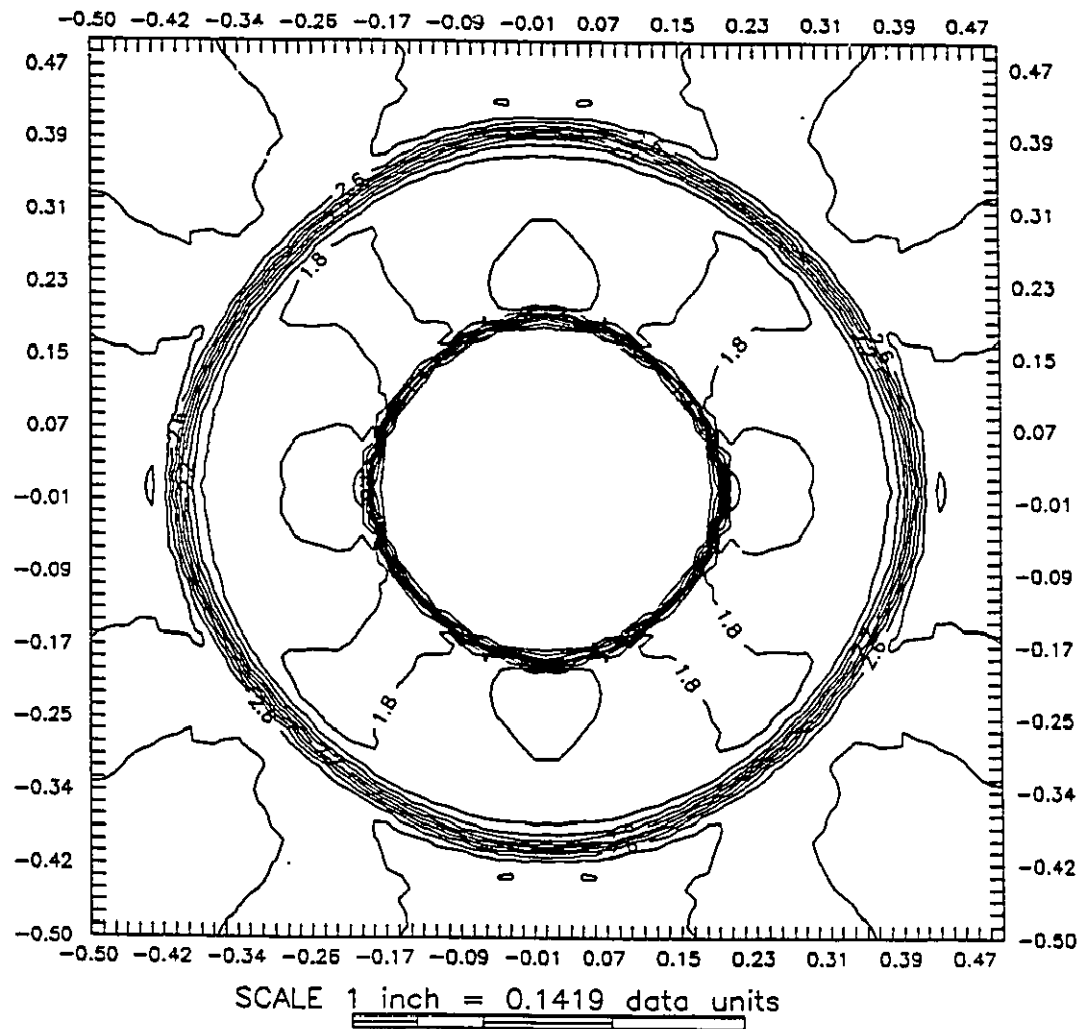
Figure (3.13c)- Iso-density contours for a converging cylindrical shock wave
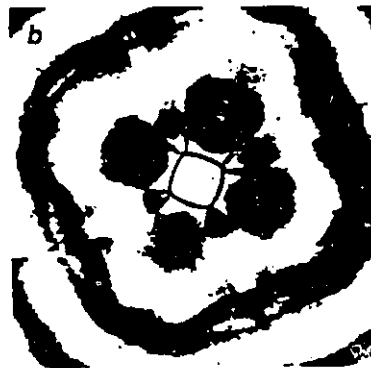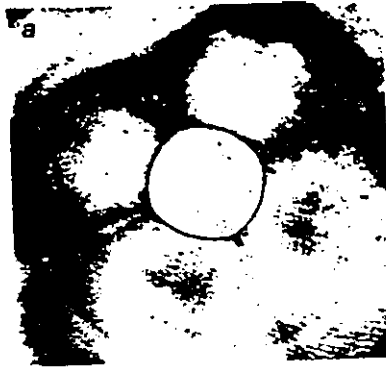
(Mode = 4, t = 0.259, δ = 0.02, K = 4)
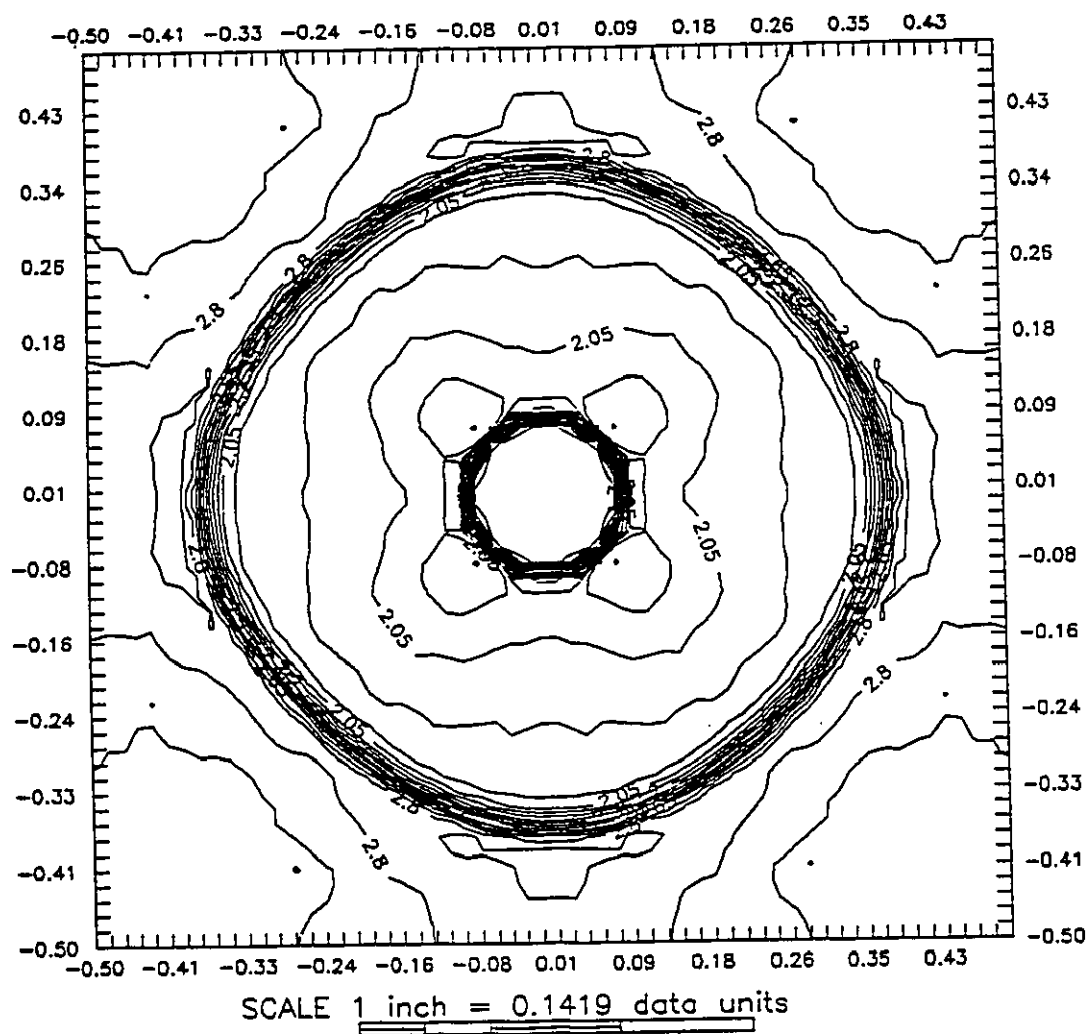
Figure (3.13d)- Iso-density contours for a converging cylindrical shock wave

(Mode = 4, t = 0.335, δ = 0.02, K = 4)
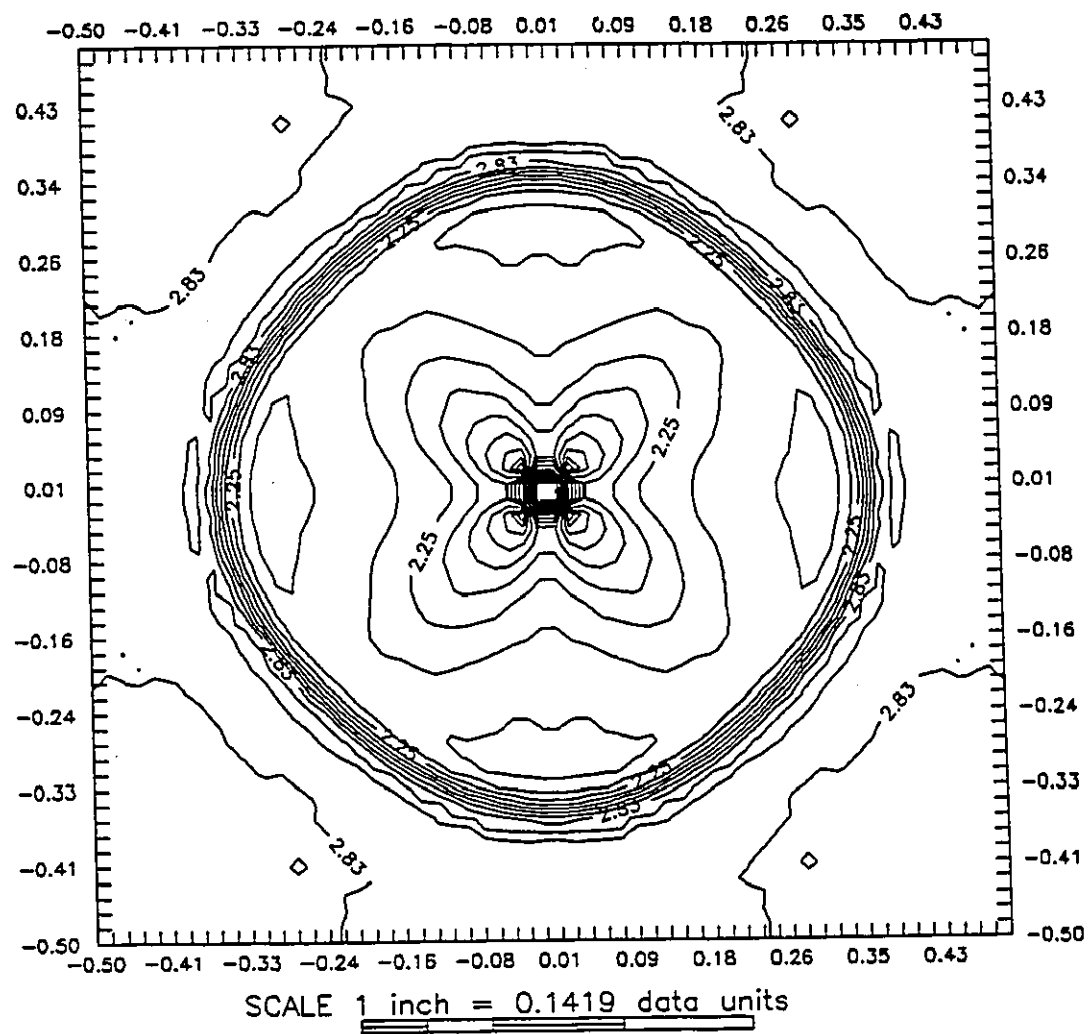
Figure (3.13e)- Iso-density contours for a converging cylindrical shock wave

(Mode = 4, t = 0.374, δ = 0.02, K = 4)
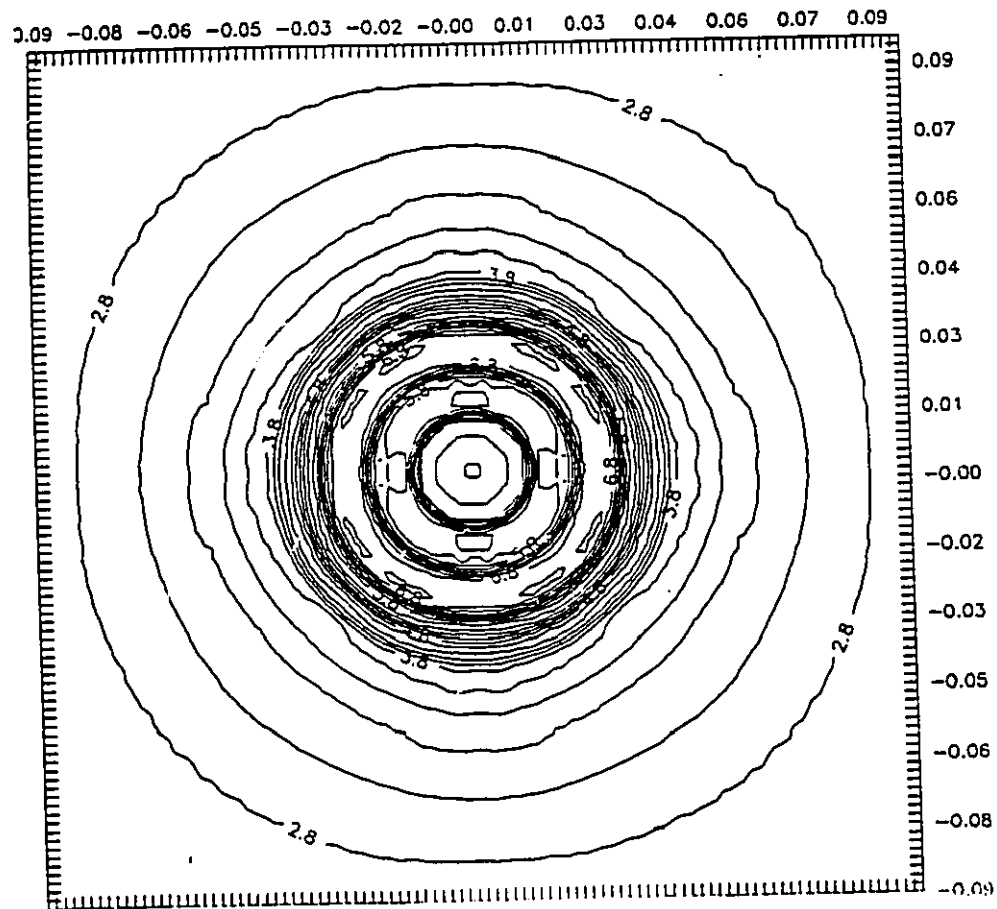
Figure (3.13f)- Iso-density contours for after the reflection for a cylindrical shock wave (Mode = 4, t = 0.475, δ = 0.02, K = 4)
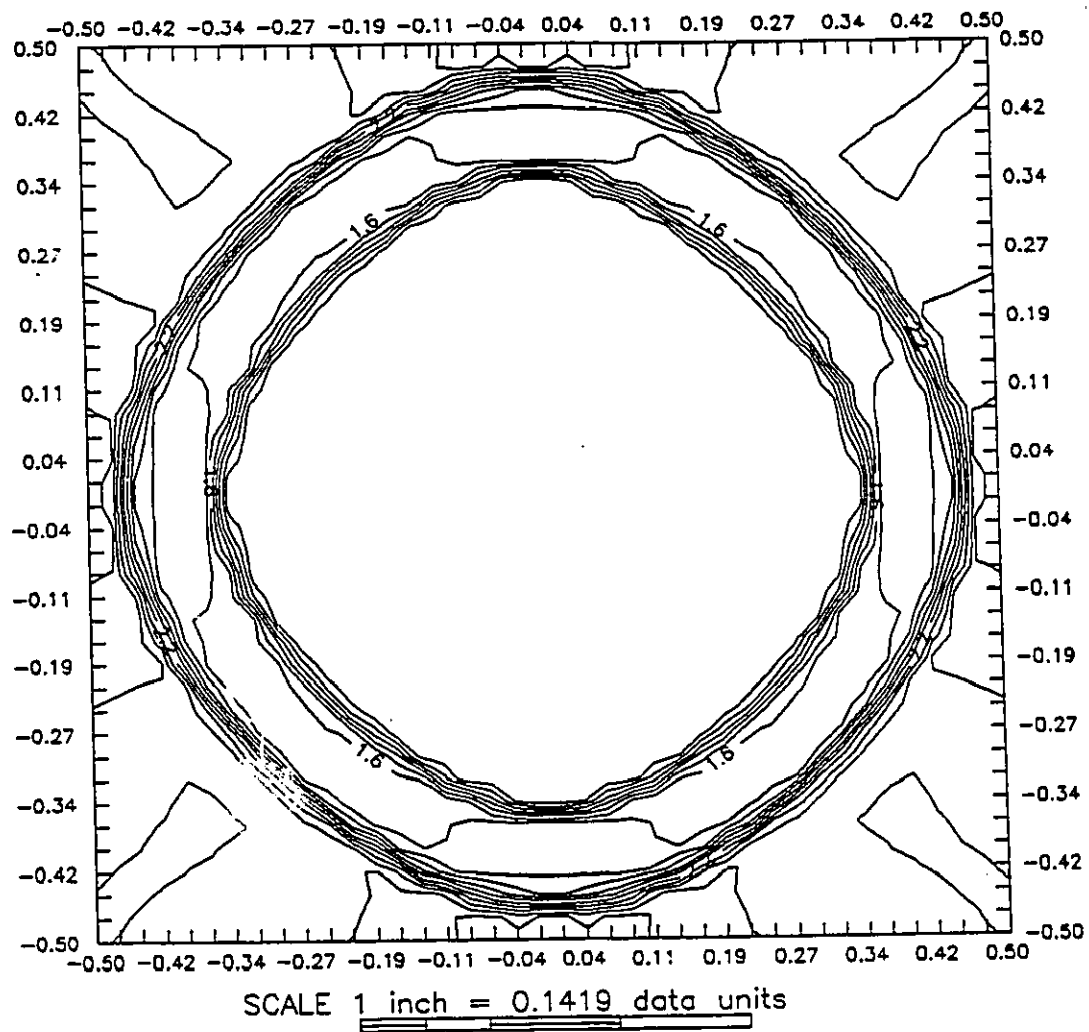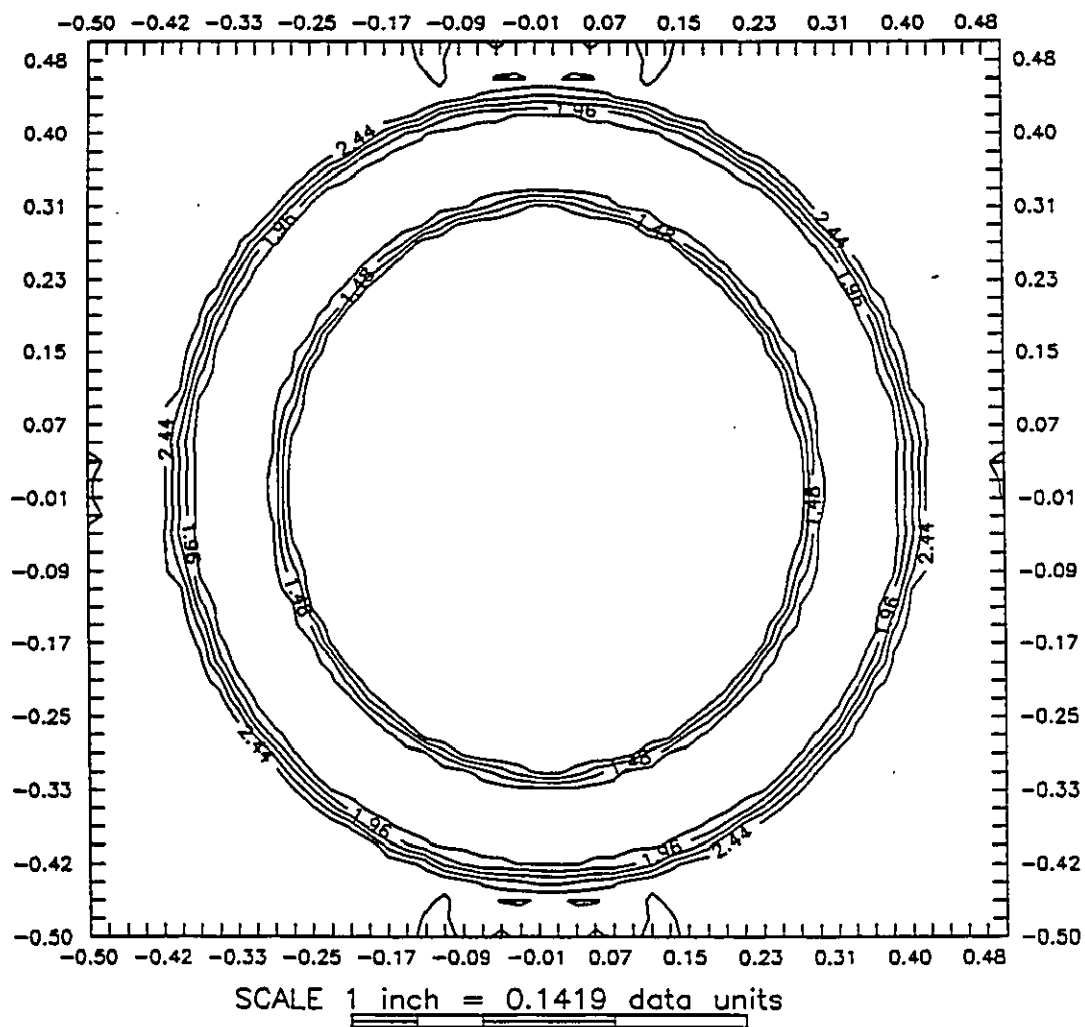
Figure (3.14a)- Iso-density contours for a converging cylindrical shock wave

(Mode = 4, t = 0.142, δ = 0.03, K = 4)
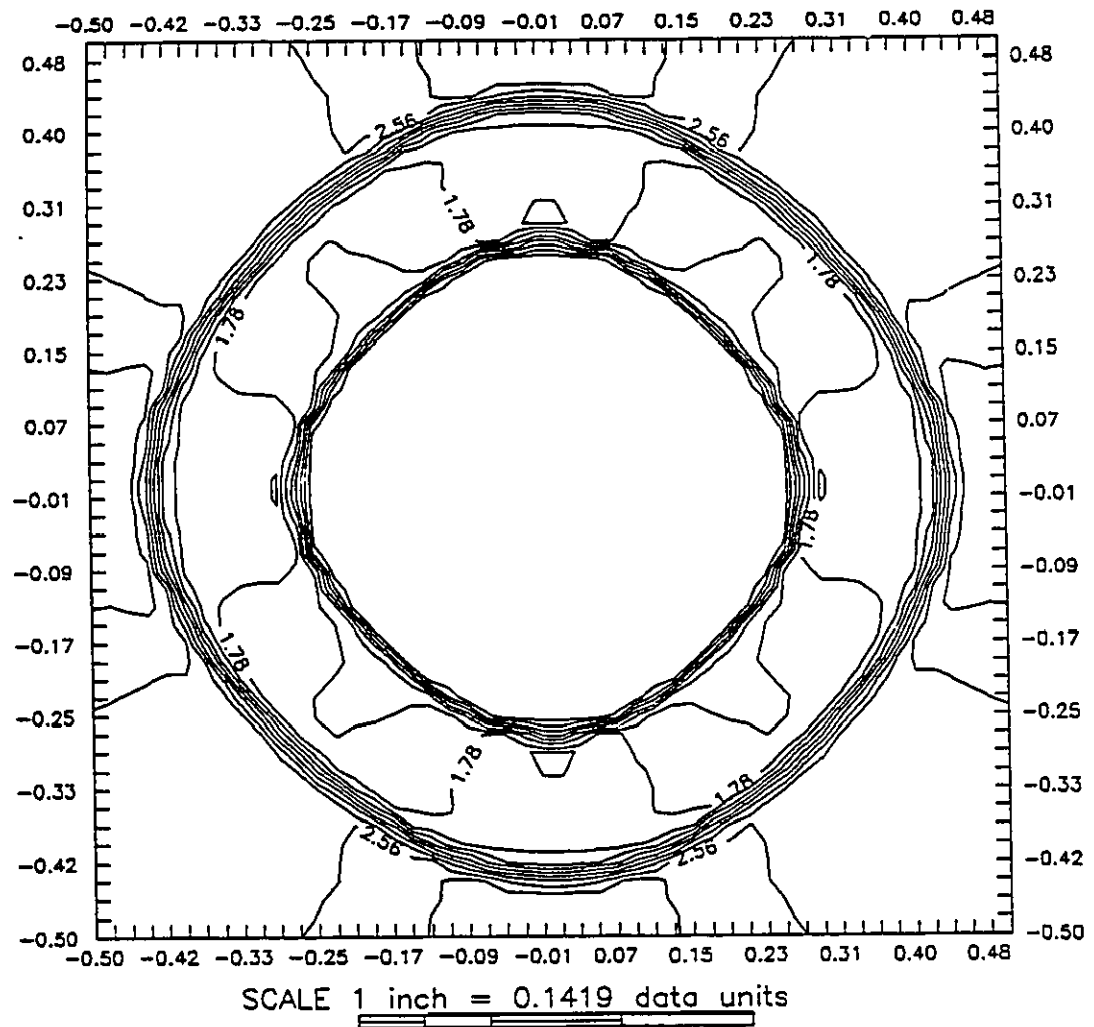
Figure (3.14b)- Iso-density contours for a converging cylindrical shock wave

(Mode = 4, t = 0.202, δ = 0.03, K = 4)

SCALE 1 inch = 0.1419 data units
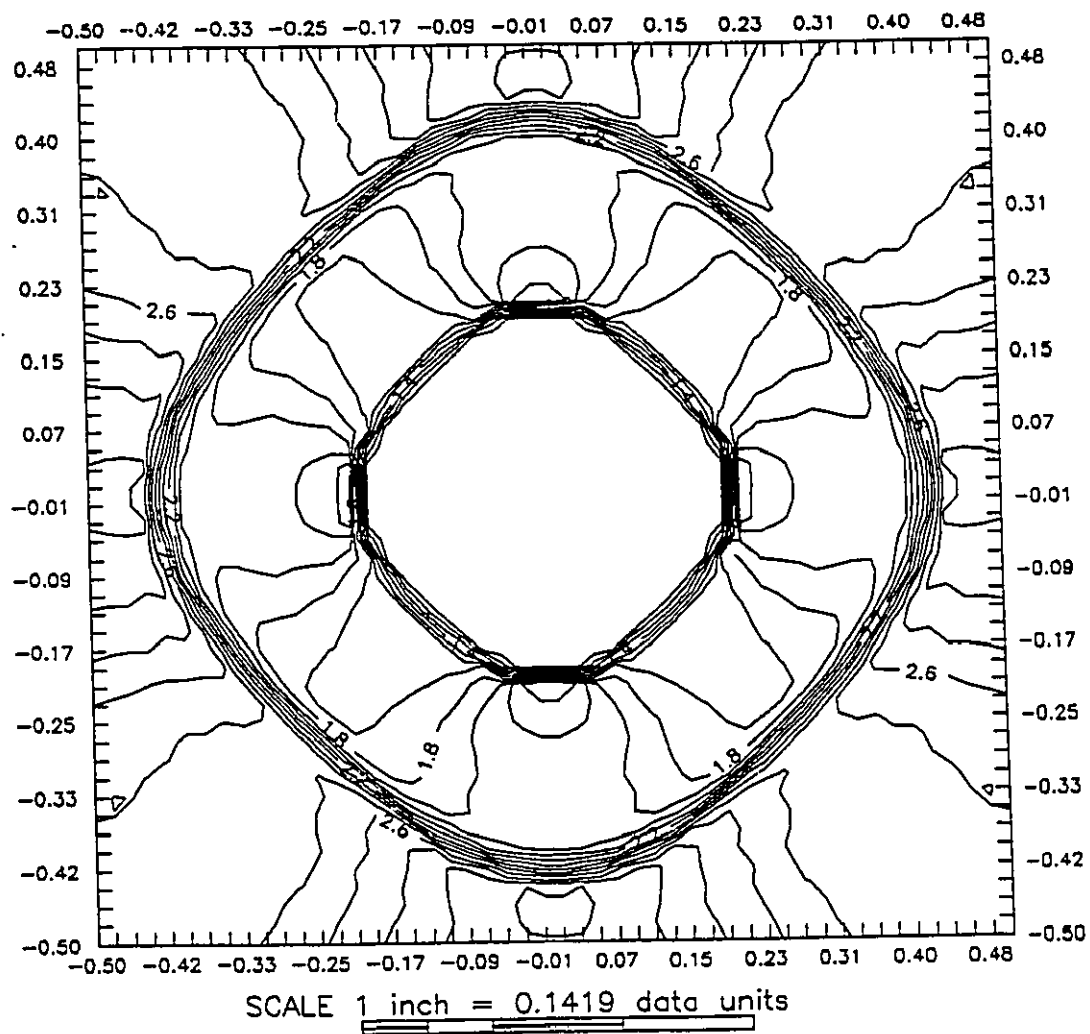
Figure (3.14c)- Iso-density contours for a converging cylindrical shock wave

(Mode = 4, t = 0.251, δ = 0.03, K = 4)
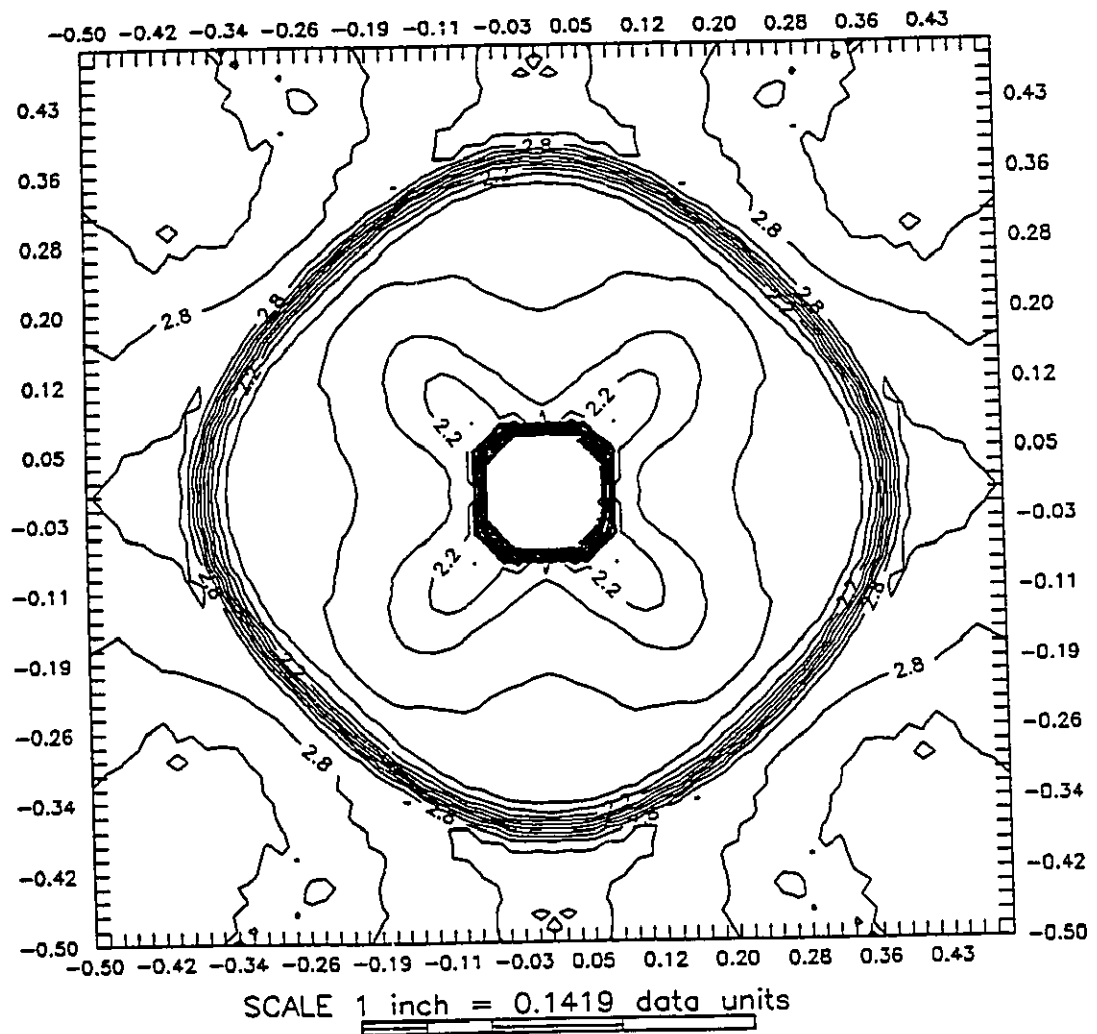
Figure (3.14d)- Iso-density contours for a converging cylindrical shock wave

(Mode = 4, t = 0.342, δ = 0.03, K = 4)

99

Figure (3.14e)- Iso-density contours for a converging cylindrical shock wave

(Mode = 4, t = 0.389, δ = 0.03, K = 4)
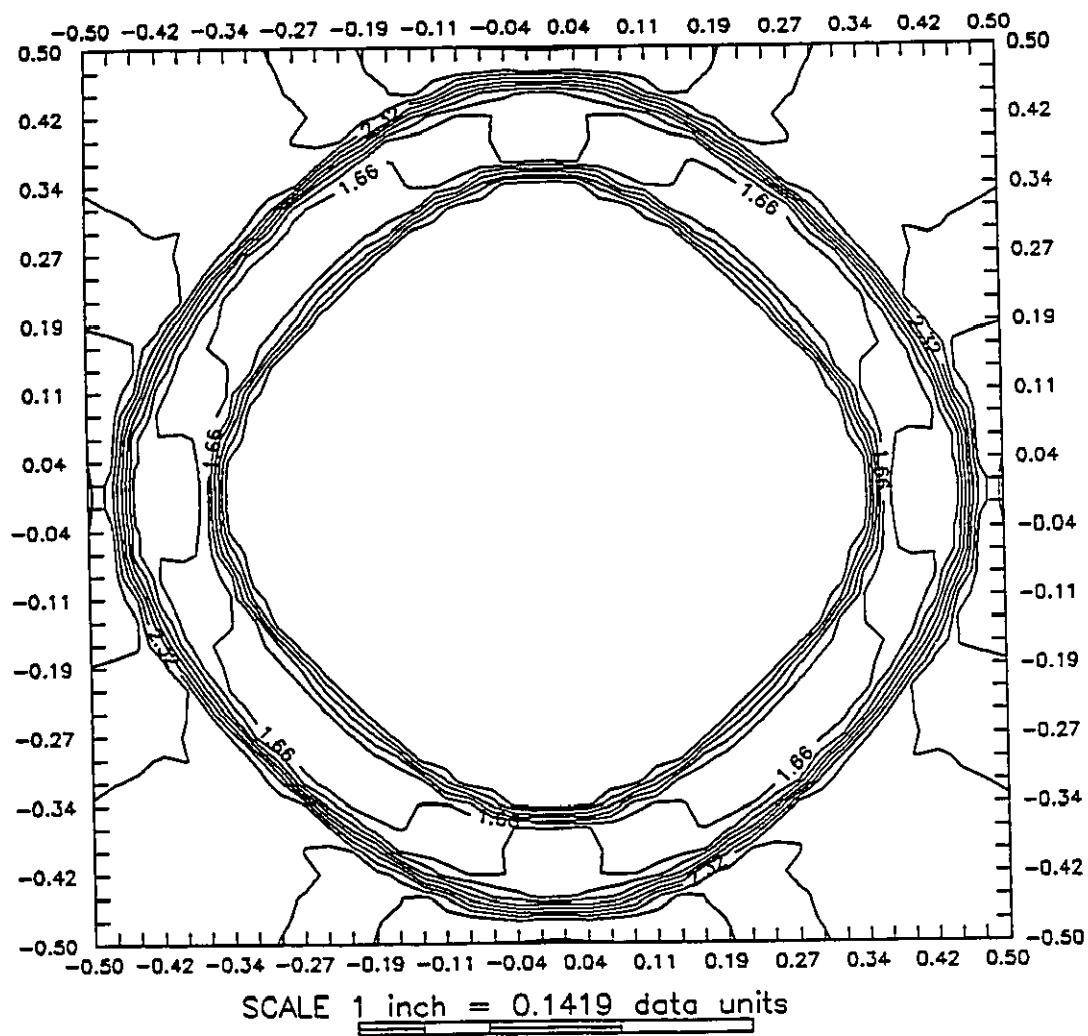
Figure (3.15a)- Iso-density contours for a converging cylindrical shock wave

(Mode = 4, t = 0.141, δ = 0.04, K = 4)

SCALE 1 inch = 0.1419 data units

Figure (3.15b)- Iso-density contours for a converging cylindrical shock wave

(Mode = 4, t = 0.214, δ = 0.04, K = 4)

102
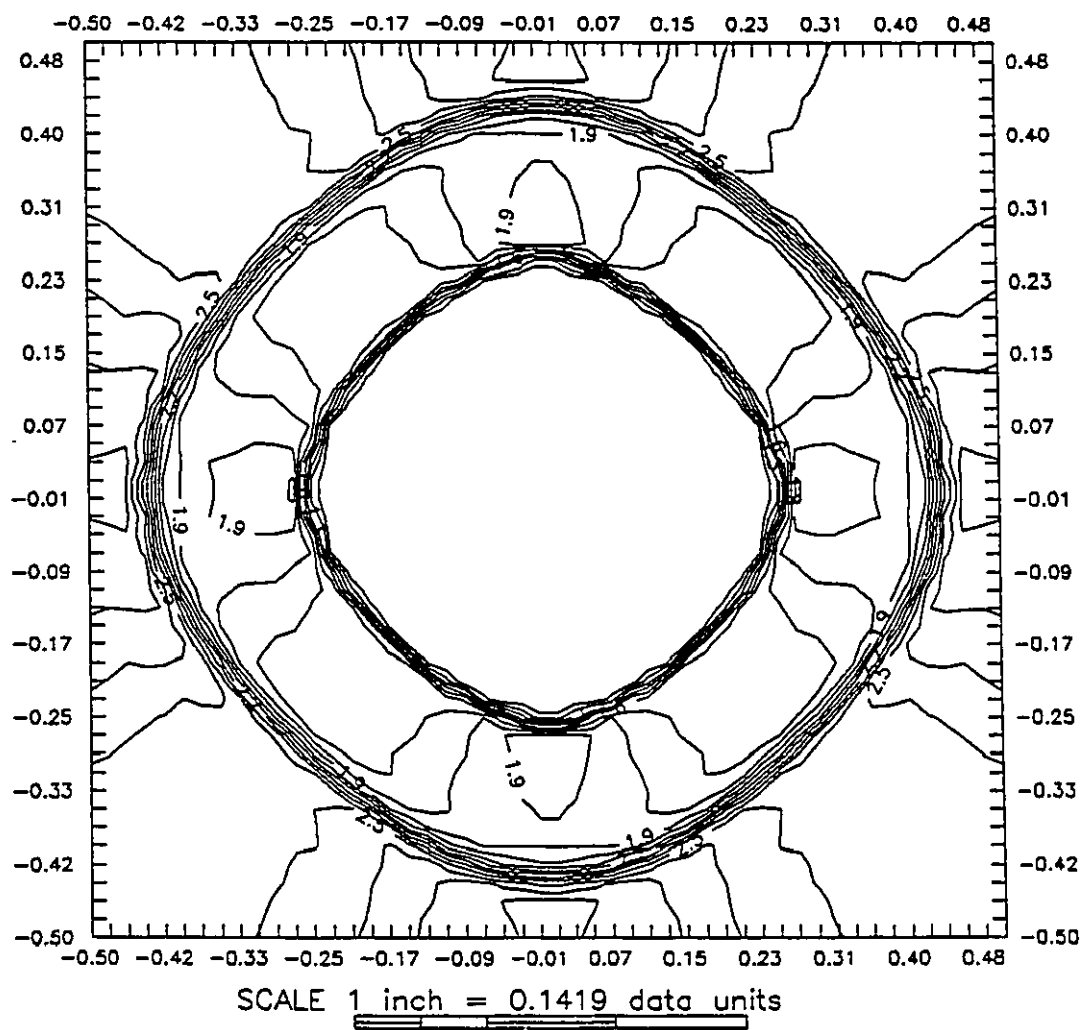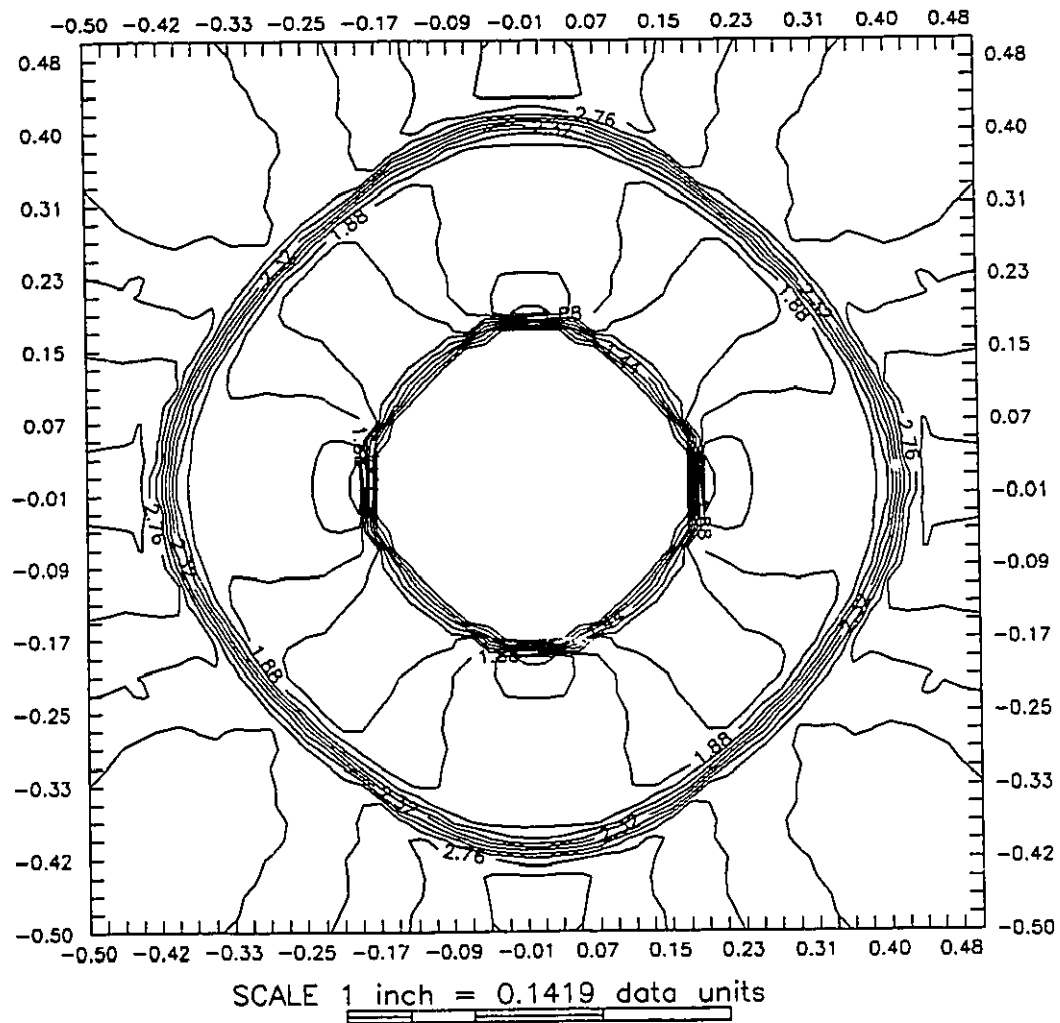
Figure (3.15c)- Iso-density contours for a converging cylindrical shock wave

(Mode = 4, t = 0.265, δ = 0.04, K = 4)

103
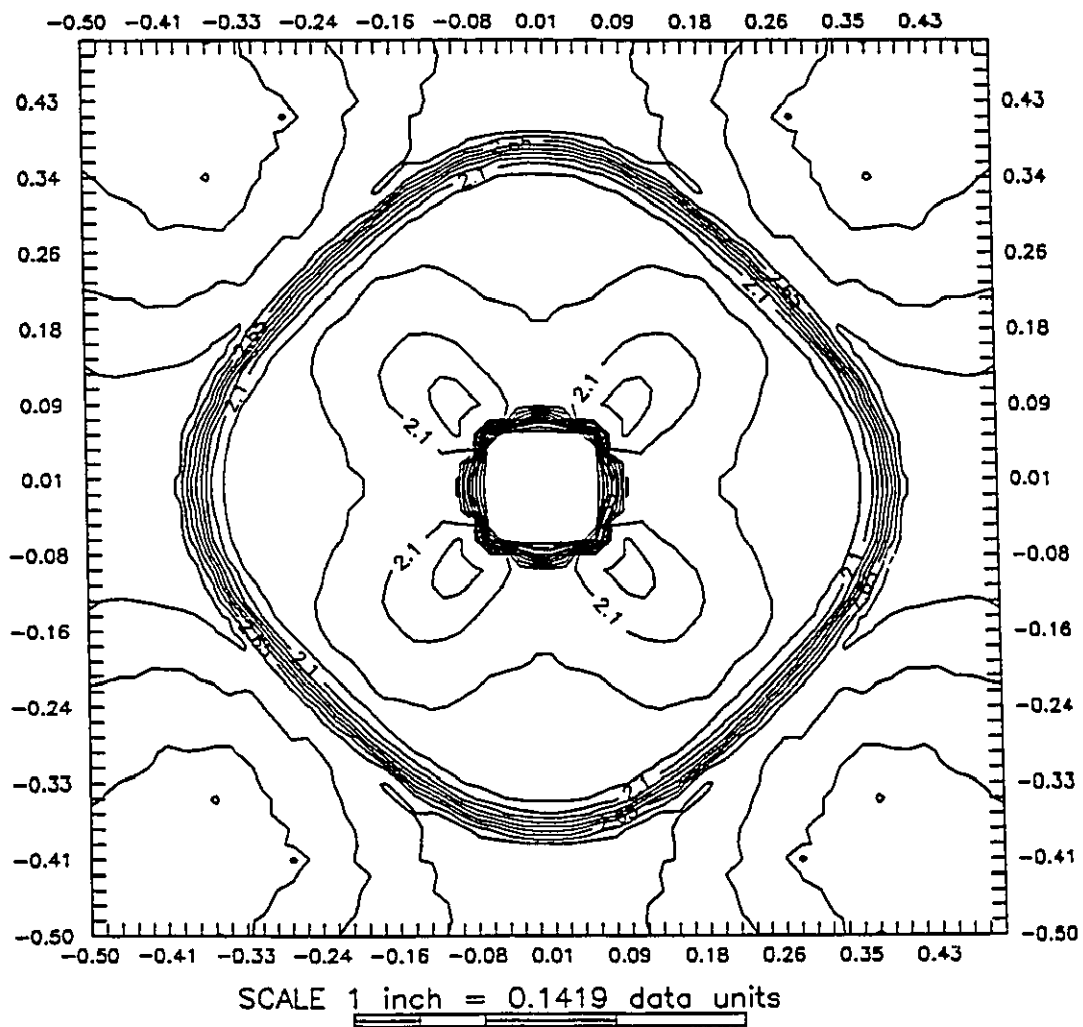
Figure (3.15d)- Iso-density contours for a converging cylindrical shock wave

(Mode = 4, t = 0.338, δ = 0.04, K = 4)

104
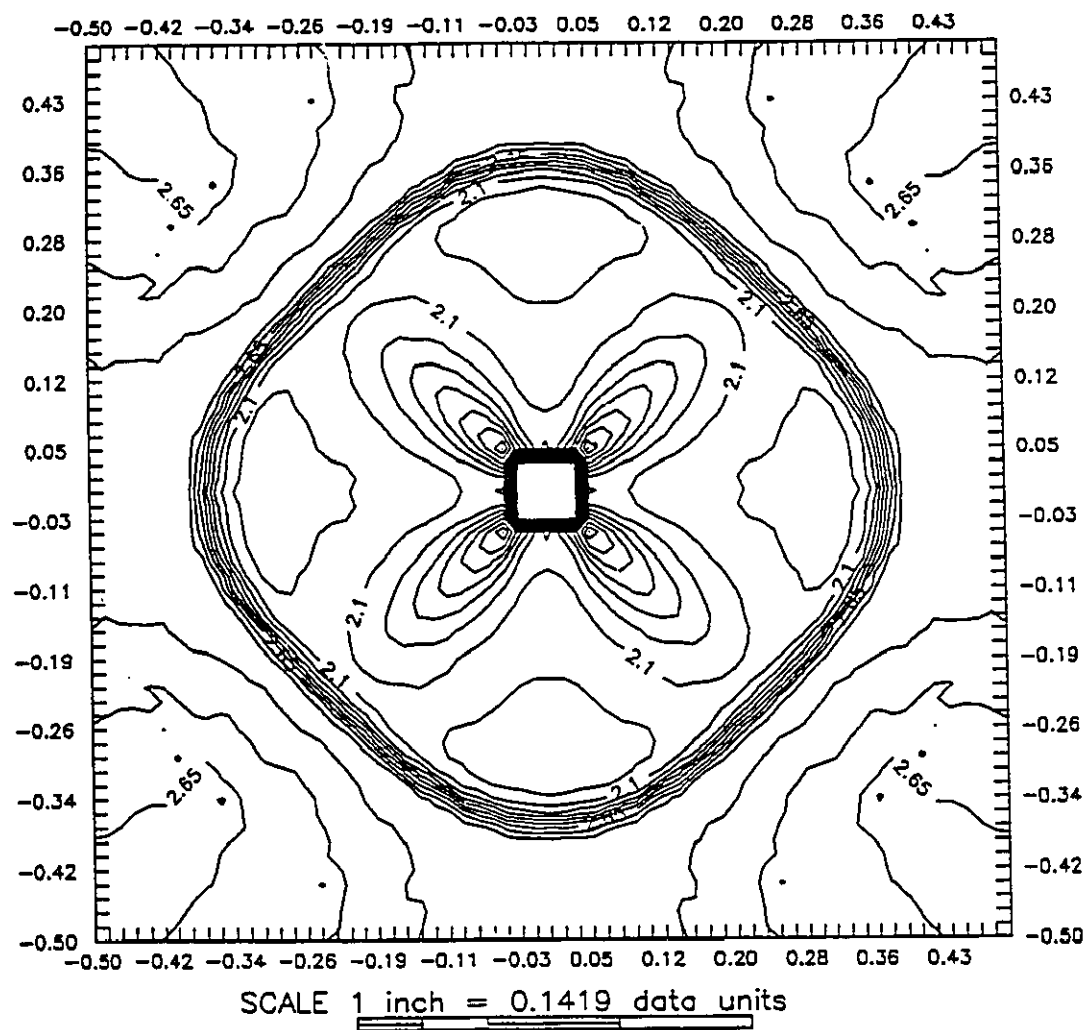
Figure (3.15e)- Iso-density contours for a converging cylindrical shock wave

(Mode = 4, t = 0.362, δ = 0.04, K = 4)

Figure (3.16)- Interferograms for mode 4 perturbation of a converging cylindrical shock wave (Wanatabe [45])
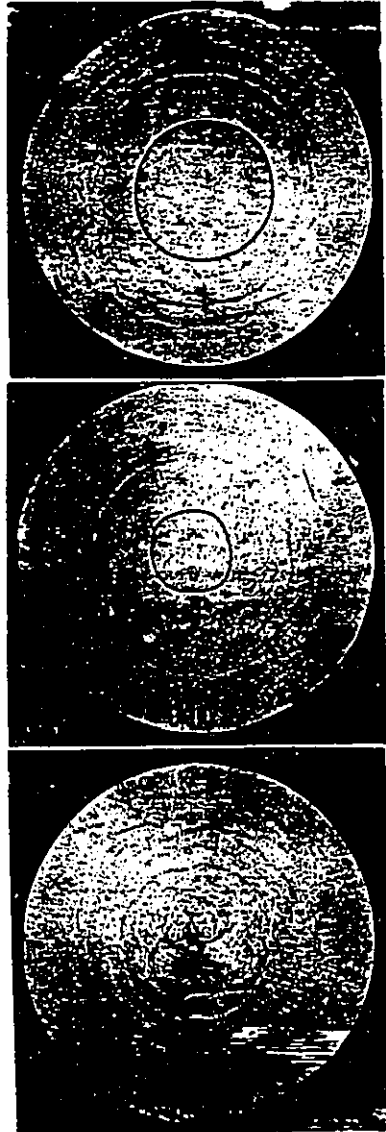
Figure (3.16a)- Shadowgraph for mode 4 square perturbation of a converging

cylindrical shock wave (Neemeh [48])

107

Amplification of the shock wave's distortion
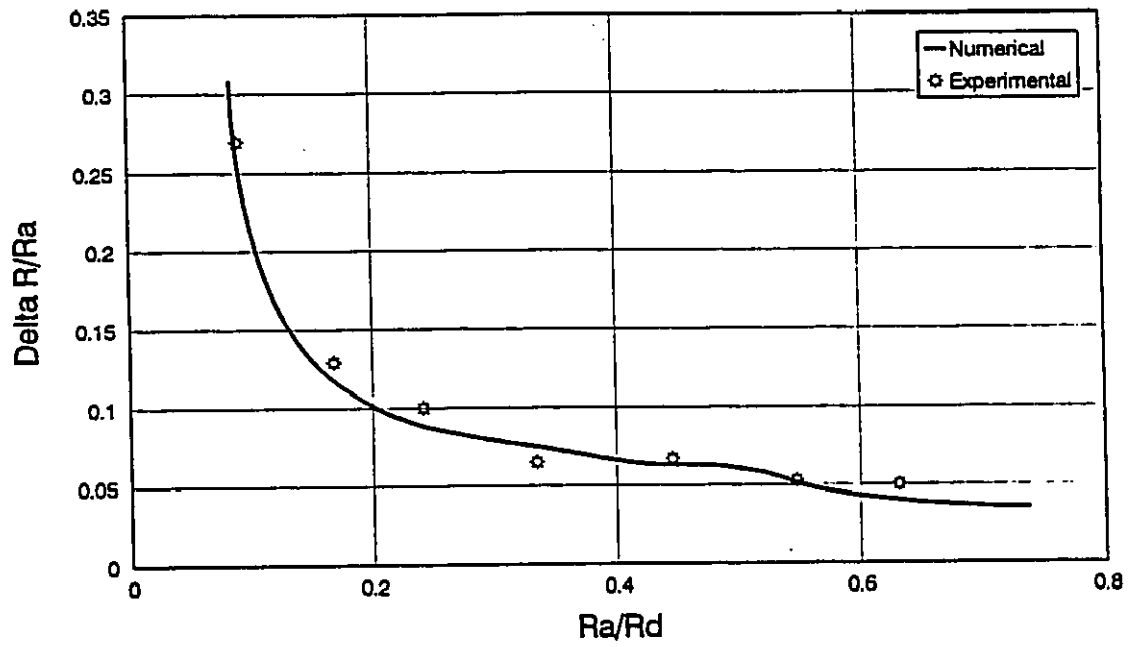
Experimental data from Ref. [45]

Figure (3.17)- Amplification of the distortion for a mode 4 converging cylindrical
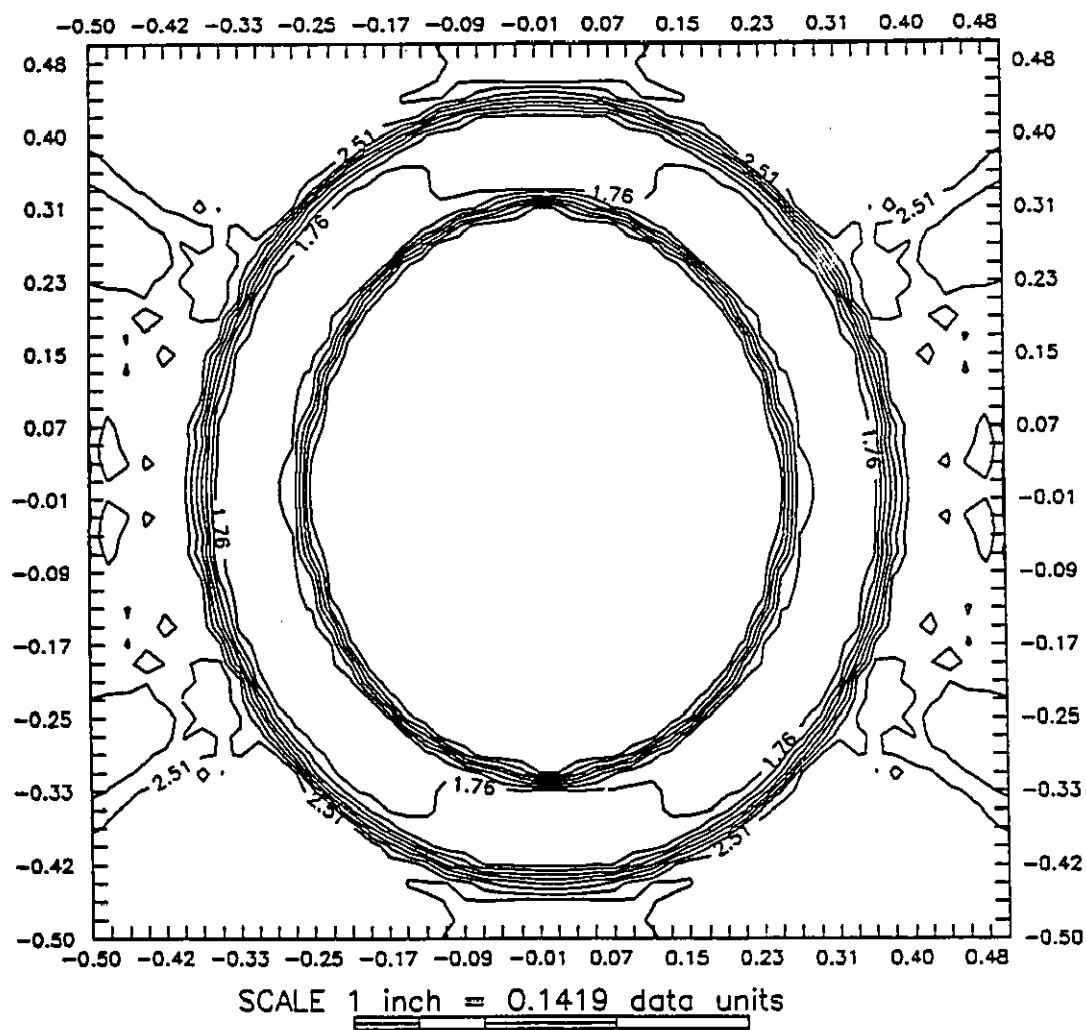
shock wave

108

Figure (3.18a)- Iso-density contours for a converging elliptical shock wave

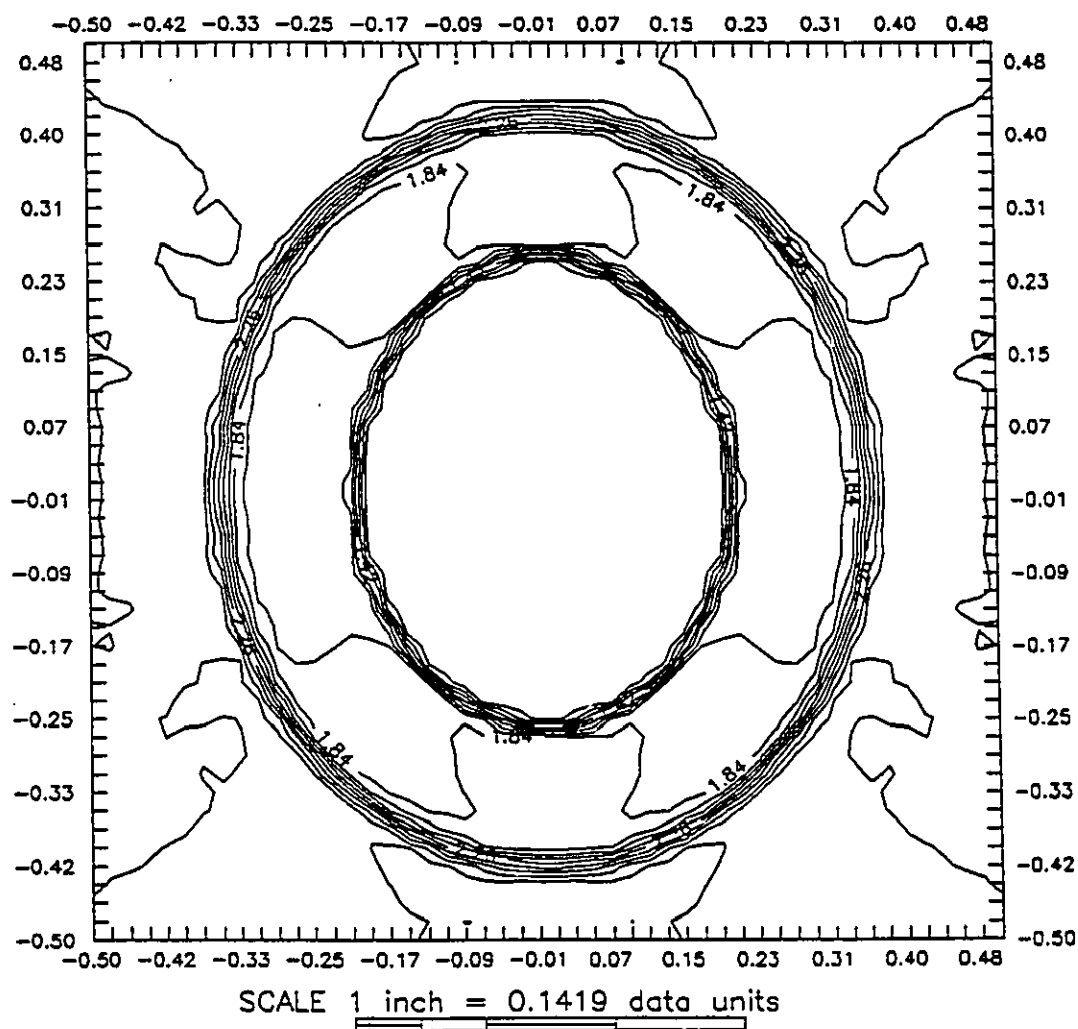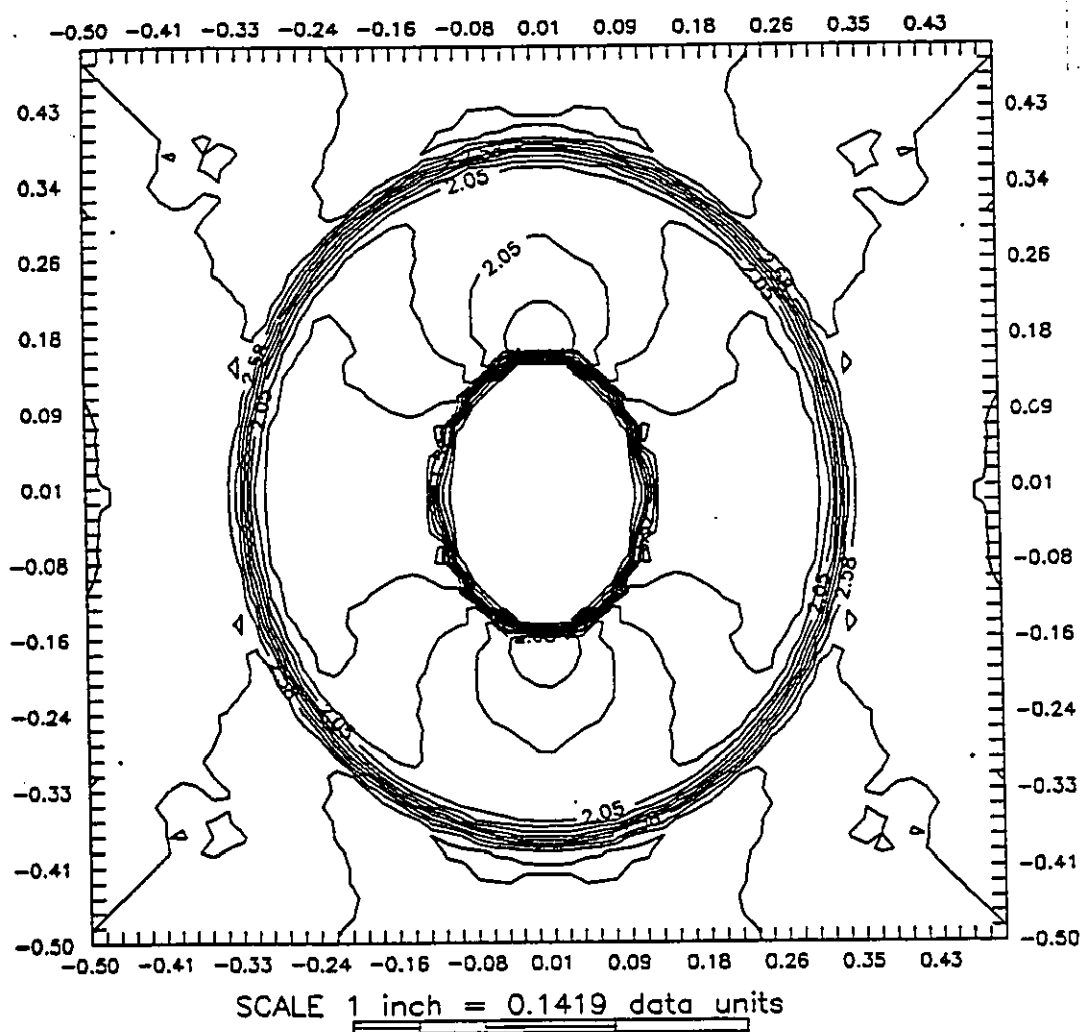$(t = 0.158, \xi_0 = 0.0415, K = 4)$

109
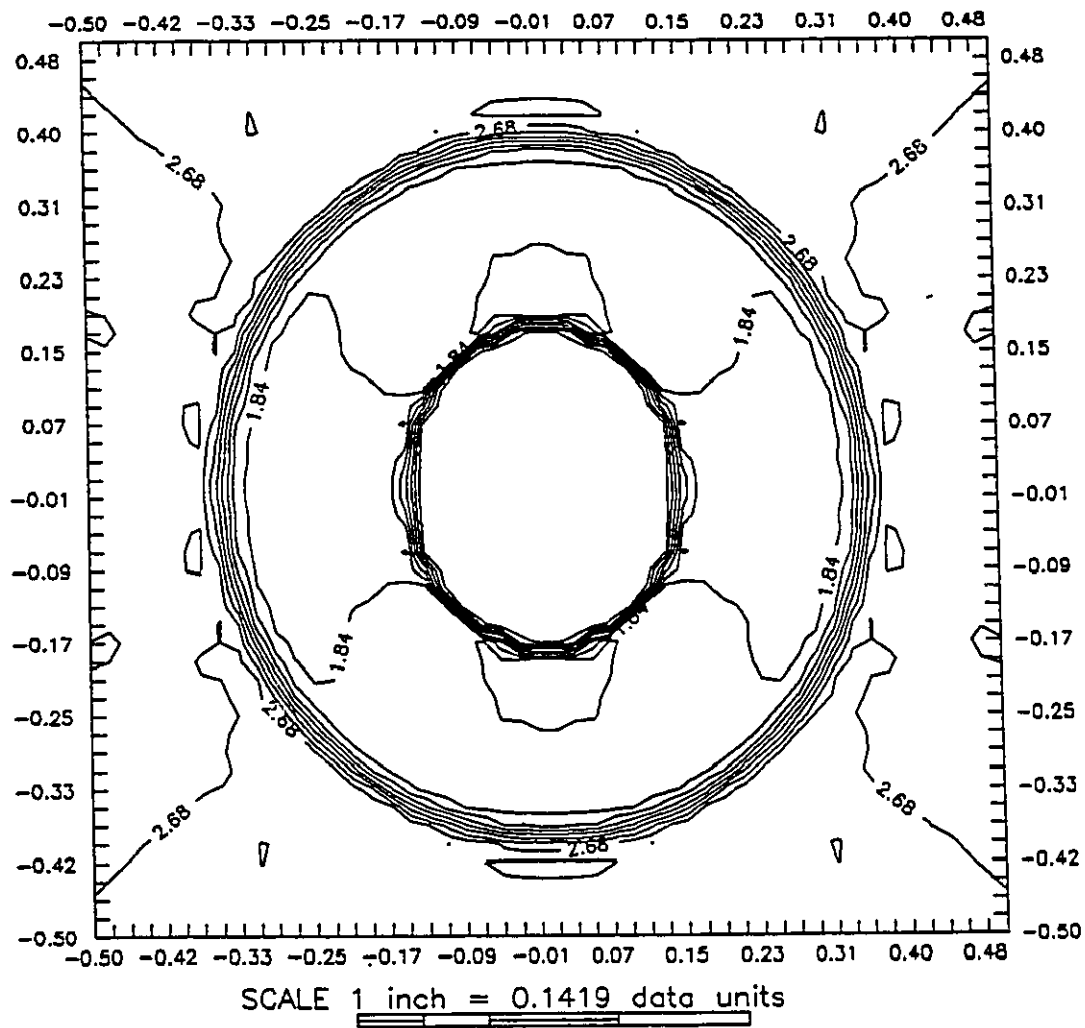
Figure (3.18b)- Iso-density contours for a converging elliptical shock wave

$$(t = 0.261, \xi_0 = 0.0415, K = 4)$$
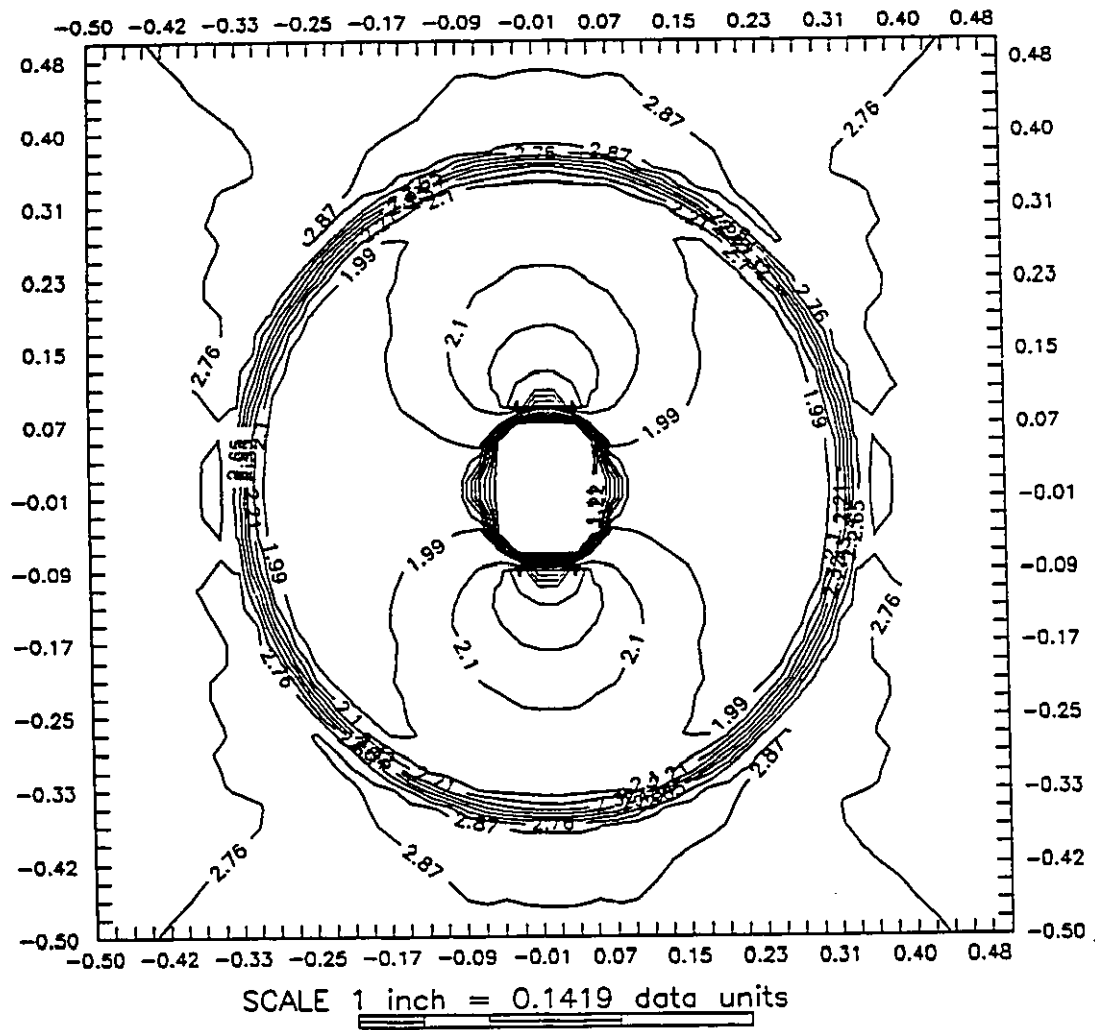
Figure (3.18c)- Iso-density contours for a converging elliptical shock wave

$(t = 0.322, \xi_o = 0.0415, K = 4)$

111
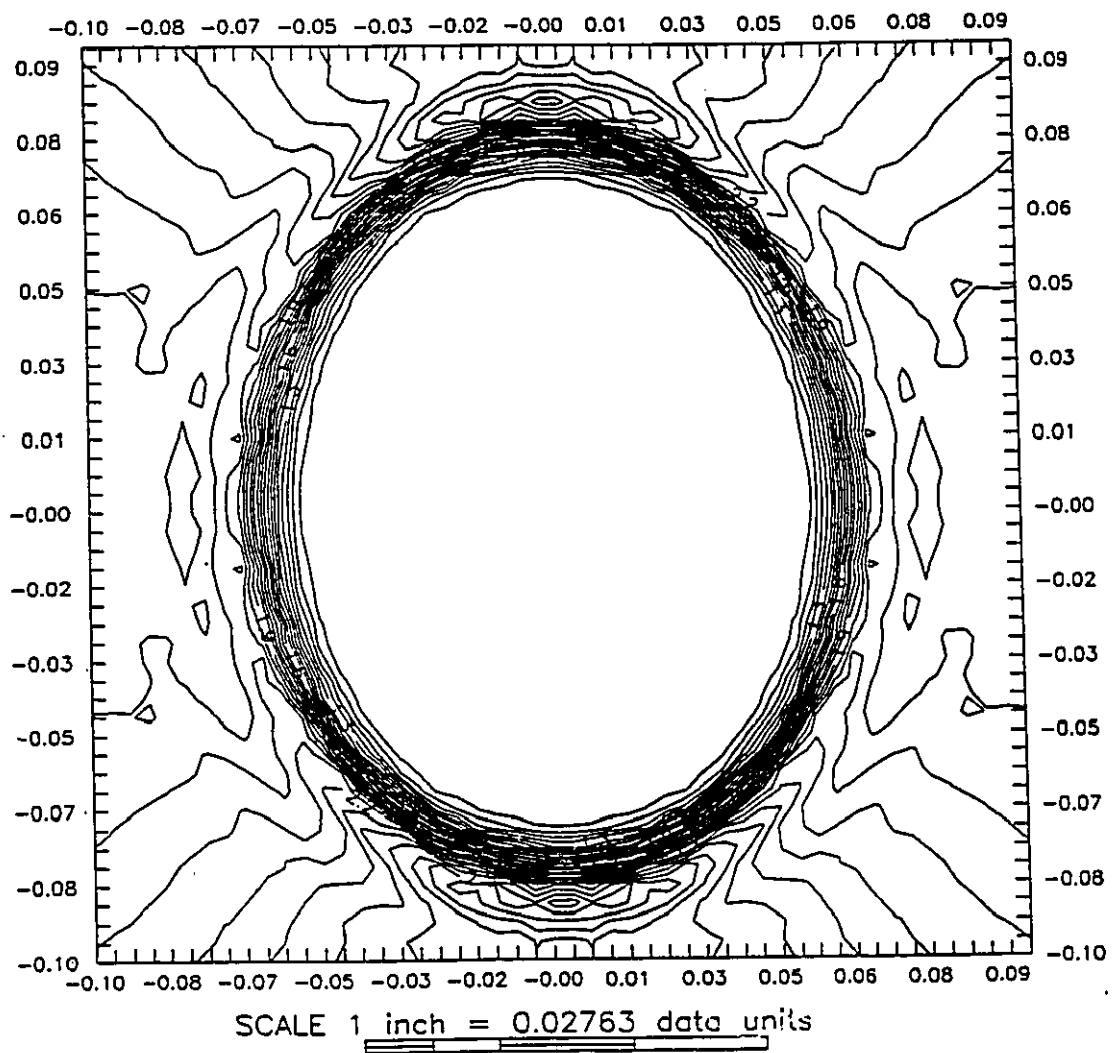
Figure (3.18d)- Iso-density contours for a converging elliptical shock wave

$(t = 0.330, \xi_o = 0.0415, K = 4, \text{Blown up})$
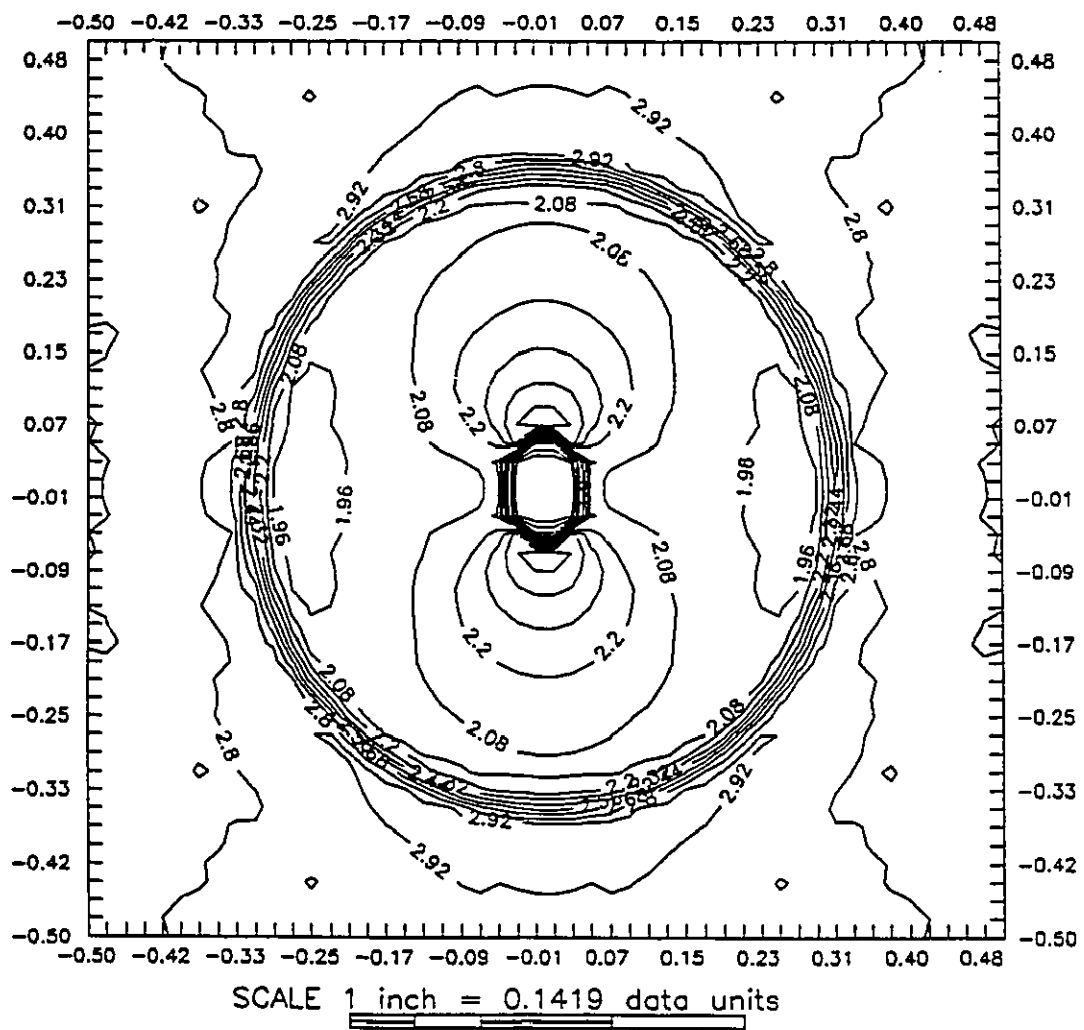
Figure (3.18e)- Iso-density contours for a converging elliptical shock wave
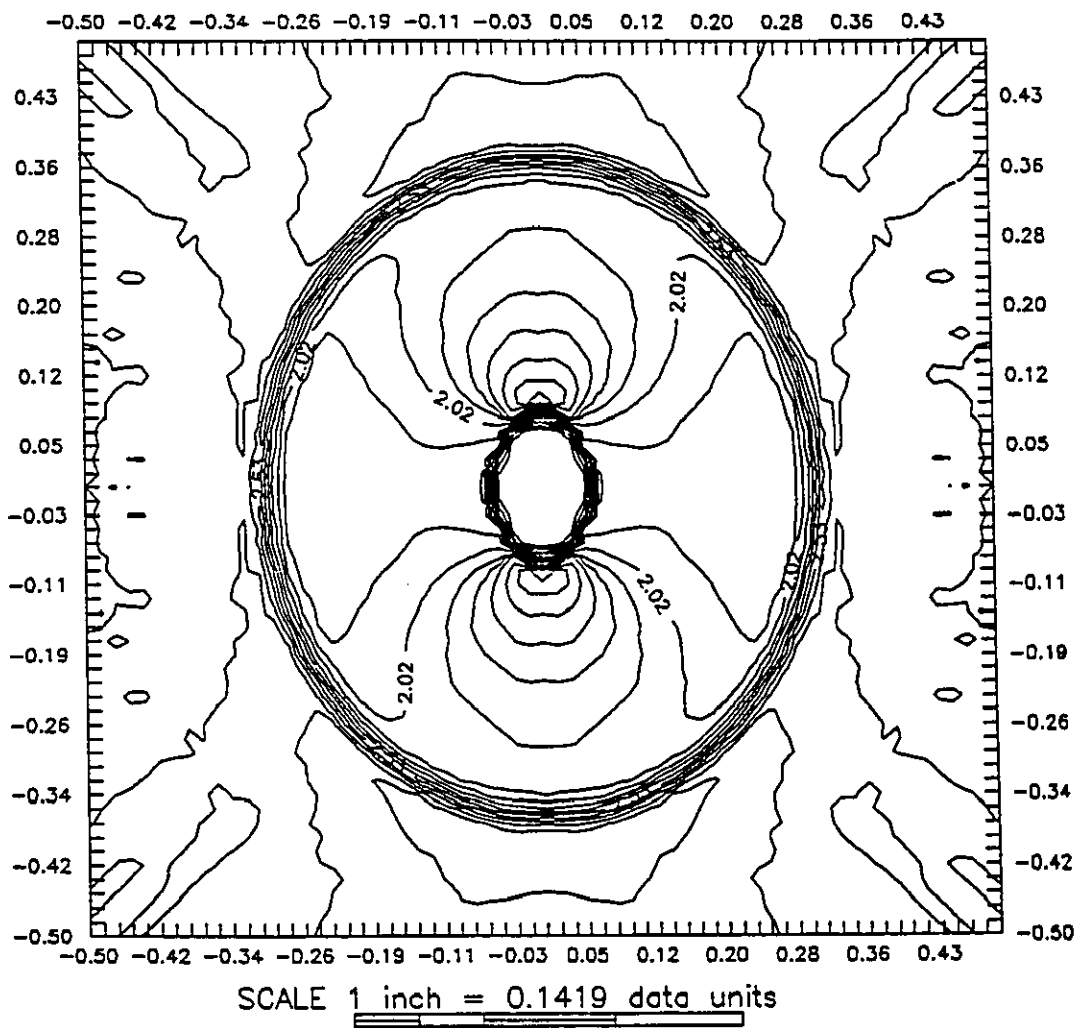
$(t = 0.345, \xi_0 = 0.0415, K = 4)$

113
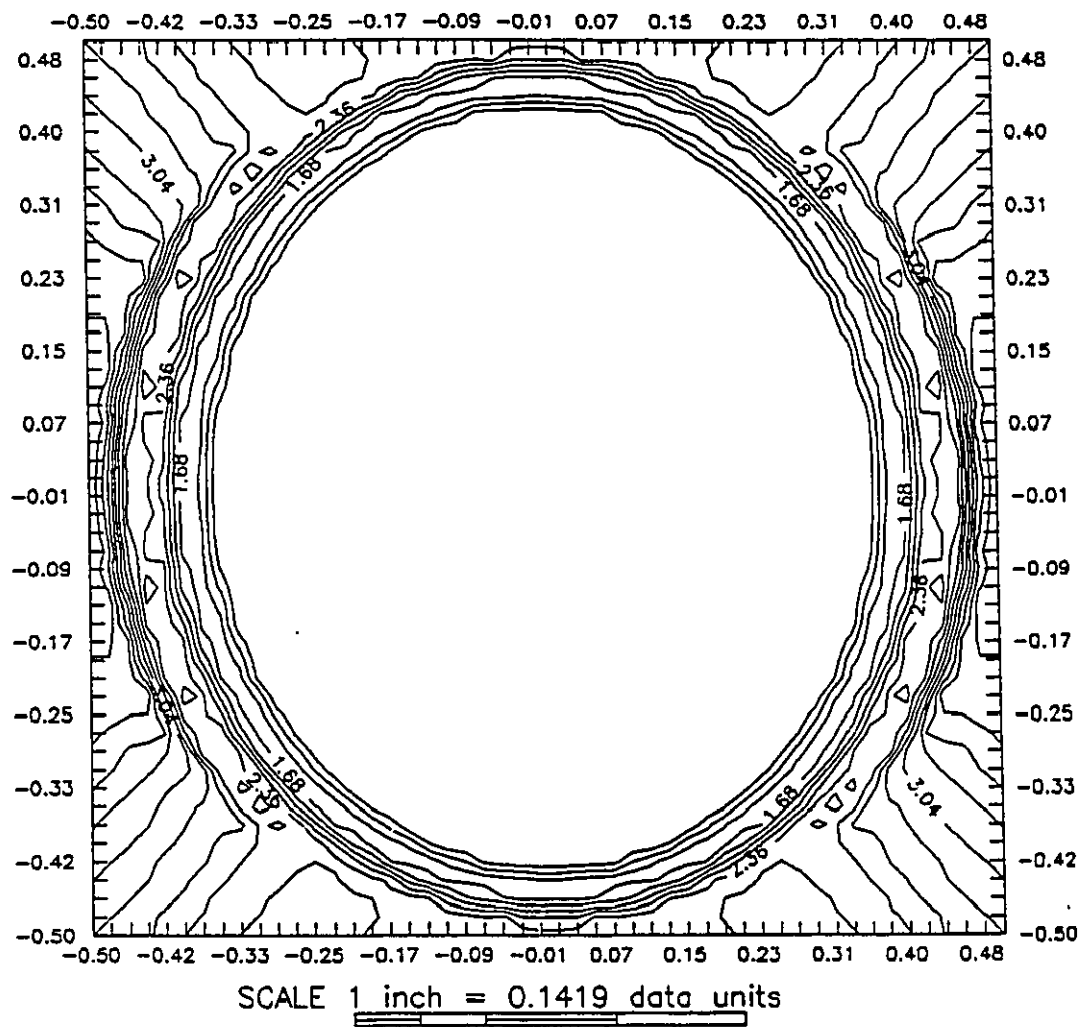
Figure (3.19a)- Iso-density contours for a converging elliptical shock wave

$(t = 0.062, \xi_0 = 0.064, K = 4)$

114

Figure (3.19b)- Iso-density contours for a converging elliptical shock wave

$(t = 0.157, \xi_o = 0.064, K = 4)$

Figure (3.19c)- Iso-density contours for a converging elliptical shock wave
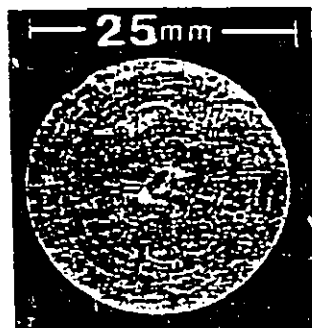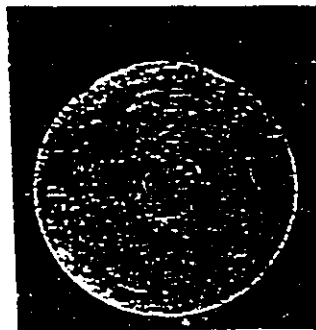
$(t = 0.201, \xi_0 = 0.064, K = 4)$

Figure (3.19d)- Iso-density contours for a converging elliptical shock wave

$(t = 0.274, \xi_o = 0.064, K = 4)$

117

Figure (3.19e)- Iso-density contours for a converging elliptical shock wave

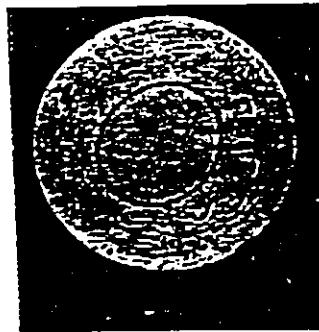$(t = 0.320, \xi_o = 0.064, K = 4)$

118

Figure (3.20)- Photos for a converging elliptical shock wave $\xi = 0.065$
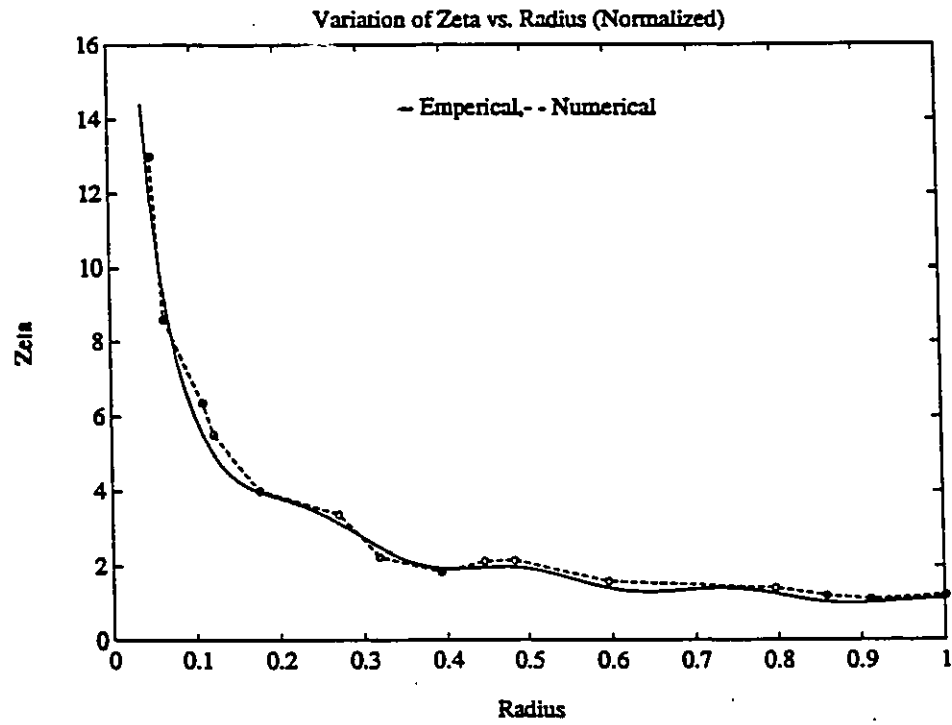(Tashtoush [46])

Figure (3.21)- Amplification of the perturbation parameter ξ for converging

elliptical shock waves (Normalized)